THE UNIVERSITY
of EDINBURGH

Inertia-gravity-waves in geostrophic turbulence

Miles A. C. Savva

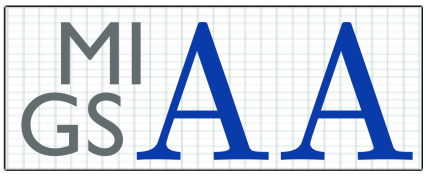

Thesis submitted in fulfilment of
the requirements for the degree of
Doctor of Philosophy
to the
University of Edinburgh — 2019

Declaration

I declare that this thesis was composed by myself, that the work contained herein is my own except where explicitly stated otherwise in the text, and that this work has not been submitted for any other degree or processional qualification except as specified.

Miles A. C. Savva
– 2019

Abstract

The dynamics of the atmosphere and ocean can be decomposed into a slow, large-scale component, in near geostrophic and hydrostatic balance, and a fast component consisting mostly of inertia–gravity waves (IGWs). These waves exist because of restoring forces provided by a combination of gravity and density stratification, and the Coriolis effect due to rotation of the Earth. Their frequencies are high, from a few hours to minutes, while their wavelengths span a broad range of scales, from say 500 km in the atmosphere and 100 km in the ocean, down to metre scales.

IGWs are important for a number of processes since they induce a transport of mass and momentum, interact with the slow component of the motion, and ultimately affect global-scale circulation in the atmosphere and ocean. It is therefore important to be able to predict and understand their evolution to model weather, ocean dynamics and climate. This evolution is complicated by the fact that IGWs do not propagate in tranquil, homogeneous environments but in the complex field of eddies and currents that characterises the nonlinear dynamics of the slow motion and is described as geostrophic turbulence.

This thesis develops new mathematical models of the propagation of IGWs in geostrophic turbulence. The new models represent the turbulent background flow using random fields and capture its impact, through advection and refraction, in a statistically-averaged sense.

In the simplest case, wave energy can be mathematically represented by a single point in wavenumber space, corresponding to a plane wave with a well defined

wavelength and direction of propagation. The presence of a background flow causes IGWs to scatter however, giving rise to changes in length-scales and directions of propagation. This corresponds to transfers of wave energy across wavenumber space. In this thesis we derive equations governing the statistics of these energy transfers. The derivations rely on the Wigner transform to define a wavenumber-resolving energy density, and on multiscale asymptotics to derive the equation it satisfies, a kinetic equation in which the scattering effect is represented through an integral in wavenumber space. In the limit of IGWs short compared with the turbulence scales, the WKB approximation applies and the scattering integral reduces to a diffusion operator in wavenumber space.

We examine scattering in a series of increasingly general scenarios. First, for scattering by flows with no vertical dependence, the governing equations for IGWs can be reduced to an equivalent shallow-water system. This setting is appropriate for studying low-mode internal tides propagating through a turbulent field of eddies which typically share similar length-scales. The kinetic equation shows that energy transfers are restricted to waves with the same frequency and identical vertical structure, and that they ultimately lead to an isotropic wave field when the turbulent flow is itself isotropic. The equation enables us to estimate characteristic time and length scales for scattering and isotropisation. We carry out simulations of internal tides generated by a planar wavemaker for the linearised shallow-water model to confirm the pertinence of these scales. A comparison with the numerical solution of the kinetic equation demonstrates the validity of the latter and illustrates how the interplay between wave scattering and transport shapes the wave statistics.

Second, we consider geostrophic turbulence with a non-trivial vertical structure consistent with Charney's theory. This leads to radically different dynamics, with a cascade of energy towards small scale in both the horizontal and vertical. We explore this using the diffusion approximation to the kinetic equation that arises in the WKB limit. We derive explicit solutions for both initial-value and forced steady-state scenarios. In the forced case, diffusion leads to a k^{-2} wave energy spectrum, consistent with as-yet-unexplained features of observed oceanic and atmospheric spectra.

Third, we go beyond the WKB approximation to consider the full kinetic equation that applies in the absence of spatial-scale separation between IGWs and geostrophic flow. We demonstrate how the kinetic equation recovers the diffusion equation in

the appropriate limit and show that it captures new dynamical features, negligible in the WKB limit but significant in practice including the reflection of upward- to downward-propagating waves. We compare the predictions of the kinetic equation and those of its diffusion approximation to high-resolution numerical simulations of the three-dimensional Boussinesq equations.

Taken together, the results provide a detailed description of the impact of geostrophic turbulence on IGWs, quantifying the spectral transfers that take IGW energy from the forcing scales to the dissipation scales and highlighting the manner in which turbulence shapes the distribution of IGW energy in the atmosphere and ocean.

Acknowledgements

Above all I must thank my supervisor, Jacques Vanneste, for the academic training, personal and professional growth, and the genuinely enjoyable collaboration I have experienced during my time in Edinburgh. I feel fortunate to have had a patient and understanding supervisor, with the vision, intuition, and enthusiasm to help keep the project moving at times when I felt I was at an impasse. I have learnt a lot by working with him, and I am leaving Edinburgh as a better thinker as a result.

I might not have had this opportunity at all, however, had I not had the good fortune of meeting Alexandra Tzella during my Undergraduate at the University of Birmingham. Besides being an excellent teacher, she took an interest in my development beyond what was required and helped me on my academic journey. I am glad that I listened to her recommendations and am grateful for her encouragement.

I have been glad to keep another connection from Birmingham through to Edinburgh, Ben, with whom I have shared countless coffees and conversations over the years. Though our areas of study diverged slightly, our struggles and experiences have been quite similar so it has been good to have someone to relate to.

My thanks go to Hossein for a brief but enjoyable collaboration. His numerical expertise allowed the work to come to life, and as a consequence it became more interesting to me.

Throughout my Ph.D. I have met many interesting and impressive people, but

Manita stands out as someone I have had particularly enjoyable and valuable discussions with since meeting by chance in Hamburg. I thank her for kindly offering to give feedback on some of the earliest and least refined parts of my thesis.

Finally, I have been supported and encouraged by my friends and family, particularly at home during the thesis-writing phase. When I wanted distraction from my work, I could always rely on Barney, Ben, Can and Luke to keep me entertained.

Miles A.C. Savva was supported by The Maxwell Institute Graduate School in Analysis and its Applications, a Centre for Doctoral Training funded by the UK Engineering and Physical Sciences Research Council (grant [EP/L016508/01]), the Scottish Funding Council, the University of Edinburgh and Heriot-Watt University.

Contents

Chapter 1

Waves and flows in the atmosphere and ocean

The introductory material for this thesis is divided into two parts. In this chapter we introduce the physical context for the work reported in this thesis, and describe some of the open questions that we seek to address. The second chapter delves into the technical, theoretical details that underpin the remaining chapters.

We begin with an overview of the atmospheric and oceanic dynamics relevant to the thesis, followed by a technical interlude to introduce some textbook-style essentials that allow for precise definitions of the important terms such as *inertia-gravity waves* and the *vortical mode*. We conclude this chapter with a plan of the thesis.

1-1 Introduction

The atmosphere and the ocean are fluids that exhibit many forms of motion over an enormous range of length and time scales – with violent tornadoes and tsunamis, steady jets and gyres, booming sound waves and crashing surface waves to name a few. In this thesis we are concerned with two in particular from the variety of observed motions – the slow flows in approximate geostrophic and hydrostatic balance with

observable features persisting for weeks to months, and the comparatively fast inertia-gravity waves with periods of a few hours down to the scale of seconds.

The slowly evolving, large-scale balanced motions are well understood and captured by simple models, such as the quasigeostrophic model and its extensions. Such models exploit the strong influence of rotation and stratification on the largest scales – the synoptic scale in the atmosphere spanning thousands of kilometres in the horizontal, and the mesoscale in the ocean spanning hundreds of kilometres. They reduce the degrees of freedom compared to the more complete primitive equations, and in particular they filter out waves. The simplified models such as the quasigeostrophic theory yielded the earliest successes for meteorologists in weather forecasting, though there was an early appreciation by pioneers such as Charney that the influence of waves could not be neglected (Lynch, 2008).

Attempts to establish a picture of the large-scale balanced motions, the global circulation of the atmosphere and ocean, are impeded by the presence of internal waves that continually perturb the background state (Thorpe, 2005). The waves constitute a significant fraction of the internal excitations that thwarted early efforts to establish a map of the background state of the ocean, including its mean currents and isopycnal levels. Helland-Hansen and Nansen noted in 1909, following the first large hydrographic survey in the Norwegian Sea, that 'puzzling waves', now known to be inertia-gravity waves (IGWs), make it 'more difficult than expected to obtain trustworthy representations' of various mean properties of the ocean.

So where do the waves come from? Waves are driven by restoring forces acting in opposition to displacements of fluids away from equilibrium positions. For IGWs the forces are provided by the combination of gravity and density stratification, as well as the Coriolis effect due to rotation of the Earth (see §1-2 for the technical details). The main sources of IGWs include flows over topographic features, convection, and – particularly in the ocean – the effects of wind and tidal forcing (see Wunsch and Ferrari (2004) and Staquet and Sommeria (2002) for in-depth reviews). They can also be generated spontaneously from the balanced motions themselves, potentially across a range of frequencies and scales (Vanneste, 2013). The spatial scales of IGWs extend over several orders of magnitude, from around 100 kilometres down to the centimetre scale. There is thus a large range of overlap where IGWs coexist with large-scale balanced turbulence, and the dynamics in that range are complicated and poorly understood (McWilliams, 2016). Confusingly, the (dynamically equivalent) ranges are

known as the mesoscale in the atmosphere and submesoscale in the ocean – we shall refer to them collectively as submesoscale from now on. In the ocean, the submesoscale is from around 1-100 km (Callies, 2016), and in the atmosphere it extends further upwards from around 10-500 km (Callies *et al.*, 2014). In order to understand the dynamics in this regime, there is a need to disentangle the contributions from the balanced motions and unbalanced IGWs in observational and numerical data (Morrow *et al.*, 2019; Torres *et al.*, 2018). The relative strength of the balanced and unbalanced motions varies both in space and time, and IGWs can dominate and mask balanced flows in the submesoscale at some locations (Callies, 2016). We note that some oceanographers identify submesoscale dynamics with the highly energetic currents and fronts at the ocean surface which, though also not balanced, have little to do with IGWs.

Aside from being a nuisance for observations, IGWs are an important dynamical agent for mixing and transport, particularly in the ocean. Vertical (diapycnal) mixing due to wave breaking in the ocean is responsible for transporting heat, with implications for the density structure of the ocean, global climate, and solutants that are necessary for biological systems (e.g. Wunsch and Ferrari (2004)). As discussed by Staquet and Sommeria (2002) "much, if not all, of the mixing energy is bound up in the internal wave field" which can be radiated throughout the ocean. IGWs also play a key role in the maintenance of balance globally, where they are presumed to facilitate a cascade of energy from the large scales where energy is constantly being injected to the small scales where energy can be transformed to other forms such as heat through viscous dissipation (Wunsch and Ferrari, 2004). Furthermore, Thomas and Yamada (2019) described IGWs as an integral part of the geophysical turbulence phenomenology due to their influence in the evolution of the balanced motions.

Despite the many significant roles that IGWs are known to play, small-scale IGWs are still typically filtered out of or unresolved by general circulation models (GCMs) for climate and weather simulations (Staquet and Sommeria, 2002), though larger-scale IGWs can be resolved. Instead GCMs rely on parameterisations to attempt to represent the long term effect of IGWs on the larger scale motions. This is a choice forced by practical limitations – even the most recent estimates suggest that a factor $10^3 - 10^4$ greater resolution than state-of-the-art high-resolution GCMs currently apply would be necessary in order to resolve waves above horizontal scales of $\sim 2\mathrm{km}$ in atmospheric simulations (Liu, 2019). It is a problem that the submesoscale range can

be dominated by IGWs since much of the range is sub-gridscale, and can be affected by numerical diffusion. There is therefore a need to inform parameterisation choices and modelling decisions with as much understanding of IGW dynamics as possible, and particularly with how their long term evolution is shaped by interactions, both within the IGW wave field itself and with the balanced motions, since the sub-gridscale dynamics impact the long-term, large-scale forecasts.

Recently, data-analysis methods have been developed that are helping to add new clarity on these issues. Diagnostic techniques that decompose energy spectra, deduced from observations along single flight paths or ship tracks, into orthogonal contributions associated with the vortical and divergent parts of the flow have been advanced in a series of papers (Callies and Ferrari, 2013; Callies *et al.*, 2014, 2016). They found a strong divergent motion, partly associated with IGWs, across the submesoscales that can dominate over the vortical part of the flow, associated with the balanced motions. Further analysis based on the linear IGW dispersion relation and polarisation relations (see §1-2) decomposes the spectra into a part due to linear IGWs and a geostrophic remainder. Examples of decomposed atmospheric spectra taken from their papers are shown in Figure 1-1. From the decomposed spectra Callies *et al.* conclude that almost-linear IGWs dominate the submesoscales in much of the atmosphere and ocean, a controversial conclusion (e.g. Li and Lindborg (2018)), but it highlights the need to understand the submesoscale dynamics in greater detail. Understanding what shapes the IGW spectrum in this range is clearly a necessary and important component.

Before going further and setting out the specific ways this thesis aims to address some of the issues raised in the introduction, a brief technical interlude fixes the mathematical description and the terminology for IGWs and balanced motions.

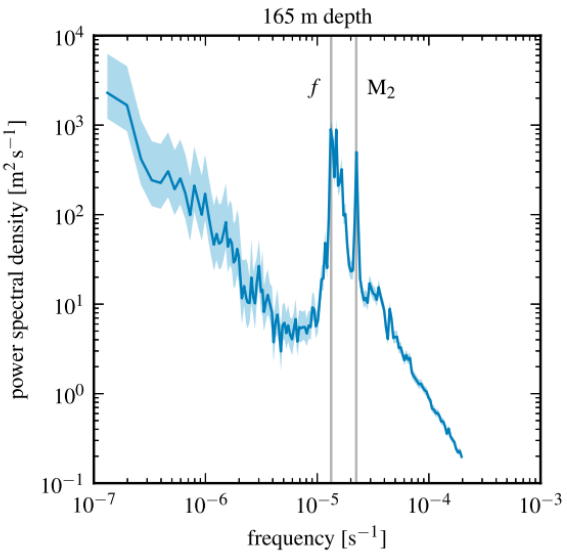

(a) Frequency spectrum of oceanic kinetic energy from a fixed location. Note the largest contributions from low-frequencies in near-geostrophic balance, and a large increase in energy at frequencies above f where IGWs are supported. (From Callies and Ferrari (2013).)

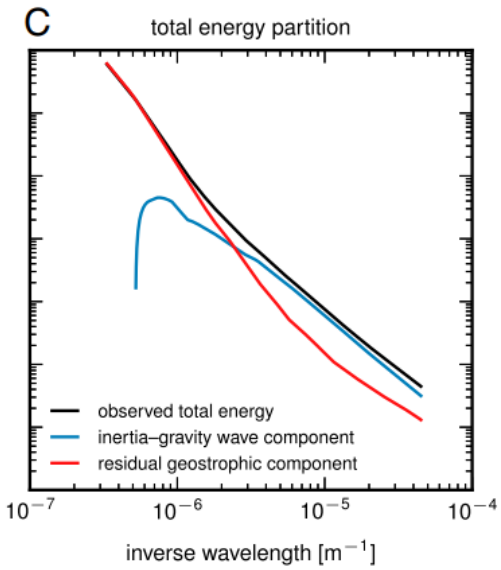

(b) Observed wavenumber spectrum of midlatitude atmospheric total kinetic energy, along with its decomposition into an IGW component and a geostrophic remainder. Note that the submesoscale range is approximately between $2 \times 10^{-6} - 10^{-4}\mathrm{m}^{-1}$. (From Callies *et al.* (2014).)

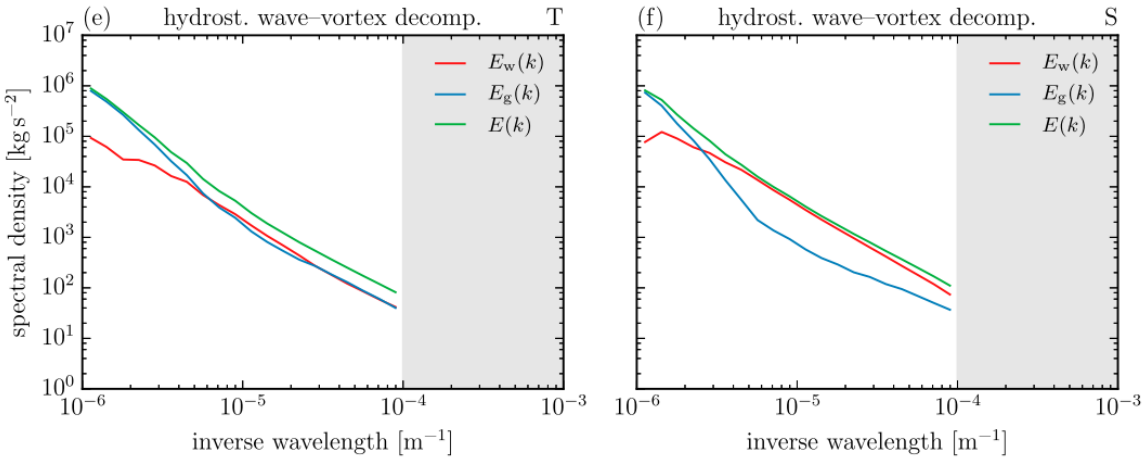

(c) As in 1-1b but separated into spectra collected in the upper troposphere (left), where IGWs are important but not sufficient to explain the observed energy spectrum, and lower stratosphere (right) where IGWs dominate across the submesoscale range. (From Callies *et al.* (2016).)

Figure 1-1.

1-2 Preliminaries

This section contains some of the basic textbook-style theory relating to IGWs, setting out some of the notation and fixing the essential modelling ideas. These include the governing equations for IGWs, their dispersion relation, and a definition of the vortical mode. The most important parts are repeated in later chapters, and no new ideas unique to the thesis are raised in this section.

1-2.1 The Boussinesq approximation

The simplest fluid model that incorporates the effects of stable stratification and rotation to admit inertia-gravity waves is the (rotating) Boussinesq equations (Bühler, 2014), which can be seen as a simplified form of the Euler equations. In essence[1], the model assumes that the fluid density ρ varies by only a small amount from a constant reference density ρ_0. Without any approximation we can decompose the density field into a constant part ρ_0, a part that varies only with depth $\bar{\rho}(z)$, and a remaining perturbation quantity $\rho'(\boldsymbol{x}, t)$ such that

$$\rho(\boldsymbol{x}, t) = \rho_0 + \bar{\rho}(z) + \rho'(\boldsymbol{x}, t).$$

The Boussinesq approximation then assumes that $\bar{\rho}, \rho' \ll \rho_0$, which is a good approximation in the ocean where the density varies by only about 3%, but can only be justified in limited circumstances in the atmosphere where the density can change by 100% in the vertical (Bühler, 2014). This allows for the replacement of ρ by the constant ρ_0 everywhere except for the terms involving gravitational effects which, in the Boussinesq approximation, are assumed to be large compared with other fluid accelerations.

The fluid stratification is characterised by a density profile as a function of height, $\bar{\rho}(z)$. The frequency of oscillations exhibited by a fluid particle displaced from its equilibrium position and restored by a buoyancy force is given by the buoyancy, or

[1]Beyond this simple heuristic explanation of the Boussinesq approximation, asymptotic derivations and reasoned justifications can be found for example in Müller (2006) and Salmon (1998).

Brunt-Väisälä, frequency N defined by

$$N(z) = \left(-\frac{g}{\rho_0} \frac{\mathrm{d}\bar{\rho}}{\mathrm{d}z} \right)^{1/2}. \tag{1-2.1}$$

In order for N to be a real number we must have $\mathrm{d}\bar{\rho}/\mathrm{d}z < 0$, i.e. the density should decrease with height – this is the condition for stable stratification, which we exclusively consider throughout this thesis. Unstable stratification configurations where more dense fluid sits atop less dense fluid are also observed in nature, and are responsible for phenomena such as the Rayleigh-Taylor instability. A typical value for the buoyancy frequency is $N = O(10^{-3})\ \mathrm{s}^{-1}$ in the ocean interior (Olbers *et al.*, 2012), and in the atmosphere from $N = O(10^{-2})\ \mathrm{s}^{-1}$ in the troposphere to larger values in the lower stratosphere (Gill, 1982). We assume fluids with a constant buoyancy frequency N in this thesis.

The rotation of the Earth provides a Coriolis effect whereby a particle in motion experiences a force perpendicular to its velocity. We incorporate the effect under the *traditional approximation*, which assumes that fluid motions are mostly horizontal such that only the vertical component of the angular velocity vector for the Earth's rotation needs to be retained. Thus the full Coriolis acceleration $\boldsymbol{f} \times \boldsymbol{u}$ is approximated as $f\hat{\boldsymbol{z}} \times \boldsymbol{u}$, with $\hat{\boldsymbol{z}}$ the vertical unit vector. The Coriolis parameter $f = 2\Omega \sin\phi$, where $\Omega \simeq 7 \times 10^{-5}\mathrm{s}^{-1}$ is the rotation rate of the Earth and ϕ is the latitude. We additionally make the *f-plane approximation* which takes the latitude as a fixed constant such that $f = f_0 = 2\Omega \sin\phi_0$. A typical value is $f = O(10^{-4})\ \mathrm{s}^{-1}$ in the midlatitudes (Olbers *et al.*, 2012). The f-plane approximation filters out motions such as Rossby waves, which exist due to the meridional variation of the Coriolis acceleration due to the curvature of the Earth. Such motions can be recovered by including additional terms in the expansion of the Coriolis parameter, for example with the β-plane approximation $f = f_0 + \beta y$, where $\beta = (\mathrm{d}f/\mathrm{d}y)|_{\phi_0} = 2\Omega \cos\phi_0 / R$, where R is the Earth's radius. Note that typically $f < N$ in the atmosphere and ocean though regions where $N \leq f$ also exist, typically at high latitudes where f is nearly maximal and stratification is weak. In such regions, IGWs cannot propagate.

The Boussinesq model can then be written in primitive variables as

$$\rho_0\big(\partial_t \boldsymbol{u} + \boldsymbol{u}\cdot\nabla\boldsymbol{u} + f\hat{\boldsymbol{z}}\times\boldsymbol{u}\big) = -\nabla p - g\rho\hat{\boldsymbol{z}}, \tag{1-2.2}$$

$$\partial_t \rho + \nabla\cdot(\rho\boldsymbol{u}) = 0, \tag{1-2.3}$$

$$\nabla\cdot\boldsymbol{u} = 0. \tag{1-2.4}$$

The first equation (1-2.2) is the momentum equation, and (1-2.3) is the continuity equation. The final equation (1-2.4) expresses that the fluid is assumed to be incompressible which has the effect of filtering out sound waves, reducing the degrees of freedom compared to the full compressible Euler system. Incompressibility is a reasonable approximation for the ocean, but is less applicable to the atmosphere where either more complicated models such as the anelastic approximation should be used, or restrictions on the vertical range of motion apply such that the density does not vary much.

We can further decompose the pressure without approximation into a part that varies only with depth $\bar{p}(z)$, and a remaining perturbation quantity $p'(\boldsymbol{x},t)$, such that

$$p(\boldsymbol{x},t) = \bar{p}(z) + p'(\boldsymbol{x},t).$$

Taking $\rho_0 + \bar{\rho}$ and $\bar{p}$ so that they are consistent with a basic state of rest leads to the hydrostatic balance relation

$$\frac{\mathrm{d}\bar{p}}{\mathrm{d}z} = -g(\rho_0 + \bar{\rho}(z)). \tag{1-2.5}$$

It is convenient to introduce the variable

$$b(\boldsymbol{x},t) = -\frac{g}{\rho_0}\rho'(\boldsymbol{x},t),$$

which is known as the *buoyancy*. Then, using the hydrostatic balance relation (1-2.5) in the momentum equation (1-2.2), and the rewriting the continuity equation (1-2.3) in terms of the buoyancy b along with (1-2.1) leads to a more convenient form of the

Boussinesq approximation:

$$\left.\begin{aligned} \partial_t \boldsymbol{u} + \boldsymbol{u}\cdot\nabla\boldsymbol{u} + f\hat{\boldsymbol{z}}\times\boldsymbol{u} &= -\nabla\tilde{p} + b\hat{\boldsymbol{z}}, \\ \partial_t b + \boldsymbol{u}\cdot\nabla b + N^2 w &= 0, \\ \nabla\cdot\boldsymbol{u} &= 0, \end{aligned}\right\} \tag{1-2.6}$$

where $\tilde{p} = p'/\rho_0$ is the kinematic pressure above the hydrostatic value.

We note that this nonlinear system admits a materially conserved quantity known as the *potential vorticity* (e.g. see Majda (2003)), defined as

$$q = (\nabla\times\boldsymbol{u} + f\hat{\boldsymbol{z}})\cdot\nabla(b + N^2 z) - fN^2, \tag{1-2.7}$$

such that $\partial_t q + \boldsymbol{u}\cdot\nabla q = 0$.

1-2.2 Linear dynamics

We linearise (1-2.6) about a state of rest in order to consider its normal-mode solutions. The linearised equations, which assume small amplitudes so that the nonlinear advective terms are negligible, can be written as

$$\left.\begin{aligned} \partial_t \boldsymbol{u}_h + f\hat{\boldsymbol{z}}\times\boldsymbol{u}_h &= -\nabla_h\tilde{p}, \\ \partial_t w &= -\partial_z\tilde{p} + b, \\ \partial_t b + N^2 w &= 0, \\ \nabla\cdot\boldsymbol{u} &= 0. \end{aligned}\right\} \tag{1-2.8}$$

Taking a plane-wave ansatz of the form

$$\begin{pmatrix} u \\ v \\ w \\ b \\ \tilde{p} \end{pmatrix} = \mathrm{Re}\begin{pmatrix} \hat{u} \\ \hat{v} \\ \hat{w} \\ \hat{b} \\ \hat{p} \end{pmatrix} \exp[\mathrm{i}(\boldsymbol{k}\cdot\boldsymbol{x} - \omega t)],$$

where the wavevector $\boldsymbol{k} = (k_1, k_2, k_3)$ and Re denotes taking the real part of the expression, and substituting into (1-2.8) leads to the system

$$\left.\begin{aligned} -\mathrm{i}\omega\hat{u} - f\hat{v} + \mathrm{i}k_1\hat{p} &= 0, \\ -\mathrm{i}\omega\hat{v} + f\hat{u} + \mathrm{i}k_2\hat{p} &= 0, \\ -\mathrm{i}\omega\hat{w} + \mathrm{i}k_3\hat{p} - \hat{b} &= 0, \\ -\mathrm{i}\omega\hat{b} + N^2\hat{w} &= 0, \\ \mathrm{i}(k_1\hat{u} + k_2\hat{v} + k_3\hat{w}) &= 0. \end{aligned}\right\} \tag{1-2.9}$$

These are five linear, homogeneous equations for the five variables in this system; however there are only three independent degrees of freedom. The characteristic polynomial to consistently solve this system of equations is therefore cubic in the unknown ω, and is given by

$$\omega(\omega^2 - (N^2k_h^2 + f^2k_3^2)^{1/2}/k) = 0, \tag{1-2.10}$$

where $k = |\boldsymbol{k}|$, and $k_h = \sqrt{k_1^2 + k_2^2}$ is the horizontal wavenumber. We see that (1-2.10) is solved by either a time-independent solution with $\omega = \omega_0 = 0$, or

$$\omega = \omega_\pm = \pm\frac{(N^2k_h^2 + f^2k_3^2)^{1/2}}{k} \tag{1-2.11}$$

which is the dispersion relation for inertia-gravity waves.

The linearised Boussinesq equations (1-2.8) conserve the linearised form of the potential vorticity (1-2.7), which we write as

$$q_l = N^2\zeta + f\partial_z b$$

such that $\partial_t q_l = 0$, where we have written the vertical component of the vorticity as $\zeta = \hat{\boldsymbol{z}}\cdot\nabla\times\boldsymbol{u}$. We show in Appendix A that q_l is only non-zero when $\omega = 0$. Therefore the ω_0 mode is commonly also known as the *vortical mode*, and corresponds to the linear manifestation of the large-scale balanced motions of geostrophic turbulence. In the nonlinear case, the evolution of the balanced motion is characterised by advection of the full potential vorticity q (Vallis, 2017). The IGW modes $\omega_\pm$ have zero potential vorticity and play no role in its dynamics in the linear approximation.

Properties of the IGW modes $\omega = \omega_\pm$

From the dispersion relation (1-2.11) we note that the IGW frequency is bounded from below by the Coriolis parameter for purely vertical wavevector, and from above by the buoyancy frequency for purely horizontal wavevector, so that $f \leq |\omega| \leq N$. We can observe in Figure 1-1a that there is an abrupt increase in the kinetic energy content of the ocean from $\omega = f$ as the IGW modes become active.

From (1-2.9) we can write the polarisation relations for the IGW modes in the form

$$\hat{u} = \frac{k_1}{\omega - \mathrm{i}f}\,\hat{p}, \quad \hat{v} = \frac{k_2}{\omega + \mathrm{i}f}\,\hat{p}, \quad \hat{w} = \frac{\omega k_3}{\omega^2 + N^2}\,\hat{p}, \quad \hat{b} = \frac{-\mathrm{i}N^2 k_3}{\omega^2 + N^2}\,\hat{p}.$$

These express the relationship between the various dependent variables, for example their relative phases.

From the last equation of (1-2.9) we see that $\boldsymbol{k} \cdot \boldsymbol{u} = 0$, which tells us that IGWs are purely transverse waves – their motion is along lines of constant phase. The phase speed is given by $c_p = \omega/k$, or in a given direction by $c_p^{(i)} = \omega/k_i$. The group velocity, which is the velocity with which energy propagates, is also obtained from the dispersion relation as $\boldsymbol{c}_g = \nabla_{\boldsymbol{k}}\omega = (\boldsymbol{c}_g^{(h)}, c_g^{(3)})$, and in a given direction $c_g^{(i)} = \partial\omega/\partial k_i$. Explicitly, the horizonal and vertical group velocity is given as

$$\boldsymbol{c}_g^{(h)} = \frac{\boldsymbol{k}_h k_3^2}{\omega k^4}(N^2 - f^2), \quad c_g^{(3)} = -\frac{k_3 k_h^2}{\omega k^4}(N^2 - f^2). \tag{1-2.12}$$

IGWs have a peculiar property that in the vertical direction, the wave phase and the energy propagate in opposition since

$$c_p^{(3)} c_g^{(3)} = \frac{\omega}{k_3}\frac{\partial\omega}{\partial k_3} = -\frac{k_h^2}{k^4}(N^2 - f^2) < 0,$$

so that upward propagating IGWs have a phase that increases downwards. Furthermore we see from (1-2.12) that the group velocity is along the constant phase lines since $\boldsymbol{c}_g \cdot \boldsymbol{k} = 0$.

Properties of the vortical mode $\omega = 0$

The vortical mode solution is a steady, time-independent solution to (1-2.8) such that the time derivatives disappear, or equivalently obtained by setting $\omega = 0$ in (1-2.9).

This mode appears stationary in the linear approximation because it evolves on a much longer time scale than the IGWs in the full, nonlinear system.

From (1-2.9) we can write the polarisation relations for the vortical mode as

$$\hat{u} = -\mathrm{i}k_2\hat{p}/f, \quad \hat{v} = \mathrm{i}k_1\hat{p}/f, \quad \hat{w} = 0, \quad \hat{b} = \mathrm{i}k_3\hat{p}.$$

We see that $w = 0$, so the vortical mode motion is purely horizontal. The incompressibility constraint then reduces to $\nabla_h \cdot \boldsymbol{u} = 0$ so that the fluid is horizontally non-divergent. We see also that the horizontal velocity fields are in geostrophic balance with the pressure, and the buoyancy field is hydrostatically balanced.

1-3 Thesis overview

1-3.1 Aims for this thesis

The aim of this thesis is to quantify and characterise how IGWs evolve in the presence of geostrophic turbulence. In particular, we study the statistics of linear IGWs that interact weakly with the vortical mode, described in more detail in the next chapter. We hope to give a quantification of and clear insight into the role of the vortical mode in shaping some of the observed IGW features in the atmosphere and ocean, as most previous studies have focused only on nonlinear wave-wave interactions in attempting to explain features such as energy cascades, equilibrium energy spectra, and various scattering processes.

Wave-wave interaction studies have far outnumbered those of wave-vortical mode interactions. This can be partly explained by the fact that the earliest studies (e.g. Hasselmann (1962); Müller and Olbers (1975); Olbers (1976); McComas and Bretherton (1977); Henyey and Pomphrey (1983)) were framed in a Lagrangian setting, and it is difficult to study interactions with the vortical mode in such a setting (Müller *et al.*, 1986; Staquet and Sommeria, 2002). Nevertheless, these studies yielded some success in explaining how aspects of the IGW spectrum could be interpreted and quantified by wave-wave interactions such as the parametric subharmonic instability and induced diffusion classes of energy transfers, and the successes generated more interest and focus on wave-wave interactions alone. Modern techniques such as those of wave turbulence (Nazarenko, 2011) have been similarly inappropriate for studying

the wave-vortical mode interactions. Wave turbulence relies on the existence of a small parameter in the form of a ratio between nonlinear and linear parts of the system (Zakharov *et al.*, 2004) which is undefined for the vortical mode since it has zero linear part ($\omega = 0$).

Yet there have been a number of studies that have shown the vortical mode to be an effective agent for redistributing IGW energy in wavenumber space. These have included Warn (1986), Lelong and Riley (1991), Bartello (1995), and Ward and Dewar (2010), but the literature is comparatively thin. These studies have typically focused on purely spectral descriptions of the energy transfers, and either used statistical mechanics arguments to establish the existence and direction of energy cascades, or in the case of Ward and Dewar (2010) have provided a deterministic theory which does not reveal much about the generic properties of IGWs scattered by turbulence.

This thesis goes some way towards filling the gap in the literature by developing the theory to quantify and characterise IGW scattering by geostrophic turbulence. We do this by employing a statistical description, representing the turbulent background flow using random fields, which highlights how turbulence shapes the distribution of IGW energy through transfers in physical and spectral space.

A description of the remaining chapters is now given.

Chapter 2: Kinetic equations for waves in random flows

Chapter 2 introduces and describes the mathematical machinery we use for studying waves scattered by geostrophic turbulence. We begin by discussing and defining the various possible scaling regimes and the different techniques that are appropriate in each case before focusing on one regime in particular, the scattering regime. We derive a kinetic equation in the scattering regime for the evolution of a wavevector-resolving energy density $a(\boldsymbol{x}, \boldsymbol{k}, t)$ which is based upon the Wigner transform of the wave fields. The kinetic equation describes, in a statistical sense, the energy transfers through physical and spectral space that IGWs undergo due to their interactions with geostrophic turbulence.

Chapter 3: Scattering of internal tides

Having developed a fairly general theory, we apply it to a specific but simplified case of scattering by flows with no vertical dependence. There, the governing equations for IGWs reduce to an equivalent shallow-water system. Such a model is appropriate for studying the propagation of low-mode internal tides through a turbulent field of eddies with shared length scales. The kinetic equation derived for this chapter allows us to estimate characteristic time and length scales for scattering and isotropisation of the IGWs based on physical parameters. It predicts that energy transfers are restricted to waves with the same frequency, and consequently the same length scales, and also with identical vertical structure. We compare the predictions to simulations of the linearised shallow-water model to confirm the validity of the estimates. The subject of this chapter has been published as a paper in the *Journal of Fluid Mechanics* (Savva and Vanneste, 2018).

Chapter 4: Diffusion of IGWs by geostrophic turbulence

In this chapter we consider scattering by geostrophic turbulence with a non-trivial vertical structure which introduces new dynamical effects due to vertical shear by the flow. In particular, it introduces a mechanism for IGW energy to cascade to small scales in both the horizontal and vertical. We explore a simplified regime of waves that are short relative to the geostrophic turbulence in length scales such that a diffusion approximation to the kinetic equation applies. With the simpler diffusion equation description, we derive explicit solutions to both initial-value and forced steady-state scenarios. In the forced case, we observe that diffusion leads to an equilibrium spectrum with a k^{-2} dependence above the forcing scales which is consistent with and relevant to observational oceanic and atmospheric spectra, such as those shown in this introduction chapter. The predictions of the diffusion equation are compared with and verified by high-resolution simulations of the three-dimensional Boussinesq equations. The contents of Chapter 4 have been published as a paper in the *Journal of Fluid Mechanics* (Kafiabad, Savva and Vanneste, 2019).

Chapter 5: Scattering of IGWs by geostrophic turbulence

In Chapter 5 we incorporate the full complexity of geostrophic turbulence with non-trivial vertical structure and length scales that overlap with that of IGWs. As in Chapter 3, this is achieved by deriving a kinetic equation based on the method from Chapter 2. We show that in the appropriate limits we can recover the kinetic equation from Chapter 3 and the diffusion equation from Chapter 4, but that the kinetic equation also captures some of the dynamical features missing from the simplified models. In particular this includes the reflection of upward- to downward-propagating waves, and predictions about the equilibration of energy between the two types of waves. Again we compare the kinetic equation with numerical simulations of the full three-dimensional Boussinesq equations, but we also explore outside of the WKB regime such that the diffusion approximation fails to hold but the kinetic equation continues to be applicable. The work in this chapter is being prepared for submission to the *Journal of Fluid Mechanics*.

Chapter 6: Conclusion

We present an overview of the key findings in this thesis, conclusions that can be drawn from them, and how they fit into the context of the broader literature. We then finish with a brief discussion of possible directions for further research.

Chapter 2

Kinetic equations for waves in random flows

In this chapter we introduce the main mathematical tool for studying waves in turbulence that is used in this thesis – the kinetic equation – and we outline the asymptotic regimes for kinetic equations to be valid, along with their physical interpretations. We discuss some of the other theories and methods that apply in other regimes, and some of the general limitations to studying waves in turbulent flows. We present a derivation of the so-called 'scattering integral' form of the kinetic equation in a general and abstract way, such that it can be tailored in later chapters where we then adopt specific models for wave propagation. This is to allow attention to be focused later on the physically relevant quantities for each model without obscuring the analysis with derivations.

The derivation of the kinetic equation is achieved by employing a *Wigner transform* of the wave-fields. The Wigner transform features prominently throughout the rest of the thesis, and so we devote part of this chapter to discuss what it is, and to develop an understanding of how it is applied. The derivation presented within this chapter is based on the appendix of *Scattering of internal tides by barotropic quasi-geostrophic flows*, published in the Journal of Fluid Mechanics (Savva and Vanneste, 2018).

2-1 Introduction

We have seen in Chapter 1 that IGWs span a vast range of length scales, and in the atmosphere and the ocean these scales are not necessarily distinct from the length scales of geostrophic turbulence. This broad range of scales creates difficulties in two ways. First, when trying to simulate the atmosphere and ocean, it would be necessary to take an impossibly fine grid in order to resolve IGWs down to the dissipation scales. The difficulty is made worse by the fact that IGWs evolve on a much faster time scale than the large-scale motions, placing a restriction on the size of the time-steps a numerical simulation can take. Second, the range of spatial scales means that some traditional theoretical approaches for studying waves in a background flow cannot be applied. In particular the WKB method, which is popular due to its simplicity, relies on there being a separation of spatial scales between the waves and background flow.

In this chapter we explore some of the ways to describe the energy transfers due to waves propagating in a background flow, and show that we can overcome the requirement for a spatial scale separation by instead exploiting the separation in time scales.

Weakly nonlinear interactions of waves and flows

In order to frame a mathematical discussion about how we study the interaction of IGWs and balanced flows, along with the scales and regimes involved, we now introduce some notation and an equation for IGW propagation in an abstract form. What follows is a heuristic discussion intended to elucidate the prevalent ideas and essential elements of the models in this thesis, without getting side-tracked by the details of a full and explicit set of equations. We reserve explicit representations of the dynamical equations for later chapters.

Throughout the thesis we take lowercase variables for wave quantities, and uppercase variables for the balanced flow. We always consider a regime of small amplitude waves, such that quadratic nonlinearities of wave fields are negligible. We linearise the wave fields, contained in a vector $\boldsymbol{u}$, about slowly-evolving background flow fields, contained in the vector $\boldsymbol{U}$. The weakness of their interaction and their separation in time is controlled by the small dimensionless Rossby number $\mathrm{Ro} = U_*/fL_* \ll 1$, where U_* and L_* are the characteristic velocity and length scale of the

background flow, and f is a local Coriolis parameter. Typical Rossby numbers are of the order of $\mathrm{Ro} = 0.1$ in the atmosphere and $\mathrm{Ro} = 0.01$ in the ocean, though the number varies in a broad range depending on location and on the chosen definition of the Rossby number.

We can write the equations governing the evolution of IGWs in a weak background flow for a variety of models in the same general form as

$$\partial_t \boldsymbol{u} + \mathcal{L}(\boldsymbol{u}) + \mathrm{Ro}\,\mathcal{N}(\boldsymbol{U}, \boldsymbol{u}) = 0. \tag{2-1.1}$$

Here, $\mathcal{L}$ is a linear differential operator that generates the dispersion relation of the waves when transformed to spectral space, and $\mathcal{N}$ is a bilinear differential operator that arises from the nonlinear terms in the governing equations, for example the advective terms. The small parameter Ro appears from nondimensionalising the equations, but it can be regarded as a bookkeeping parameter to keep track of the relative size of the terms in their dimensional form here. With Ro small, the effects due to the background flow are small compared to the linear dynamics, and so the background flow interacts weakly.

We consider the wave amplitudes to be represented by a characteristic scale u_*, such as the wave rms velocity, and to vary on a spatial scale l_*, the wavelength. We define a wave-based Rossby number $\mathrm{Ro}^{(w)} = u_*/fl_*$, so that when $\mathrm{Ro}^{(w)} \ll 1$ we can neglect terms that are quadratic in wave quantities. When $\mathrm{Ro}^{(w)}$ is large, for example when the waves cascade to very small scales with $l_* \to 0$, then nonlinear effects dominate and cannot be neglected. We note that the linear form of (2-1.1) means that u_* can be divided out of the equation so that there is no explicit dependence on u_*, and in particular there is no condition to impose on the relative strength of U_* and u_*. This matters because it is very often the case in reality that the geostrophic turbulence fields are far more energetic than IGW fields, with $U_* > u_*$, but such an arrangement is not in contradiction with the designation of a 'weakly' interacting background flow which is instead a consequence of time scale separation. There is no requirement for the background flow $\boldsymbol{U}$ to be subject to weakly nonlinear dynamics itself, and we consider it in its full turbulent complexity in this thesis.

Regimes of waves propagating in background flows

The dynamics described by an equation of the form (2-1.1) depend on the choices made for the characteristic scales involved; different choices define different distinguished asymptotic regimes. This thesis explores a subset of the possible dynamics, so it is informative to discuss how the different regimes compare and relate to one another. We consider the characteristic spatial scale, for example the correlation length, of the background flow to be fixed at L_*, or equivalently at its wavenumber counterpart K_*. We can describe how the different terms of (2-1.1) vary for different IGW length scales represented by the wavenumber k_*.

Contained in the operator $\mathcal{N}$ are terms that include the effects of refraction by the flow and Doppler shifting of the wave frequency due to advection by the flow. As a heuristic but explicit example, we can unpack $\mathcal{N}$ in dimensional form to consider

$$\partial_t \boldsymbol{u} + \mathcal{L}(\boldsymbol{u}) + \nabla_{\boldsymbol{X}} \boldsymbol{U} \cdot \boldsymbol{u} + \boldsymbol{U} \cdot \nabla_{\boldsymbol{x}} \boldsymbol{u} = 0. \tag{2-1.2}$$

Here, $\boldsymbol{x}$ is a spatial coordinate varying on the wave scale l_*, while $\boldsymbol{X}$ is a spatial coordinate which varies on the flow scale L_*. Nondimensionalising time by the inertial frequency f, which we assume here to be the relevant time scale for the linear terms in (2-1.2) also, we see the relative scaling of the terms involving the background flow as

$$\begin{gathered} \frac{1}{u_* f}\big[\, \partial_t \boldsymbol{u} + \mathcal{L}(\boldsymbol{u}) + \quad \nabla_{\boldsymbol{X}} \boldsymbol{U} \cdot \boldsymbol{u} \quad + \quad \boldsymbol{U} \cdot \nabla_{\boldsymbol{x}} \boldsymbol{u} \quad \big] = 0. \\ \sim 1 \quad \sim 1 \quad \sim \tfrac{U_*}{f L_*} = \mathrm{Ro} \quad \sim \tfrac{U_*}{f l_*} = \mathrm{Ro}\tfrac{k_*}{K_*} \end{gathered} \tag{2-1.3}$$

Relative to the linear terms of (2-1.3), the refraction term scales as Ro ($\ll 1$), while the Doppler shift scales as $\mathrm{Ro}(k_*/K_*)$. There are are several different distinguished regimes that depend upon the relative spatial scale of the waves and the background flow given by $L_*/l_* = k_*/K_*$ which we describe now.

- First, the combination k_*/K_* can be taken arbitrarily small, which physically amounts to the waves varying on a much larger scale than the background flow. Mathematically, such a regime can be treated by *homogenisation*, a multiple-scales method for averaging the governing equations over the small scale to obtain a leading-order description that is free from the small-scale but contains coefficients representing the effective small-scale contributions.

- When the waves are at a scale similar to the background flow, in other words with $k_* \sim K_*$, the two effects of refraction and Doppler shifts are comparable in magnitude and both scale as Ro. This is known as the *radiative transfer regime* (Hasselmann, 1967; Ryzhik *et al.*, 1996), but we will frequently refer to it as the *scattering regime*.

- For smaller scale waves with $k_* \gg K_*$, the Doppler shift dominates over refractive effects. In this case the background flow varies on a much larger scale than the waves, and so the WKB approximation holds. For this to be a weakly nonlinear effect, it is required that the Doppler term remains small compared with the linear terms of (2-1.1) so that $k_*/K_* < \mathrm{Ro}^{-1}$. This regime is known as *induced diffusion* after McComas and Bretherton (1977) in the context of wave–wave interactions, but as we study it in the context of wave–vortical mode interactions we refer to it differently as the *diffusion regime*. We note that it is also sometimes known as the *random geometric optics* regime (Bal *et al.*, 2010).

- The weakness of the interactions fails to hold for very small waves when the combination $\mathrm{Ro}(k_*/K_*) = O(1)$, and so a different approach exists for small waves with $(k_*/K_*) > O(\mathrm{Ro}^{-1})$ known as the *eikonal method* (Henyey and Pomphrey, 1983; Flatté *et al.*, 1985). This method is also valid where the WKB approximation holds.

- Finally, it is clear that (2-1.1) cannot continue to hold for vanishingly small waves since $\mathrm{Ro}^{(w)}(\propto k_*)$ cannot continue to be small enough to neglect nonlinear terms in the wave variables. Therefore the eikonal regime can only describe waves up to the scale $(k_*/K_*) = O(\mathrm{Ro}^{-1}U_*/u_*)$, which is when $\mathrm{Ro}^{(w)} = O(1)$, and beyond this point the dynamics cannot be meaningfully described in terms of waves, and instead exhibit full nonlinear turbulence.

Figure 2-1 indicates which theories and approaches are valid for the relative spatial scale separation of the waves and background flow, characterised by k_*/K_*, subject to a time scale separation of order Ro. The labels refer to the names by which the theories or regimes are typically known. It is worth pointing out that the dynamics in the overlapping diffusion and eikonal regimes are both described by the WKB approximation; the difference is that one can exploit weakness to derive a kinetic equation that has been averaged over realisations of the background flow in the

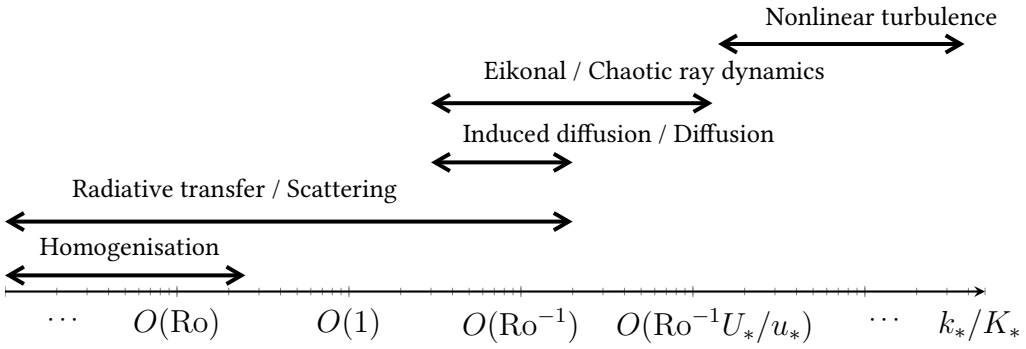

Figure 2-1. The main regimes of wave scattering by background flows.

diffusion regime, whereas the eikonal description is in terms of a stochastic equation with coefficients that depend on the particular realisation of the flow. In this thesis we consider the propagation of waves in the *scattering* and *diffusion* regimes.

Kinetic equations

Kinetic equations originally appeared in the context of statistical mechanics, where they describe the transport of particles due to multiple collisions and scatterings in position- and momentum-space through the evolution of a probability distribution, which characterises the macroscopic state of the system in an averaged sense. Kinetic theory is generally concerned with deriving closed-form equations for macroscopic quantities, such as the average energy density spectrum and other higher order correlations of fields. A well-known example of such an equation in statistical mechanics is the Boltzmann transport equation.

In an analogous way we may consider IGW fields to be made up of wave packets with a small spread of wave numbers centred on $\boldsymbol{k}$, and occupying a small region about a point $\boldsymbol{x}$ (Müller *et al.*, 1986). Such wave packets can overlap and fill space, and in the linear wave approximation are regarded as independent of each other. When these wave packets propagate through a randomly inhomogeneous background flow, at each point $\boldsymbol{x}$ they interact with the flow and scatter to a new state with wave vector $\boldsymbol{k}'$ at a rate that depends on details of the flow. In analogy with the statistical mechanical description of particles, we seek to describe the net macroscopic effect of wave scattering in terms of averaged statistical quantities. Depending on the assumptions made on the nature of the interactions there are different ways to achieve

such a description (Hasselmann, 1962; McComas and Bretherton, 1977; Müller and Olbers, 1975; Meiss and Watson, 1982; Lelong and Riley, 1991; Nazarenko, 2011; Eden *et al.*, 2019).

A powerful formalism evinced by Ryzhik *et al.* (1996) provides a way to construct wave kinetic equations in terms of the Wigner function, which is an energy-density-like function defined on $(\boldsymbol{x}, \boldsymbol{k})$ phase-space. The theory treats waves as having undergone multiple weak interactions with a randomly fluctuating medium over length scales typically much greater than the 'micro'-scale of the fluctuations. The precise mathematical form of the macroscopic model depends upon the distinguished regime under consideration. The general form is given by

$$\partial_t a + \nabla_{\boldsymbol{k}}\omega \cdot \nabla_{\boldsymbol{x}} a - \nabla_{\boldsymbol{x}}\omega \cdot \nabla_{\boldsymbol{k}} a = \mathcal{L}_{sc} a, \tag{2-1.4}$$

with $a(\boldsymbol{x}, \boldsymbol{k}, t)$ the energy density $\omega(\boldsymbol{x}, \boldsymbol{k})$ the dispersion relation of the linear waves, and $\mathcal{L}_{sc}$ a scattering operator. We emphasise that $a(\boldsymbol{x}, \boldsymbol{k}, t)$ is a phase-space energy density and it is defined in terms of a Wigner transform with details given in §2-2. Determining $\mathcal{L}_{sc}$ for a given system is a challenge, with the particular form of the operator depending on the specific details of the model (Ryzhik, 2014; Bal *et al.*, 2010).

In the scattering regime $\mathcal{L}_{sc}$ takes the form of a scattering integral given by

$$\mathcal{L}_{sc} a(\boldsymbol{x}, \boldsymbol{k}, t) = \int_{\mathbb{R}^d} \sigma(\boldsymbol{k}, \boldsymbol{k}') a(\boldsymbol{x}, \boldsymbol{k}', t) \mathrm{d}\boldsymbol{k}' - \int_{\mathbb{R}^d} \sigma(\boldsymbol{k}', \boldsymbol{k}) \mathrm{d}\boldsymbol{k}' a(\boldsymbol{x}, \boldsymbol{k}, t), \tag{2-1.5}$$

where $\sigma(\boldsymbol{k}, \boldsymbol{k}')$ is the differential scattering cross-section, a function that encodes the effect of the background flow. In this regime we can identify (2-1.4) with a linearised form of the Boltzmann transport equation, where instead of considering collisions of particles, the equation describes the net effect of multiple triadic interactions of wave and flow modes. The rest of this chapter is spent deriving the kinetic equation in the scattering regime, and further discussion about the analysis of the equation is relegated to later chapters where we derive the cross-section for different models.

In appendix D we show that, in the appropriate limit for the wave diffusion regime, this scattering integral operator reduces to a diffusion in wavenumber space in the form

$$\mathcal{L}_{sc} a(\boldsymbol{x}, \boldsymbol{k}, t) = \nabla_{\boldsymbol{k}} \cdot \big(\mathbf{D}(\boldsymbol{k}) \cdot \nabla_{\boldsymbol{k}} a(\boldsymbol{x}, \boldsymbol{k}, t) \big) \tag{2-1.6}$$

where $\mathbf{D}$ is a diffusion tensor which is written explicitly in chapter 4 which, like $\sigma(\boldsymbol{k}, \boldsymbol{k}')$, encodes the effect of the background flow.

Note – For the remainder of this thesis, references to 'the kinetic equation' correspond to the transport equation (2-1.4) in the scattering regime with a scattering integral operator of the form (2-1.5), and references to 'the diffusion equation' are for the transport equation taking the diffusion operator (2-1.6).

2-2 The Wigner transform

The approach we take to deriving the kinetic equation, due to Ryzhik *et al.* (1996), involves recasting IGW fields in terms of their Wigner transform. We include this short section to describe what the Wigner transform is and what it represents for wave fields.

The basic definition of the Wigner transform of a field $\boldsymbol{\phi}(\boldsymbol{x}, t)$, with $\boldsymbol{x} \in \mathbb{R}^d$, is given by

$$W(\boldsymbol{x}, \boldsymbol{k}, t) = \int_{\mathbb{R}^d} \mathrm{e}^{\mathrm{i}\boldsymbol{k}\cdot\boldsymbol{y}} \boldsymbol{\phi}(\boldsymbol{x} - \boldsymbol{y}/2, t) \boldsymbol{\phi}^*(\boldsymbol{x} + \boldsymbol{y}/2, t) \frac{\mathrm{d}\boldsymbol{y}}{(2\pi)^d}, \tag{2-2.1}$$

where $\boldsymbol{\phi}^*$ denotes the complex conjugate for a scalar field, or Hermitian conjugate for a vector-valued function. Note that if $\boldsymbol{\phi}$ is an n-dimensional column vector, then W is an $n \times n$ matrix. The function W is referred to as the Wigner function, or properly as the Wigner distribution, after Eugene Wigner who introduced the definition (2-2.1) (Wigner, 1932).

There is a second definition of the Wigner function that is sometimes useful to work with, defined in terms of the Fourier transform of $\boldsymbol{\phi}$. We follow the convention of Ryzhik *et al.* (1996) who use the pair

$$\widehat{\boldsymbol{\phi}}(\boldsymbol{k}, t) = \int_{\mathbb{R}^d} \mathrm{e}^{\mathrm{i}\boldsymbol{k}\cdot\boldsymbol{x}} \boldsymbol{\phi}(\boldsymbol{x}, t) \frac{\mathrm{d}\boldsymbol{x}}{(2\pi)^d} \quad \text{and} \quad \boldsymbol{\phi}(\boldsymbol{x}, t) = \int_{\mathbb{R}^d} \mathrm{e}^{-\mathrm{i}\boldsymbol{k}\cdot\boldsymbol{x}} \widehat{\boldsymbol{\phi}}(\boldsymbol{k}, t) \mathrm{d}\boldsymbol{k}.$$

Inserting the transformed fields into (2-2.1) leads to the dual definition

$$W(\boldsymbol{x}, \boldsymbol{k}, t) = \int_{\mathbb{R}^d} \mathrm{e}^{\mathrm{i}\boldsymbol{p}\cdot\boldsymbol{x}} \widehat{\boldsymbol{\phi}}(-\boldsymbol{k} - \boldsymbol{p}/2, t) \widehat{\boldsymbol{\phi}}^*(-\boldsymbol{k} + \boldsymbol{p}/2, t) \mathrm{d}\boldsymbol{p}. \tag{2-2.2}$$

We note that the Wigner transform is invertible, up to a constant phase, with

$$\boldsymbol{\phi}(\boldsymbol{x},t)\boldsymbol{\phi}^*(0,t) = \int_{\mathbb{R}^d} \mathrm{e}^{\mathrm{i}\boldsymbol{k}\cdot\boldsymbol{x}} \mathsf{W}(\boldsymbol{x}/2,\boldsymbol{k},t)\mathrm{d}\boldsymbol{k},$$

or similarly for the Fourier transformed field

$$\widehat{\boldsymbol{\phi}}(\boldsymbol{k},t)\widehat{\boldsymbol{\phi}}^*(0,t) = \int_{\mathbb{R}^d} \mathrm{e}^{\mathrm{i}\boldsymbol{k}\cdot\boldsymbol{x}} \mathsf{W}(\boldsymbol{x},-\boldsymbol{k}/2,t)\frac{\mathrm{d}\boldsymbol{x}}{(2\pi)^d}.$$

Basic properties of the Wigner function

From (2-2.1) and (2-2.2) we can note some interesting properties of the Wigner function. First we see that the Wigner function is Hermitian, so that $\mathsf{W}(\boldsymbol{x},\boldsymbol{k},t) = \mathsf{W}^*(\boldsymbol{x},\boldsymbol{k},t)$. Second is the integral property, otherwise known as the marginal or projection property, where

$$\int_{\mathbb{R}^d} \mathsf{W}(\boldsymbol{x},\boldsymbol{k},t)\mathrm{d}\boldsymbol{k} = \boldsymbol{\phi}(\boldsymbol{x},t)\boldsymbol{\phi}^*(\boldsymbol{x},t) \;\text{ and }\; \int_{\mathbb{R}^d} \mathsf{W}(\boldsymbol{x},-\boldsymbol{k},t)\frac{\mathrm{d}\boldsymbol{x}}{(2\pi)^d} = \widehat{\boldsymbol{\phi}}(\boldsymbol{k},t)\widehat{\boldsymbol{\phi}}^*(\boldsymbol{k},t).$$

This property, relating the Wigner function to quadratic functions of the fields, gives the Wigner function a sense of being an energy density in phase space. There is an issue with this interpretation though; the Wigner function as defined by (2-2.1) or (2-2.2) is not necessarily a positive function.

Furthermore, the basic definition of the transform is troublesome for studying rapidly oscillating fields, as is easily demonstrated. Consider a simple plane wave defined by $\phi(\boldsymbol{x}/\varepsilon) = A\,\mathrm{e}^{\mathrm{i}\boldsymbol{k}_0\cdot\boldsymbol{x}/\varepsilon}$, with a fixed wavenumber $\boldsymbol{k}_0 \in \mathbb{R}^d$, scalar amplitude A, and $\varepsilon > 0$ a small parameter. Then, its Wigner transform is given by

$$\begin{aligned}\mathsf{W}(\boldsymbol{x}/\varepsilon,\boldsymbol{k}) &= \int_{\mathbb{R}^d} \mathrm{e}^{\mathrm{i}\boldsymbol{k}\cdot\boldsymbol{y}} A\,\mathrm{e}^{\mathrm{i}\boldsymbol{k}_0\cdot(\boldsymbol{x}-\boldsymbol{y}/2)/\varepsilon} A^*\,\mathrm{e}^{-\mathrm{i}\boldsymbol{k}_0\cdot(\boldsymbol{x}+\boldsymbol{y}/2)/\varepsilon}\frac{\mathrm{d}\boldsymbol{y}}{(2\pi)^d} \\ &= |A|^2\delta(\boldsymbol{k}-\boldsymbol{k}_0/\varepsilon).\end{aligned}$$

Clearly this function (distribution) does not have a limit as $\varepsilon \to 0$, corresponding to waves that are rapidly oscillating in space.

Fortunately, the Wigner transform has a useful scaling property which can be used to obtain a modified definition of the Wigner transform suitable for high frequency fields, known as the *semiclassical Wigner transform* (Ryzhik, 2014) or *scaled Wigner*

transform (Ryzhik *et al.*, 1996). Suppose there are two fields $u(\boldsymbol{x})$ and $v(\boldsymbol{x})$, with $\boldsymbol{x} \in \mathbb{R}^d$, related by a rescaling of the form

$$v(\boldsymbol{x}) = a^{d/2} u(a\boldsymbol{x}),$$

with $a > 0$. Then the scaling property of the Wigner transform says that their respective Wigner functions are related by

$$W_v(\boldsymbol{x}, a\boldsymbol{k}) = W_u(a\boldsymbol{x}, \boldsymbol{k}), \tag{2-2.3}$$

where the subscript denotes the field being transformed according to (2-2.1).

Scaled Wigner transform

Taking $a = 1/\varepsilon$ in (2-2.3) and setting $u(\boldsymbol{x}/\varepsilon) =: u_\varepsilon(\boldsymbol{x})$, we see that

$$W_v(\boldsymbol{x}, \boldsymbol{k}/\varepsilon) = \varepsilon^{-d} W_{u_\varepsilon}(\boldsymbol{x}, \boldsymbol{k}/\varepsilon) = W_u(\boldsymbol{x}/\varepsilon, \boldsymbol{k}).$$

This suggests that if we have a wave field that varies on the small/fast scales $(\boldsymbol{x}/\varepsilon, t/\varepsilon)$, we can take a rescaled field $\boldsymbol{\phi}_\varepsilon(\boldsymbol{x}, t) := \boldsymbol{\phi}(\boldsymbol{x}/\varepsilon, t/\varepsilon)$ and introduce its scaled Wigner transform defined by

$$W^\varepsilon(\boldsymbol{x}, \boldsymbol{k}, t) = \varepsilon^{-d} W(\boldsymbol{x}, \boldsymbol{k}/\varepsilon, t) = \int_{\mathbb{R}^d} \mathrm{e}^{\mathrm{i}\boldsymbol{k}\cdot\boldsymbol{y}} \boldsymbol{\phi}_\varepsilon(\boldsymbol{x} - \varepsilon\boldsymbol{y}/2, t) \boldsymbol{\phi}_\varepsilon^*(\boldsymbol{x} + \varepsilon\boldsymbol{y}/2, t) \frac{\mathrm{d}\boldsymbol{y}}{(2\pi)^d}. \tag{2-2.4}$$

This definition makes it possible to follow the evolution of the Wigner function over large scales, like the envelope scale of a wave packet, while picking up variations on the small scale of the wave phase. We note that generally the scaled transform W^ε remains positive semi-definite for all time in the limit that ε goes to zero, which is important as it is closely related to the energy of the system. There is no guarantee of positivity for initially positive Wigner functions with finite values of ε, though local averages over a region of size $\sqrt{\varepsilon}$ are non-negative (Bal *et al.*, 2010, §3.1.2). The energy density of the waves can be written

$$\mathcal{E}(\boldsymbol{x}, t) = \frac{1}{2} \boldsymbol{\phi}_\varepsilon^* \boldsymbol{M} \boldsymbol{\phi}_\varepsilon,$$

with M a Hermitian matrix. This is found from the scaled Wigner function as

$$\mathcal{E}(\boldsymbol{x},t) = \frac{1}{2}\int_{\mathbb{R}^d} \mathrm{tr}\big(\mathsf{M}\mathsf{W}^\varepsilon(\boldsymbol{x},\boldsymbol{k},t)\big)\mathrm{d}\boldsymbol{k}. \tag{2-2.5}$$

In addition to fixing concerns about negative energy densities, the definition (2-2.4) turns out to have the correct scaling for studying the rapidly oscillating waves. Returning to the plane wave example and now allowing the wave amplitude to vary on the large scale, with $\phi(\boldsymbol{x}/\varepsilon) = A(\boldsymbol{x})\,\mathrm{e}^{\mathrm{i}\boldsymbol{k}_0\cdot\boldsymbol{x}/\varepsilon} = \phi_\varepsilon(\boldsymbol{x})$, we find that its scaled transform is given by

$$\begin{aligned}\mathsf{W}^\varepsilon(\boldsymbol{x},\boldsymbol{k}) &= \int_{\mathbb{R}^d} \mathrm{e}^{\mathrm{i}\boldsymbol{k}\cdot\boldsymbol{y}} A(\boldsymbol{x}-\varepsilon\tfrac{\boldsymbol{y}}{2})\,\mathrm{e}^{\mathrm{i}\boldsymbol{k}_0\cdot(\boldsymbol{x}/\varepsilon-\boldsymbol{y}/2)} A^*(\boldsymbol{x}+\varepsilon\tfrac{\boldsymbol{y}}{2})\,\mathrm{e}^{-\mathrm{i}\boldsymbol{k}_0\cdot(\boldsymbol{x}/\varepsilon+\boldsymbol{y}/2)}\frac{\mathrm{d}\boldsymbol{y}}{(2\pi)^d}\\ &= |A(\boldsymbol{x})|^2\delta(\boldsymbol{k}-\boldsymbol{k}_0)+O(\varepsilon).\end{aligned}$$

Clearly this transform is well defined in the limit $\varepsilon \to 0$, and it correctly identifies that the wave energy density is concentrated on the wavenumber $\boldsymbol{k}_0$ at all points in space.

Finally we note that, as before, the scaled Wigner transform has an $\boldsymbol{x}$–$\boldsymbol{k}$ duality such that we may equivalently define the scaled transform in terms of the Fourier transformed fields as

$$\mathsf{W}^\varepsilon(\boldsymbol{x},\boldsymbol{k},t) = \varepsilon^{-d}\int_{\mathbb{R}^d} \mathrm{e}^{\mathrm{i}\boldsymbol{p}\cdot\boldsymbol{x}}\widehat{\boldsymbol{\phi}}_\varepsilon(-\boldsymbol{k}/\varepsilon-\boldsymbol{p}/2,t)\widehat{\boldsymbol{\phi}}_\varepsilon(-\boldsymbol{k}/\varepsilon+\boldsymbol{p}/2,t)\mathrm{d}\boldsymbol{p}. \tag{2-2.6}$$

2-3 Kinetic equation derivation

This section shows how to pass from the equations for wave propagation in a random flow to a kinetic equation governing the evolution of a wavenumber-resolving energy density, given in terms of a Wigner function. The derivation is in general terms so we do not write the explicit form for many of the expressions in this section, but point to the explicit representations that appear in later chapters for the different models. We begin by introducing some of the essential mathematical ingredients for the derivation.

2-3.1 Basic ingredients

To begin we rewrite (2-1.1) in a form that makes clear the dependencies of the operators as

$$\partial_t \boldsymbol{\phi} + [\boldsymbol{L}(\partial_{\boldsymbol{x}}) + \sqrt{\varepsilon}\boldsymbol{N}(\boldsymbol{x}, \partial_{\boldsymbol{x}}, \sqrt{\varepsilon}t)]\boldsymbol{\phi} = 0. \tag{2-3.1}$$

Here, $\boldsymbol{\phi}(\boldsymbol{x}, t)$ is a vector grouping the dynamical variables of the IGWs (see (3-2.9), (5-2.5)). We have chosen the scaling $\varepsilon = \mathrm{Ro}^2$ in order to keep the following derivation in closer correspondence with the mathematical literature (e.g. Bal *et al.* (2010); Ryzhik *et al.* (1996)). Unlike Ryzhik *et al.* (1996), however, here the matrix operators $\boldsymbol{L}(\partial_{\boldsymbol{x}})$ and $\boldsymbol{N}(\boldsymbol{x}, \partial_{\boldsymbol{x}}, \sqrt{\varepsilon}t)$ are pseudodifferential operators in general, and $\boldsymbol{N}$ depends not only on space but also on time through the slowly-evolving background flow (cf. Ryzhik *et al.* (1996) eq. (4.1)). We summarise some of the similarities with and departures from the derivation presented by Ryzhik *et al.* (1996) at the end of this chapter. It is assumed for this thesis that the background flow is written in terms of a streamfunction such that the velocity field of the geostrophic turbulence is given by $\boldsymbol{U}(\boldsymbol{x}, \sqrt{\varepsilon}t) = \nabla^{\perp}\psi = (-\partial_y\psi, \partial_x\psi, 0)$. Further generalisations for the flow are possible but not considered in this thesis. We assume the convention for $\boldsymbol{N}$ that the derivatives $\partial_{\boldsymbol{x}}$ appear to the right of the $\boldsymbol{x}$-dependence, so

$$\begin{aligned}\boldsymbol{N}(\boldsymbol{x}, \partial_{\boldsymbol{x}})\boldsymbol{\phi}(\boldsymbol{x}, t) &= \int \boldsymbol{N}(\boldsymbol{x}, -\mathrm{i}\boldsymbol{k})\widehat{\boldsymbol{\phi}}(\boldsymbol{k}, t)\, \mathrm{e}^{-\mathrm{i}\boldsymbol{k}\cdot\boldsymbol{x}}\mathrm{d}\boldsymbol{k} \\ &= \iint \widehat{\boldsymbol{N}}(\boldsymbol{p}, -\mathrm{i}\boldsymbol{k})\widehat{\boldsymbol{\phi}}(\boldsymbol{k}, t)\, \mathrm{e}^{-\mathrm{i}(\boldsymbol{k}+\boldsymbol{p})\cdot\boldsymbol{x}}\mathrm{d}\boldsymbol{k}\mathrm{d}\boldsymbol{p}. \end{aligned} \tag{2-3.2}$$

Explicit representations of these operators appear in later chapters ((3-2.10), (3-2.11), (5-2.7), (5-2.8)). The matrix $\boldsymbol{L}$ appearing in the equations of motion (2-3.1) is known as the dispersion matrix, since its eigenvalues give the dispersion relation of the IGWs. Generally it can also depend on space as $\boldsymbol{L}(\boldsymbol{x}, \partial_{\boldsymbol{x}})$, for example through spatially varying coefficients f and N in (1-2.6), but we do not include such dependencies in this thesis. Replacing its argument $\partial_{\boldsymbol{x}}$ by the symbol $\mathrm{i}\boldsymbol{k}$ leads to an eigenvalue equation of the form

$$\boldsymbol{L}(\mathrm{i}\boldsymbol{k})\boldsymbol{b}_j(\boldsymbol{k}) = \mathrm{i}\omega_j(\boldsymbol{k})\boldsymbol{b}_j(\boldsymbol{k}), \quad j = 0, \pm \tag{2-3.3}$$

with eigenvalues $\omega_0 = 0$, $\omega_{\pm} = \pm\omega$ for the systems we consider. As in Chapter 1, the zero eigenvalue corresponds to the vortical mode of the system. Since the

vortical mode is accounted for by a prescribed geostrophic background flow, it does not appear in any of the following derivation. The remaining eigenvalues correspond to the dispersion relation for IGWs propagating in opposite directions, for example as in (3-2.13) and (5-2.2). We note that the eigenvectors $\boldsymbol{b}$ contain the polarisation information described in Chapter 1 §1-2.

The energy density associated with the linear part of (2-3.1), that is with taking $\varepsilon \to 0$, can be written in terms of a weighted inner-product as

$$\mathcal{E}(\boldsymbol{x}, t) = \tfrac{1}{2}\langle \boldsymbol{\phi}, \boldsymbol{\phi} \rangle_{\boldsymbol{M}},$$

with

$$\langle \boldsymbol{f}, \boldsymbol{g} \rangle_{\boldsymbol{M}} := \boldsymbol{f}^* \boldsymbol{M} \boldsymbol{g},$$

where $\boldsymbol{M}$ is a Hermitian matrix, as in (3-2.12) and (5-3.3). The eigenvectors of (2-3.3), as shown in (3-2.14) and (5-3.1), can be chosen to be orthonormal with respect to this inner product such that

$$\langle \boldsymbol{b}_i, \boldsymbol{b}_j \rangle_{\boldsymbol{M}} = \delta_{ij}, \quad j = 0, \pm.$$

In addition to the right eigenvectors $\boldsymbol{b}_j$, we also use the left eigenvectors $\boldsymbol{c}_j$ which satisfy

$$\boldsymbol{c}_j \boldsymbol{L} = \mathrm{i}\omega_j \boldsymbol{c}_j, \quad \boldsymbol{c}_j = \boldsymbol{b}_j^* \boldsymbol{M} \quad \text{and} \quad \boldsymbol{c}_i \boldsymbol{b}_j = \delta_{ij}. \tag{2-3.4}$$

We note that the eigenvectors $\boldsymbol{b}$ are column vectors and $\boldsymbol{c}$ are row vectors.

It is convenient to rescale the space and time coordinates as $(\boldsymbol{x}, t) \mapsto (\boldsymbol{x}/\varepsilon, t/\varepsilon)$ and define $\boldsymbol{\phi}_\varepsilon(\boldsymbol{x}, t) := \boldsymbol{\phi}(\boldsymbol{x}/\varepsilon, t/\varepsilon)$. Under this rescaling, the equations of motion (2-3.1) take the form

$$\varepsilon \partial_t \boldsymbol{\phi}_\varepsilon + \big[\boldsymbol{L}(\varepsilon \partial_{\boldsymbol{x}}) + \sqrt{\varepsilon}\boldsymbol{N}(\boldsymbol{x}/\varepsilon, \varepsilon\partial_{\boldsymbol{x}}, t/\sqrt{\varepsilon})\big]\boldsymbol{\phi}_\varepsilon = 0. \tag{2-3.5}$$

2-3.2 Wigner function evolution equation

We obtain an evolution equation for the Wigner function by differentiating (2-2.4) with respect to t and substituting (2-3.5). This gives

$$\begin{aligned}
&\varepsilon\partial_t W^\varepsilon(\boldsymbol{x},\boldsymbol{k},t)\\
&\quad=\varepsilon\int_{\mathbb{R}^d}\mathrm{e}^{\mathrm{i}\boldsymbol{k}\cdot\boldsymbol{y}}\Big(\Big[\partial_t\boldsymbol{\phi}_\varepsilon(t,\boldsymbol{x}-\tfrac{\varepsilon\boldsymbol{y}}{2})\Big]\boldsymbol{\phi}_\varepsilon^*(t,\boldsymbol{x}+\tfrac{\varepsilon\boldsymbol{y}}{2})+\boldsymbol{\phi}_\varepsilon(t,\boldsymbol{x}-\tfrac{\varepsilon\boldsymbol{y}}{2})\Big[\partial_t\boldsymbol{\phi}_\varepsilon^*(t,\boldsymbol{x}+\tfrac{\varepsilon\boldsymbol{y}}{2})\Big]\Big)\frac{\mathrm{d}\boldsymbol{y}}{(2\pi)^d}\\
&\quad=-\int_{\mathbb{R}^d}\mathrm{e}^{\mathrm{i}\boldsymbol{k}\cdot\boldsymbol{y}}\Big[\boldsymbol{L}(\varepsilon\partial_{\boldsymbol{x}})+\sqrt{\varepsilon}\boldsymbol{N}(\tfrac{\boldsymbol{x}}{\varepsilon}-\tfrac{\boldsymbol{y}}{2},\varepsilon\partial_{\boldsymbol{x}},\tfrac{t}{\sqrt{\varepsilon}})\Big]\boldsymbol{\phi}_\varepsilon(t,\boldsymbol{x}-\tfrac{\varepsilon\boldsymbol{y}}{2})\boldsymbol{\phi}_\varepsilon^*(t,\boldsymbol{x}+\tfrac{\varepsilon\boldsymbol{y}}{2})\frac{\mathrm{d}\boldsymbol{y}}{(2\pi)^d}+\text{c.c.},
\end{aligned}$$

where c.c. denotes the complex conjugate of the term preceding it. Rewriting $\boldsymbol{\phi}_\varepsilon$ and $\boldsymbol{N}$ in terms of their Fourier transforms and making use of (2-2.6), we find that

$$\begin{aligned}
&\varepsilon\partial_t W^\varepsilon(\boldsymbol{x},\boldsymbol{k},t)+\overbrace{\Big[\boldsymbol{L}(\mathrm{i}\boldsymbol{k}+\tfrac{\varepsilon}{2}\partial_{\boldsymbol{x}})W^\varepsilon(\boldsymbol{x},\boldsymbol{k})+\text{c.c.}\Big]}^{:=\mathcal{Q}^\varepsilon W^\varepsilon}\\
&\quad+\sqrt{\varepsilon}\underbrace{\Big[\int\mathrm{e}^{-\mathrm{i}\boldsymbol{p}\cdot\boldsymbol{\xi}}\widehat{\boldsymbol{N}}(\boldsymbol{p},\mathrm{i}(\boldsymbol{k}+\tfrac{\boldsymbol{p}}{2})+\tfrac{\varepsilon}{2}\partial_{\boldsymbol{x}},\tfrac{t}{\sqrt{\varepsilon}})W^\varepsilon(\boldsymbol{x},\boldsymbol{k}+\tfrac{\boldsymbol{p}}{2})\mathrm{d}\boldsymbol{p}+\text{c.c.}\Big]}_{:=\mathcal{P}^\varepsilon W^\varepsilon}=0. \quad (2\text{-}3.6)
\end{aligned}$$

Scattering effects due to interactions of waves with the background flow are controlled by the third term, $\mathcal{P}^\varepsilon W^\varepsilon$. To derive it, we have introduced the fast-space variable $\boldsymbol{\xi}:=\boldsymbol{x}/\varepsilon$ and the Fourier transform $\widehat{\boldsymbol{N}}$ of $\boldsymbol{N}$ defined by

$$\boldsymbol{N}(\boldsymbol{\xi},\cdot)=\int_{\mathbb{R}^d}\mathrm{e}^{-\mathrm{i}\boldsymbol{p}\cdot\boldsymbol{\xi}}\widehat{\boldsymbol{N}}(\boldsymbol{p},\cdot)\mathrm{d}\boldsymbol{p}.$$

We now derive the asymptotic limit of (2-3.6) using a multiscale expansion. Defining the intermediate time variable $\tau:=t/\sqrt{\varepsilon}$ to cater for the time dependence of the streamfunction, we expand

$$W^\varepsilon(\boldsymbol{x},\boldsymbol{\xi},\boldsymbol{k},t,\tau)=W^{(0)}(\boldsymbol{x},\boldsymbol{k},t)+\sqrt{\varepsilon}W^{(1)}(\boldsymbol{x},\boldsymbol{\xi},\boldsymbol{k},t,\tau)+\varepsilon W^{(2)}(\boldsymbol{x},\boldsymbol{\xi},\boldsymbol{k},t,\tau)+O(\varepsilon^{3/2}), \quad (2\text{-}3.7)$$

where we have anticipated that the leading-order term depends on the slow variables

only. The differential operators are then expanded as

$$\partial_{\boldsymbol{x}} \mapsto \partial_{\boldsymbol{x}} + \varepsilon^{-1}\partial_{\boldsymbol{\xi}}, \quad \partial_t \mapsto \partial_t + \varepsilon^{-1/2}\partial_\tau,$$

where $\boldsymbol{x}$ and $\boldsymbol{\xi}$, t and τ are treated as independent variables, leading to the expansion

$$\mathcal{Q}^\varepsilon = \mathcal{Q}_0 + \varepsilon\mathcal{Q}_1 + O(\varepsilon^2), \quad \mathcal{P}^\varepsilon = \mathcal{P}_0 + \varepsilon\mathcal{P}_1 + O(\varepsilon^2) \tag{2-3.8}$$

of the operators in (2-3.6). It turns out that only the leading order term $\mathcal{P}_0$ is required for the derivation of the kinetic equation.

The operators in (2-3.8) can be written explicitly through their action on an arbitrary function $Z(\boldsymbol{x}, \boldsymbol{\xi}, \boldsymbol{k})$:

$$\begin{aligned}
\widetilde{\mathcal{Q}}_0 Z(\boldsymbol{x}, \boldsymbol{\xi}, \boldsymbol{k}) &= \boldsymbol{L}(\mathrm{i}\boldsymbol{k} + \tfrac{1}{2}\partial_{\boldsymbol{\xi}})Z(\boldsymbol{x}, \boldsymbol{\xi}, \boldsymbol{k}) + \text{c.c.} \\
\widetilde{\mathcal{Q}}_1 Z(\boldsymbol{x}, \boldsymbol{\xi}, \boldsymbol{k}) &= \frac{1}{2\mathrm{i}}\big[\nabla_{\boldsymbol{k}}\boldsymbol{L}(\mathrm{i}\boldsymbol{k} + \tfrac{1}{2}\partial_{\boldsymbol{\xi}})\big] \cdot \nabla_{\boldsymbol{x}} Z(\boldsymbol{x}, \boldsymbol{\xi}, \boldsymbol{k}) + \text{c.c.} \\
\widetilde{\mathcal{P}}_0 Z(\boldsymbol{x}, \boldsymbol{\xi}, \boldsymbol{k}) &= \int_{\mathbb{R}^d} \mathrm{e}^{-\mathrm{i}\boldsymbol{p}\cdot\boldsymbol{\xi}} \widehat{\boldsymbol{N}}(\boldsymbol{p}, \mathrm{i}(\boldsymbol{k} + \tfrac{\boldsymbol{p}}{2}) + \tfrac{1}{2}\partial_{\boldsymbol{\xi}}, \tau) Z(\boldsymbol{x}, \boldsymbol{\xi}, \boldsymbol{k} + \tfrac{\boldsymbol{p}}{2})\mathrm{d}\boldsymbol{p} + \text{c.c.}
\end{aligned}$$

We have decorated the operators with a tilde to highlight the presence of $\partial_{\boldsymbol{\xi}}$ in their definition; the tildes will be removed whenever this dependence disappears.

Substituting the operators into (2-3.6) gives us the evolution equation for the Wigner function as

$$\Big[\frac{1}{\varepsilon}\widetilde{\mathcal{Q}}_0 + \frac{1}{\sqrt{\varepsilon}}\Big(\widetilde{\mathcal{P}}_0 + \frac{\partial}{\partial\tau}\Big) + \Big(\widetilde{\mathcal{Q}}_1 + \frac{\partial}{\partial t}\Big)\Big] \boldsymbol{W}^\varepsilon(\boldsymbol{x}, \boldsymbol{\xi}, \boldsymbol{k}, t, \tau) = 0. \tag{2-3.9}$$

Introducing the expansion (2-3.7) then leads to a hierarchy of equations to be solved at each order in ε.

The leading-order equation is

$$\mathcal{Q}_0 \boldsymbol{W}^{(0)} = \boldsymbol{L}(\mathrm{i}\boldsymbol{k})\boldsymbol{W}^{(0)}(\boldsymbol{x}, \boldsymbol{k}, t) + \text{c.c.} = 0. \tag{2-3.10}$$

The eigenvalues of $\boldsymbol{L}$ are purely imaginary, so this equation is satisfied by taking $\boldsymbol{W}^{(0)}$ in the form of a linear combination of the eigenvectors of the dispersion matrix. Defining the matrices

$$\boldsymbol{B}_j(\boldsymbol{k}) = \boldsymbol{b}_j(\boldsymbol{k})\boldsymbol{b}_j^*(\boldsymbol{k}),$$

the leading order Wigner function is thus given by

$$W^{(0)}(\boldsymbol{x},\boldsymbol{k},t)=\sum_{j=\pm}a_j(\boldsymbol{x},\boldsymbol{k},t)\boldsymbol{B}_j(\boldsymbol{k}). \tag{2-3.11}$$

The so-far undetermined amplitudes $a_j(\boldsymbol{x},\boldsymbol{k},t)$ are real because the Wigner function is Hermitian. These amplitudes are the phase-space energy densities discussed in §2-1.

At $O(\varepsilon^{-1/2})$, we find

$$\widetilde{\mathcal{Q}}_0 W^{(1)}(\boldsymbol{x},\boldsymbol{\xi},\boldsymbol{k},t,\tau)=-\mathcal{P}_0 W^{(0)}(\boldsymbol{x},\boldsymbol{k},t), \tag{2-3.12}$$

where we have used that $\partial_\tau W^{(0)}=0$. To solve (2-3.12), we rewrite $W^{(1)}$ in terms of its Fourier transform with respect to $\boldsymbol{\xi}$,

$$W^{(1)}(\boldsymbol{x},\boldsymbol{\xi},\boldsymbol{k},t,\tau)=\int_{\mathbb{R}^d}\mathrm{e}^{-\mathrm{i}\boldsymbol{p}\cdot\boldsymbol{\xi}}\widehat{W}^{(1)}(\boldsymbol{x},\boldsymbol{p},\boldsymbol{k},t,\tau)\mathrm{d}\boldsymbol{p}.$$

Substituting this into (2-3.12) yields

$$\begin{aligned}\boldsymbol{L}(\mathrm{i}(\boldsymbol{k}-\tfrac{\boldsymbol{p}}{2}))\widehat{W}^{(1)}(\boldsymbol{p},\boldsymbol{k})+\Big[\boldsymbol{L}(\mathrm{i}(\boldsymbol{k}+\tfrac{\boldsymbol{p}}{2}))\widehat{W}^{(1)}(-\boldsymbol{p},\boldsymbol{k})\Big]^*+\theta\widehat{W}^{(1)}(\boldsymbol{p},\boldsymbol{k})\\ =-\widehat{\boldsymbol{N}}\big(\boldsymbol{p},\mathrm{i}(\boldsymbol{k}+\tfrac{\boldsymbol{p}}{2})\big)W^{(0)}(\boldsymbol{k}+\tfrac{\boldsymbol{p}}{2})-\Big[\widehat{\boldsymbol{N}}\big(-\boldsymbol{p},\mathrm{i}(\boldsymbol{k}-\tfrac{\boldsymbol{p}}{2})\big)W^{(0)}(\boldsymbol{k}-\tfrac{\boldsymbol{p}}{2})\Big]^*,\end{aligned}$$

where we have suppressed dependencies on $\boldsymbol{x}$, t and τ for conciseness. Following Ryzhik *et al.* (1996), we have introduced a regularisation parameter $\theta>0$ which will be taken to zero at a later stage.

Since the Wigner transform is Hermitian, $\widehat{W}^{(1)}(\boldsymbol{p},\boldsymbol{k})=\widehat{W}^{(1)*}(-\boldsymbol{p},\boldsymbol{k})$. Using this, expanding $W^{(0)}$ according to (2-3.11), and pre- and post-multiplying the resulting expression by $\boldsymbol{c}_n(\boldsymbol{k}-\boldsymbol{p}/2)$ and $\boldsymbol{c}_m^*(\boldsymbol{k}+\boldsymbol{p}/2)$ (with $\boldsymbol{c}_n$ the left eigenvector defined

in (2-3.4)) gives

$$-\Big(\mathrm{i}(\omega_n(\boldsymbol{k}-\tfrac{\boldsymbol{p}}{2})-\omega_m(\boldsymbol{k}+\tfrac{\boldsymbol{p}}{2}))+\theta\Big)\boldsymbol{c}_n(\boldsymbol{k}-\tfrac{\boldsymbol{p}}{2})\widehat{W}^{(1)}(\boldsymbol{p},\boldsymbol{k})\boldsymbol{c}_m^*(\boldsymbol{k}+\tfrac{\boldsymbol{p}}{2})$$
$$=\sum_{i=\pm}a_i(\boldsymbol{k}+\tfrac{\boldsymbol{p}}{2})\boldsymbol{c}_n(\boldsymbol{k}-\tfrac{\boldsymbol{p}}{2})\widehat{\boldsymbol{N}}(\boldsymbol{p},\mathrm{i}(\boldsymbol{k}+\tfrac{\boldsymbol{p}}{2}))\boldsymbol{b}_i(\boldsymbol{k}+\tfrac{\boldsymbol{p}}{2})\boldsymbol{b}_i^*(\boldsymbol{k}+\tfrac{\boldsymbol{p}}{2})\boldsymbol{c}_m^*(\boldsymbol{k}+\tfrac{\boldsymbol{p}}{2})$$
$$+\sum_{j=\pm}a_j(\boldsymbol{k}-\tfrac{\boldsymbol{p}}{2})\boldsymbol{c}_n(\boldsymbol{k}-\tfrac{\boldsymbol{p}}{2})\boldsymbol{b}_j(\boldsymbol{k}-\tfrac{\boldsymbol{p}}{2})\boldsymbol{b}_j^*(\boldsymbol{k}-\tfrac{\boldsymbol{p}}{2})\widehat{\boldsymbol{N}}^*(-\boldsymbol{p},\mathrm{i}(\boldsymbol{k}-\tfrac{\boldsymbol{p}}{2}))\boldsymbol{c}_m^*(\boldsymbol{k}+\tfrac{\boldsymbol{p}}{2}). \tag{2-3.13}$$

It is convenient to extract the linear dependence of $\widehat{\boldsymbol{N}}$ on the streamfunction by defining a matrix $\widehat{\boldsymbol{U}}(\boldsymbol{p},\mathrm{i}\boldsymbol{q})$ such that

$$\widehat{\boldsymbol{N}}(\boldsymbol{p},\mathrm{i}\boldsymbol{q},\tau)=\widehat{\boldsymbol{U}}(\boldsymbol{p},\mathrm{i}\boldsymbol{q})\widehat{\psi}(\boldsymbol{p},\tau). \tag{2-3.14}$$

We now decompose $\widehat{W}^{(1)}$ using the vectors $\boldsymbol{b}_i(\boldsymbol{k})$, which form a complete basis, as

$$\widehat{W}^{(1)}(\boldsymbol{x},\boldsymbol{p},\boldsymbol{k},t,\tau)=\sum_{m,n=\pm}\alpha_{mn}(\boldsymbol{x},\boldsymbol{p},\boldsymbol{k},t,\tau)\boldsymbol{b}_n(\boldsymbol{k}-\tfrac{\boldsymbol{p}}{2})\boldsymbol{b}_m^*(\boldsymbol{k}+\tfrac{\boldsymbol{p}}{2}).$$

Using this along with the orthonormality of the eigenvectors we finally write the solution

$$\widehat{W}^{(1)}(\boldsymbol{x},\boldsymbol{p},\boldsymbol{k},t,\tau)=\sum_{m,n=\pm}\Big[a_m(\boldsymbol{x},\boldsymbol{k}+\tfrac{\boldsymbol{p}}{2},t)\boldsymbol{c}_n(\boldsymbol{k}-\tfrac{\boldsymbol{p}}{2})\widehat{\boldsymbol{U}}(\boldsymbol{p},\mathrm{i}(\boldsymbol{k}+\tfrac{\boldsymbol{p}}{2}))\boldsymbol{b}_m(\boldsymbol{k}+\tfrac{\boldsymbol{p}}{2})$$
$$+a_n(\boldsymbol{x},\boldsymbol{k}-\tfrac{\boldsymbol{p}}{2},t)\boldsymbol{b}_n^*(\boldsymbol{k}-\tfrac{\boldsymbol{p}}{2})\widehat{\boldsymbol{U}}^*(-\boldsymbol{p},\mathrm{i}(\boldsymbol{k}-\tfrac{\boldsymbol{p}}{2}))\boldsymbol{c}_m^*(\boldsymbol{k}+\tfrac{\boldsymbol{p}}{2})\Big]\frac{\boldsymbol{b}_n(\boldsymbol{k}-\frac{\boldsymbol{p}}{2})\boldsymbol{b}_m^*(\boldsymbol{k}+\frac{\boldsymbol{p}}{2})\widehat{\psi}(\boldsymbol{p},\tau)}{\mathrm{i}\big(\omega_m(\boldsymbol{k}+\frac{\boldsymbol{p}}{2})-\omega_n(\boldsymbol{k}-\frac{\boldsymbol{p}}{2})\big)-\theta},$$

where we have taken into account that $\widehat{\psi}(\boldsymbol{p})=\widehat{\psi}^*(-\boldsymbol{p})$. We note that this solution shows $W^{(1)}$ is linear in the streamfunction ψ.

The slow evolution of the leading-order Wigner function $W^{(0)}$ is controlled by the $O(1)$ term in the expansion of (2-3.9), given by

$$-\widetilde{\mathcal{Q}}_0W^{(2)}=(\widetilde{\mathcal{P}}_0+\partial_\tau)W^{(1)}+(\mathcal{Q}_1+\partial_t)W^{(0)}. \tag{2-3.15}$$

We assume that the streamfunction is a random process that is stationary in τ and

homogeneous in $\boldsymbol{\xi}$, with zero mean, $\langle\psi(\boldsymbol{\xi},\tau)\rangle = 0$, and covariance

$$\langle\psi(\boldsymbol{\xi},\tau)\psi(\boldsymbol{\xi}',\tau)\rangle = R(\boldsymbol{\xi}-\boldsymbol{\xi}'),$$

where $\langle\cdot\rangle$ denotes an ensemble average, or equivalently an average over $\boldsymbol{\xi}$. In terms of Fourier transforms, this implies that

$$\langle\widehat{\psi}(\boldsymbol{p})\widehat{\psi}(\boldsymbol{p}')\rangle = \widehat{R}(\boldsymbol{p})\delta(\boldsymbol{p}+\boldsymbol{p}'), \tag{2-3.16}$$

where the streamfunction power spectrum $\widehat{R}$ is the Fourier transform of R. Then since $\boldsymbol{u} = \nabla_h^\perp\psi$, the more familiar kinetic energy spectrum is then

$$\widehat{E}(\boldsymbol{k}) = |\boldsymbol{k}_h|^2\widehat{R}(\boldsymbol{k}).$$

We now take the average of (2-3.15). The slow time derivative term on the right-hand side disappears since $\mathsf{W}^{(1)} \propto \widehat{\psi}$, so that $\langle\mathsf{W}^{(1)}\rangle = 0$. Since $\langle\partial_\xi\mathsf{W}^{(2)}\rangle = 0$ by homogeneity in $\boldsymbol{\xi}$, we have $\langle\widetilde{\mathcal{Q}}_0\mathsf{W}^{(2)}\rangle = \mathcal{Q}_0\langle\mathsf{W}^{(2)}\rangle$, where the removal of the tilde corresponds to setting $\partial_{\boldsymbol{\xi}}$ to 0 in $\mathcal{Q}_0$. This leads to

$$-\mathcal{Q}_0\big\langle\mathsf{W}^{(2)}\big\rangle = \Big\langle\widetilde{\mathcal{P}}_0\mathsf{W}^{(1)} + (\mathcal{Q}_1+\partial_t)\mathsf{W}^{(0)}\Big\rangle, \tag{2-3.17}$$

an inhomogeneous version of (2-3.10).

The matrix $\mathcal{Q}_0$ has a non-trivial null space, spanned by the matrices $\boldsymbol{B}_j(\boldsymbol{k})$; the right-hand side of (2-3.17) must therefore satisfy a solvability condition of being orthogonal to the null-space of $\mathcal{Q}_0$. Since $\mathrm{i}\mathcal{Q}_0$ is self-adjoint with respect to the matrix inner product

$$\langle\!\langle\boldsymbol{X},\boldsymbol{Y}\rangle\!\rangle := \mathrm{tr}(\boldsymbol{M}\boldsymbol{X}^*\boldsymbol{M}\boldsymbol{Y}),$$

this condition is obtained by applying $\langle\!\langle\boldsymbol{B}_j(\boldsymbol{k}),\cdot\rangle\!\rangle$ to (2-3.17). We deal with the resulting terms one by one. First, by orthogonality and (2-3.11) we have

$$\langle\!\langle\boldsymbol{B}_i,\partial_t\mathsf{W}^{(0)}\rangle\!\rangle = \sum_{j=\pm}(\partial_t a_j)\langle\!\langle\boldsymbol{B}_i,\boldsymbol{B}_j\rangle\!\rangle = \partial_t a_i(\boldsymbol{x},\boldsymbol{k},t). \tag{2-3.18}$$

Next,

$$\begin{aligned}\langle\!\langle \boldsymbol{B}_i, \mathcal{Q}_1 W^{(0)} \rangle\!\rangle &= \sum_{j=\pm} \frac{1}{2\mathrm{i}} \langle\!\langle \boldsymbol{B}_i, (\nabla_{\boldsymbol{k}} \boldsymbol{L} \cdot \nabla_{\boldsymbol{x}} a_j) \boldsymbol{B}_j \rangle\!\rangle + \text{c.c.} \\ &= \sum_{j=\pm} \frac{1}{2\mathrm{i}} \langle\!\langle \boldsymbol{B}_i, \nabla_{\boldsymbol{k}} (\boldsymbol{L}\boldsymbol{B}_j) - \boldsymbol{L} \nabla_{\boldsymbol{k}} \boldsymbol{B}_j \rangle\!\rangle \cdot \nabla_{\boldsymbol{x}} a_j + \text{c.c.} \\ &= \sum_{j=\pm} \frac{1}{2\mathrm{i}} \langle\!\langle \boldsymbol{B}_i, \nabla_{\boldsymbol{k}} (\mathrm{i}\omega_j) \boldsymbol{B}_j + (\mathrm{i}\omega_j - \boldsymbol{L}) \nabla_{\boldsymbol{k}} \boldsymbol{B}_j \rangle\!\rangle \cdot \nabla_{\boldsymbol{x}} a_j + \text{c.c.} \\ &= \nabla_{\boldsymbol{k}} \omega_i \cdot \nabla_{\boldsymbol{x}} a_i(\boldsymbol{x}, \boldsymbol{k}, t). \end{aligned} \tag{2-3.19}$$

In order to evaluate the remaining term, we note that using (2-3.14) and (2-3.16), we have

$$\left\langle \widehat{N}_{\alpha\beta}(\boldsymbol{p}, \mathrm{i}\boldsymbol{q}) \widehat{N}_{\gamma\delta}(\boldsymbol{p}', \mathrm{i}\boldsymbol{q}') \right\rangle = \widehat{U}_{\alpha\beta}(\boldsymbol{p}, \mathrm{i}\boldsymbol{q}) \widehat{U}_{\gamma\delta}(\boldsymbol{p}', \mathrm{i}\boldsymbol{q}') \widehat{R}(\boldsymbol{p}) \delta(\boldsymbol{p} + \boldsymbol{p}'), \tag{2-3.20}$$

where Greek indices are used for matrix elements to make the following derivation clearer, and summation over repeated Greek indices is implied.

Expanding all terms, and making use of the delta function in (2-3.20), we have

$$
\begin{aligned}
&\langle\!\langle \boldsymbol{B}_i, \left\langle \widetilde{\mathcal{P}}_0 W^{(1)} \right\rangle \rangle\!\rangle \\
&= \iint \mathrm{e}^{\mathrm{i}(\boldsymbol{p}+\boldsymbol{p}')\cdot\boldsymbol{\xi}} M_{\nu\rho} b^i_\rho(\boldsymbol{k}) b^{i*}_\sigma(\boldsymbol{k}) M_{\sigma\lambda} \Big\langle \widehat{N}_{\lambda\mu}\big(\boldsymbol{p}, \mathrm{i}(\boldsymbol{k}+\tfrac{\boldsymbol{p}-\boldsymbol{p}'}{2})\big)\, \widehat{W}^{(1)}_{\mu\nu}(\boldsymbol{p}', \boldsymbol{k}+\tfrac{\boldsymbol{p}}{2}) \Big\rangle \mathrm{d}\boldsymbol{p}\mathrm{d}\boldsymbol{p}' + \text{c.c.} \\
&= \int \sum_{m,n=\pm} c^i_\lambda(\boldsymbol{k}) \widehat{U}_{\lambda\mu}(\boldsymbol{p}, \mathrm{i}(\boldsymbol{k}+\boldsymbol{p})) b^n_\mu(\boldsymbol{k}+\boldsymbol{p}) \overbrace{c^m_\rho(\boldsymbol{k}) b^i_\rho(\boldsymbol{k})}^{\delta^{im}} \widehat{R}(\boldsymbol{p}) \\
&\times \frac{a_m(\boldsymbol{k}) c^n_\alpha(\boldsymbol{k}+\boldsymbol{p}) \widehat{U}_{\alpha\beta}(-\boldsymbol{p}, \mathrm{i}\boldsymbol{k}) b^m_\beta(\boldsymbol{k}) + a_n(\boldsymbol{k}+\boldsymbol{p}) \Big(c^m_\alpha(\boldsymbol{k}) \widehat{U}_{\alpha\beta}(\boldsymbol{p}, \mathrm{i}(\boldsymbol{k}+\boldsymbol{p})) b^n_\beta(\boldsymbol{k}+\boldsymbol{p}) \Big)^*}{\mathrm{i}\big(\omega_m(\boldsymbol{k}) - \omega_n(\boldsymbol{k}+\boldsymbol{p})\big) - \theta} \mathrm{d}\boldsymbol{p} \\
&\quad + \text{c.c.} \\
&= -2\theta \mathrm{Re} \int \sum_{n=\pm} c^i_\lambda(\boldsymbol{k}) \widehat{U}_{\lambda\mu}(\boldsymbol{k}'-\boldsymbol{k}, \mathrm{i}\boldsymbol{k}') b^n_\mu(\boldsymbol{k}') \widehat{R}(\boldsymbol{k}'-\boldsymbol{k}) \\
&\quad \times \frac{a_i(\boldsymbol{k}) c^n_\alpha(\boldsymbol{k}') \widehat{U}_{\alpha\beta}(\boldsymbol{k}-\boldsymbol{k}', \mathrm{i}\boldsymbol{k}) b^i_\beta(\boldsymbol{k}) + a_n(\boldsymbol{k}') \Big(c^i_\alpha(\boldsymbol{k}) \widehat{U}_{\alpha\beta}(\boldsymbol{k}'-\boldsymbol{k}, \mathrm{i}\boldsymbol{k}') b^n_\beta(\boldsymbol{k}') \Big)^*}{\big(\omega_i(\boldsymbol{k}) - \omega_n(\boldsymbol{k}')\big)^2 + \theta^2} \mathrm{d}\boldsymbol{k}',
\end{aligned}
\tag{2-3.21}
$$

where we have let $\boldsymbol{k}' := \boldsymbol{k} + \boldsymbol{p}$. Setting the regularisation parameter $\theta \to 0$, we have that $\theta/(x^2+\theta^2) \to \pi\delta(x)$. This leads to a factor $\delta(\omega_i(\boldsymbol{k}) - \omega_n(\boldsymbol{k}'))$ which indicates that scattering is restricted within a single branch of the dispersion relation, and so we may drop the sum over n.

Scattering cross-section and kinetic equation

In order to evaluate (2-3.21), we define

$$
c_\lambda(\boldsymbol{k}) \widehat{U}_{\lambda\mu}(\boldsymbol{k}'-\boldsymbol{k}, \mathrm{i}\boldsymbol{k}') b_\mu(\boldsymbol{k}') := \alpha(\boldsymbol{k}, \boldsymbol{k}') + \mathrm{i}\beta(\boldsymbol{k}, \boldsymbol{k}'). \tag{2-3.22}
$$

For systems that conserve energy to leading-order, α and β have the symmetry properties

$$
\alpha(\boldsymbol{k}, \boldsymbol{k}') = -\alpha(\boldsymbol{k}', \boldsymbol{k}) \quad \text{and} \quad \beta(\boldsymbol{k}, \boldsymbol{k}') = \beta(\boldsymbol{k}', \boldsymbol{k}). \tag{2-3.23}
$$

We find in later chapters that these symmetries emerge naturally and are not imposed in the models that we consider, although it is not immediately clear what is responsible for the symmetries from the underlying model.

Assuming that (2-3.23) holds, it is straightforward to show that the terms in (2-3.21) simplify as

$$\mathrm{Re}\left(c_\lambda(\boldsymbol{k})\widehat{U}_{\lambda\mu}(\boldsymbol{k}'-\boldsymbol{k},\mathrm{i}\boldsymbol{k}')b_\mu(\boldsymbol{k}')\right)\left(c_\alpha(\boldsymbol{k}')\widehat{U}_{\alpha\beta}(\boldsymbol{k}-\boldsymbol{k}',\mathrm{i}\boldsymbol{k})b_\beta(\boldsymbol{k})\right) = -(\alpha^2(\boldsymbol{k},\boldsymbol{k}')+\beta^2(\boldsymbol{k},\boldsymbol{k}')),$$

and

$$\mathrm{Re}\left(c_\lambda(\boldsymbol{k})\widehat{U}_{\lambda\mu}(\boldsymbol{k}'-\boldsymbol{k},\mathrm{i}\boldsymbol{k}')b_\mu(\boldsymbol{k}')\right)\left(c_\alpha(\boldsymbol{k})\widehat{U}_{\alpha\beta}(\boldsymbol{k}'-\boldsymbol{k},\mathrm{i}\boldsymbol{k}')b_\beta(\boldsymbol{k}')\right)^* = \alpha^2(\boldsymbol{k},\boldsymbol{k}')+\beta^2(\boldsymbol{k},\boldsymbol{k}').$$

Then we can collect terms in (2-3.21) as

$$\begin{aligned}&\langle\!\langle \boldsymbol{B}_i, \left\langle \widetilde{\mathcal{P}}_0 W^{(1)}\right\rangle\rangle\!\rangle\\ &= 2\pi\int_{\mathbb{R}^d}\left(\alpha^2(\boldsymbol{k},\boldsymbol{k}')+\beta^2(\boldsymbol{k},\boldsymbol{k}')\right)\widehat{R}(\boldsymbol{k}'-\boldsymbol{k})\delta\big(\omega(\boldsymbol{k})-\omega(\boldsymbol{k}')\big)\big[a_i(\boldsymbol{k})-a_i(\boldsymbol{k}')\big]\mathrm{d}\boldsymbol{k}'.\end{aligned} \tag{2-3.24}$$

We may thus define a function

$$\sigma(\boldsymbol{k},\boldsymbol{k}') := 2\pi\big(\alpha^2(\boldsymbol{k},\boldsymbol{k}')+\beta^2(\boldsymbol{k},\boldsymbol{k}')\big)\widehat{R}(\boldsymbol{k}'-\boldsymbol{k})\delta\big(\omega(\boldsymbol{k})-\omega(\boldsymbol{k}')\big) \tag{2-3.25}$$

and collect the results (2-3.18), (2-3.19) and (2-3.24) such that each mode of the phase-space energy density $a_i(\boldsymbol{x},\boldsymbol{k},t)$, $i=\pm$, satisfies the kinetic equation

$$\partial_t a_i + \nabla_{\boldsymbol{k}}\omega_i\cdot\nabla_{\boldsymbol{x}}a_i = \int_{\mathbb{R}^d}\sigma(\boldsymbol{k},\boldsymbol{k}')a_i(\boldsymbol{k}')\mathrm{d}\boldsymbol{k}' - \Sigma(\boldsymbol{k})a_i(\boldsymbol{k}), \tag{2-3.26}$$

with

$$\Sigma(\boldsymbol{k}) = \int_{\mathbb{R}^d}\sigma(\boldsymbol{k},\boldsymbol{k}')\mathrm{d}\boldsymbol{k}'.$$

The function $\sigma(\boldsymbol{k},\boldsymbol{k}')$ is the main object of interest, known as the *differential scattering cross-section*, and $\Sigma(\boldsymbol{k})$ is known as the *total cross-section*. As discussed in §2-1, it encodes the effect of the background flow on the propagation of wave energy through

phase-space, quantifying the rate at which a wave with wavevector $\boldsymbol{k}'$ scatters to a wave with wavevector $\boldsymbol{k}$ at a position $\boldsymbol{x}$ in space. Explicit representations of the differential scattering cross-section in this thesis are given by (3-2.16) and (5-3.9). We recognise the right-hand side of (2-3.26) as the scattering integral (2-1.5) from §2-1.

We note that had the dispersion matrix depended on space as $\boldsymbol{L}(\boldsymbol{x}, \partial_{\boldsymbol{x}})$, then the dispersion relation would become $\omega(\boldsymbol{x}, \boldsymbol{k})$ and there would be an additional term on the left side of (2-3.26) of the form $-\nabla_{\boldsymbol{x}}\omega_i \cdot \nabla_{\boldsymbol{k}} a_i$.

Energy conservation

The conservation of the leading-order energy is established by noting that (2-2.5) expands to give

$$\begin{aligned}\mathcal{E}(\boldsymbol{x}, t) &= \frac{1}{2}\mathrm{tr}\int_{\mathbb{R}^d} \boldsymbol{M}\big[\boldsymbol{W}^{(0)} + \varepsilon^{1/2}\boldsymbol{W}^{(1)} + O(\varepsilon)\big]\mathrm{d}\boldsymbol{k} \\ &= \frac{1}{2}\int_{\mathbb{R}^d}\sum_{i=\pm} a_i(\boldsymbol{x}, \boldsymbol{k}, t)\mathrm{d}\boldsymbol{k} + O(\varepsilon^{1/2}) \\ &= \mathcal{E}_0(\boldsymbol{x}, t) + O(\varepsilon^{1/2}).\end{aligned}$$

Integrating (2-3.26) with respect to $\boldsymbol{k}$ and noting that the right-hand side vanishes because of the symmetry $\sigma(\boldsymbol{k}, \boldsymbol{k}') = \sigma(\boldsymbol{k}', \boldsymbol{k})$, which is observable from (2-3.23) and (2-3.25), we find the leading-order energy density conservation

$$\partial_t \mathcal{E}_0 + \nabla_{\boldsymbol{x}} \cdot \mathcal{F}_0 = 0, \tag{2-3.27}$$

with the leading-order energy flux

$$\mathcal{F}_0(\boldsymbol{x}, t) := \frac{1}{2}\int_{\mathbb{R}^d}\sum_{i=\pm}[\nabla_{\boldsymbol{k}}\omega_i(\boldsymbol{k})]a_i(\boldsymbol{x}, \boldsymbol{k}, t)\mathrm{d}\boldsymbol{k}.$$

Integrating (2-3.27) with respect to $\boldsymbol{x}$ gives conservation of the total energy $E = \iint \sum_i a_i(\boldsymbol{x}, \boldsymbol{k}, t)\mathrm{d}\boldsymbol{x}\mathrm{d}\boldsymbol{k}$ to leading-order. The wave action $\mathcal{A} = E/\omega$ is usually found to be the conserved quantity in wave–mean flow interacting systems (e.g. Salmon (1998); Olbers *et al.* (2012)), but here the energy is conserved as it differs from the action by only a small amount of order Ro due to the weak-flow assumption. We observe further that leading-order energy conservation in the scattering regime depends only the linear model conserving energy, that is to say the model (2-1.1) with

$\mathcal{N} = 0$. This is important as systems of the form (2-1.1) with a background flow do not generally conserve energy.

Kinetic equation derivation – concluding remarks

The primary focus of this section has been to derive the kinetic equation (2-3.26), taking the framework of Ryzhik *et al.* (1996) as a guide. A secondary outcome was to generalise and extend their framework a modest amount in order to handle some of the different ingredients in our underlying models for wave propagation. It is worth briefly summarising points of departure from and similarities with the Ryzhik *et al.* approach to give a better understanding of how the approaches compare.

The major differences stem from the different form of the starting point we take, in particular the model for the waves given by (2-3.1). Ryzhik *et al.* (1996) deals exclusively with first-order symmetric hyperbolic systems (see their eq. (4.1)) which can easily be shown to conserve a total energy. That specific class of system imposes some restrictions on the form of the operators and matrices appearing in the governing equations, and it also means that there are certain symmetries that can be exploited to simplify steps in the derivation.

The model (2-3.1) is not generally symmetric hyperbolic for the systems of waves linearised about a background flow we consider, though we have implicitly noted that a certain symmetry should be present for the linear part of the system. Equation 2-3.3 shows that the operator for the linear part of the system, $\boldsymbol{L}$, should have purely imaginary eigenvalues. This occurs when $\boldsymbol{L}$ is skew-symmetric with respect to the weighted inner product such that $\langle \boldsymbol{\phi}, \boldsymbol{L}\boldsymbol{\phi} \rangle_{\boldsymbol{M}} = -\langle \boldsymbol{L}\boldsymbol{\phi}, \boldsymbol{\phi} \rangle_{\boldsymbol{M}}$, and when this holds the linear system conserves energy. The approach of Ryzhik *et al.* is more restrictive by considering symmetric hyperbolic systems, as it implies a similar symmetry must also hold for the terms involving the background flow (see Ryzhik *et al.* (1996) eq. (4.2)) to ensure the total conservation of energy. An analagous condition for our model would be to consider systems with a skew-symmetric operator $\boldsymbol{N}$ such that $\langle \boldsymbol{\phi}, \boldsymbol{N}\boldsymbol{\phi} \rangle_{\boldsymbol{M}} = -\langle \boldsymbol{N}\boldsymbol{\phi}, \boldsymbol{\phi} \rangle_{\boldsymbol{M}}$, which is a property that doesn't hold for the models we have considered.

In Fourier space, this condition on the background flow terms translates to

$$\boldsymbol{M}(\boldsymbol{k})\widehat{\boldsymbol{N}}(\boldsymbol{p}, \mathrm{i}(\boldsymbol{k}+\boldsymbol{p})) = -\widehat{\boldsymbol{N}}^{*}(-\boldsymbol{p}, \mathrm{i}\boldsymbol{k})\boldsymbol{M}(\boldsymbol{k}+\boldsymbol{p}) \tag{2-3.28}$$

(c.f. Ryzhik *et al.* (1996) eq.(4.2)). Such a symmetry would help to simplify the derivation of the kinetic equation in two places. First, in (2-3.13) it would allow for the operator $\widehat{\boldsymbol{N}}$ to be factorised to obtain an expression for $\widehat{W}^{(1)}$. In this thesis we are saved by the special form that the operator $\widehat{\boldsymbol{N}}$ takes which is linearly dependent on the random streamfunction ψ, as shown in (2-3.14), such that we can factorise the linear dependence of $\widehat{W}^{(1)}$ on $\widehat{\psi}$. As a secondary consequence, this special form also means that we need only consider a scalar power spectrum $\widehat{R}$ for the random flow, whereas in general Ryzhik *et al.* show that it can be a tensor. It seems likely however that it is necessary to have the additional symmetries of the symmetric hyperbolic system in order to complete the derivation of the kinetic equation in the case of a tensor valued power spectrum. Second, the condition (2-3.28) would simplify the evaluation of (2-3.21) where, in lieu of additional symmetries, we introduced the decomposition (2-3.22) to help with the algebra. This decomposition gives a plain view of the $\boldsymbol{k}$–$\boldsymbol{k}'$ reversal symmetry of the cross-section, but it is unclear which ingredients in the underlying model would guarantee the symmetries (2-3.23). It seems likely that (2-3.23) holds whenever the underlying linear model conserves energy, as this $\boldsymbol{k}$–$\boldsymbol{k}'$ reversal symmetry leads to the leading order conservation of the Wigner function in the kinetic equation.

By considering the operators $\boldsymbol{L}$ and $\boldsymbol{N}$ as general pseudodifferential operators, we have shown how to work with a wider class of systems than the first-order PDE systems that Ryzhik *et al.* considers in deriving kinetic equations. This extension has already been considered, for example in Bal (2005) and Powell and Vanneste (2005).

Finally, the operator $\boldsymbol{N}$ further differed from Ryzhik *et al.* here as we included an additional dependence on a slow time scale to give $\boldsymbol{N}(\boldsymbol{x}, \partial_{\boldsymbol{x}}, \sqrt{\varepsilon}t)$. While this extension was the most straightforward to adopt and could be easily assimilated into the existing framework of Ryzhik *et al.*, it is perhaps the most significant update to the derivation from a physical point of view as it shows the energy transfers occur on constant-frequency resonant surfaces as long as the background flow varies slowly enough. However there are weak energy transfers that broaden the resonant surface due to this time dependence that are not captured by the kinetic equation, but would become significant over long timescales. It would be desirable to study these higher-order transfers as a further extension to the framework presented in this chapter.

Chapter 3

Scattering of internal tides

The derivation presented in the previous chapter is in general terms, highlighting that many features are shared between models that may differ in their specific form, but have the same basic scaling and mathematical structure in common, as discussed in §2-1.

In order to see how the kinetic equation description works in practice, and to train some intuition about its analysis, it is instructive to first apply the framework to a simple model. We take as a first case a background flow that is barotropic (i.e. z-independent)– a simplification that allows for the vertical dynamics to be separated to leave a two-dimensional shallow-water-like system that is simpler to analyse. Such a model finds a strong practical application in the problem of internal tide scattering, which we focus on for this chapter.

In later chapters we allow for full geostrophic turbulence with non-trivial vertical dynamics, where vertical shear by the background flow leads to IGWs scattering in three-dimensions.

The following is adapted from *Scattering of internal tides by barotropic quasigeostrophic flows*, published in the Journal of Fluid Mechanics (Savva and Vanneste, 2018).

3-1 Introduction

The propagation of IGWs in the ocean has received a great deal of attention, mainly motivated by the role they play in the large- and mesoscale circulation, through wave–mean-flow interaction, mixing and dissipation. The IGW spectrum is dominated by two types of waves: near-inertial oscillations, with frequencies close to the inertial frequency f, which are mainly generated by winds, and internal tides (ITs), primarily at the semi-diurnal lunar frequency, which are generated by the interaction of the barotropic tide with topography (e.g., Ferrari and Wunsch, 2009). Near-inertial oscillations have distinctive dynamics, including weak dispersion and weak vertical motion, that stem from their unique place at the low-frequency end of the IGW spectrum (Alford *et al.*, 2016); ITs, in contrast, are generic mid-frequency IGWs with their externally imposed frequency as their sole defining property.

The ocean's highly energetic quasigeostrophic turbulence has a strong impact on the structure of both inertial oscillations and ITs and hence, in the case of ITs, on their signature on the sea-surface height (Rainville and Pinkel, 2006; Ray and Zaron, 2016). There is by now an extensive literature devoted to this impact, with a recent impetus provided by upcoming high-resolution satellite-altimetry instruments and the need to disentangle ITs from mesoscale (balanced) motion in the observed sea-surface height. We refer the reader to the recent papers by Wagner *et al.* (2017) and Dunphy *et al.* (2017) for further background.

A key aspect of the interactions between quasigeostrophic turbulence and both near-inertial oscillations and low-mode ITs is that turbulence and waves share similar horizontal scales, of the order of 100 km. A consequence is that, in such a regime, the WKB approximation on which much of the understanding of IGW propagation is built is not valid. This has prompted the development of simplified, wave-averaged models that rely only on time-scale separation to represent the interactions between waves and flow in a simplified manner. Models of this kind include the Young–Ben Jelloul model of near-inertial oscillations in a quasigeostrophic flow (Young and Ben Jelloul, 1997) and its extensions accounting for the feedback of the waves on the flow (Xie and Vanneste, 2015; Wagner and Young, 2016; Thomas *et al.*, 2017). Wagner *et al.* (2017) recently derived an analogue of the Young–Ben Jelloul model equation for ITs. This model is formulated in physical space and retains a stiff term which enforces the

constraint that the ITs' fixed frequency imposes on their spatial structure and which cannot be eliminated without resorting to a Fourier-space formulation.

The present chapter focuses similarly on the impact of a quasigeostrophic flow on ITs, making no asymptotic assumption about the relative horizontal scales of ITs and flow. The focus here is on quantifying the scattering induced by a barotropic (i.e. z-independent) geostrophic turbulent flow which we model as a spatially homogeneous random field. We take advantage of the assumption of barotropic flow to use a vertical-mode expansion and thus reduce the problem to the study of an (equivalent) shallow-water model. Following the theory described in Chapter 2, we outline the derivation of a kinetic equation describing, in a statistically averaged sense, the energy exchanges between ITs with different wavevectors. The theory is formulated in terms of a wavevector-resolving energy density, $a(\boldsymbol{x}, \boldsymbol{k}, t)$, which makes it possible to capture spatial variations of the wave energy. The form of the scattering term in the kinetic equation for $a(\boldsymbol{x}, \boldsymbol{k}, t)$ shows that energy transfers are restricted to waves with the same frequency or, equivalently, the same wavenumber $|\boldsymbol{k}|$. These transfers result from interactions within resonant triads consisting of two ITs of equal frequencies with a zero-frequency flow (vortical) mode – the so-called catalytic interactions of Lelong and Riley (1991) and Bartello (1995). The rate of these transfers is proportional to the energy spectrum of the geostrophic flow. In the case of an isotropic flow, the scattering leads to the relaxation of the energy density towards a locally isotropic density $a(\boldsymbol{x}, |\boldsymbol{k}|)$. This theory complements that developed by Ward and Dewar (2010), shifting from a deterministic to a statistical treatment that can be regarded as a version of wave turbulence (Nazarenko, 2011) in which the statistics of the flow are prescribed. It generalises the theory developed by Danioux and Vanneste (2016) for near-inertial oscillations to IGWs of arbitrary frequencies. Note that this statistical approach focuses on a homogeneous field of scatterers (resulting from the turbulent flow) and that different analysis techniques apply to waves incident on isolated scatterers (e.g. Olbers, 1981).

We analyse the predictions of the kinetic equation, focusing attention on parameters representative of the first baroclinic mode of the semidiurnal lunar tide M_2. These predictions include a time scale for wave isotropisation applicable to statistically homogeneous wavefields (i.e. such that $\nabla_{\boldsymbol{x}} a = 0$) and in particular to the isotropisation of an initially plane wave examined numerically by Ward and Dewar (2010) in a shallow-water setup. The kinetic equation applies to more general, non-homogeneous

situations in which the energy density is modulated spatially ($\nabla_{\boldsymbol{x}} a \neq 0$). This makes it possible to study the scattering of ITs generated by a localised source such as a topographic ridge. Ponte and Klein (2015) and Dunphy *et al.* (2017) recently used three-dimensional Boussinesq simulations to study this problem and quantify the temporal incoherence of the ITs that results from the presence of a time-dependent turbulent flow. (See also Kelly *et al.* (2016) and Kelly and Lermusiaux (2016) for simulations of ITs in realistic configurations.) We carry out shallow-water simulations in a setup analogous to theirs, and compare the results with direct solutions of the kinetic equation. This provides an estimate for the length scale over which the wave field becomes isotropic and, more broadly, sheds light on the interplay between transport of the wave energy by the group velocity and scattering. We emphasise that this theory concentrates on the statistical properties of the IT energy and makes no predictions for their phase. In the regime we consider, with a flow assumed to vary on a timescale much larger than the tidal period, the stationarity of the turbulent energy spectrum ensures that the tidal energy remains concentrated at the single wavenumber dictated by the fixed tide frequency.

The plan of the chapter is as follows. We describe the equations satisfied by linear internal waves propagating on a barotropic quasigeostrophic flow in §3-2, expanding them in vertical modes to obtain an equivalent shallow-water system for each mode. We then sketch the derivation of the kinetic equation using the method of Ryzhik *et al.* (1996), relegating the technical computations to §2-3. We focus on the application of the kinetic equation to the case of an isotropic flow in §3-3 where we derive explicit estimates for the time- and lengthscales over which the IT field becomes isotropic. In §3-4 we compare theoretical predictions with direct simulations of the linearised shallow-water equations and with numerical solutions of the kinetic equation itself in a configuration where a wavemaker forces a plane IT in a turbulent flow. We conclude in §3-5 with a discussion.

3-2 Scattering theory for internal tides

3-2.1 Model

We model the propagation of ITs through a turbulent quasigeostrophic eddy field using the hydrostatic Boussinesq equations linearised about a slowly evolving

barotropic flow. The background flow is time dependent and geostrophically and hydrostatically balanced, given by $\boldsymbol{U} = (U, V, 0) = (-\partial_y\psi, \partial_x\psi, 0)$ in terms of a z-independent streamfunction ψ. With these assumptions, the linearised hydrostatic–Boussinesq equations read

$$\left.\begin{aligned} \partial_t \boldsymbol{u} + \boldsymbol{U}\cdot\nabla\boldsymbol{u} + \boldsymbol{u}\cdot\nabla\boldsymbol{U} + f\hat{\boldsymbol{z}}\times\boldsymbol{u} &= -\nabla p, \\ \partial_z p &= b, \\ \partial_t b + \boldsymbol{U}\cdot\nabla b + N^2 w &= 0, \\ \nabla\cdot\boldsymbol{u} + \partial_z w &= 0, \end{aligned}\right\} \tag{3-2.1}$$

where $(\boldsymbol{u}, w)$ denotes the IT velocity, $\hat{\boldsymbol{z}}$ is the vertical unit vector, p is the pressure normalised by a reference density, b the buoyancy, f the Coriolis parameter, and $N(z)$ the buoyancy frequency. We use the notation $\nabla = (\partial_x, \partial_y, 0)$ for the horizontal gradient throughout.

Assuming a flat bottom boundary and rigid lid, we project (3-2.1) onto baroclinic modes to obtain a set of rotating shallow-water equations governing their amplitudes:

$$\begin{aligned} \partial_t \boldsymbol{u}_m + \boldsymbol{u}_m\cdot\nabla\boldsymbol{U} + \boldsymbol{U}\cdot\nabla\boldsymbol{u}_m + f\hat{\boldsymbol{z}}\times\boldsymbol{u}_m &= -g\nabla\eta_m, \\ \partial_t\eta_m + \boldsymbol{U}\cdot\nabla\eta_m + h_m\nabla\cdot\boldsymbol{u}_m &= 0, \end{aligned} \tag{3-2.2}$$

where η_m is the equivalent surface height and h_m is the equivalent depth (see Appendix B for details). Note that this system differs from the one obtained by linearising the shallow-water equations about a background flow in geostrophic balance since the latter system includes a contribution from the (sloping) background free surface.

For physical applications in later sections, we take parameters corresponding to the first baroclinic mode only, since this contains the majority of the IT energy. In the ocean, energy is transferred between vertical modes as a result of vertical shear. However, as discussed by Dunphy and Lamb (2014) and Ponte and Klein (2015) the effect is small. Simulations in Dunphy *et al.* (2017) put the transfer of energy from the first mode to higher modes at 3% in their most extreme cases, with a highly energetic background flow, and less for typical ocean conditions. We drop the subscript m in (3-2.2) from this point on.

3-2.2 Derivation of the kinetic equation

We study IT scattering in the distinguished regime where the spatial scale of the flow, L_* say, is of the same order as the wavelength, that is, $|\boldsymbol{k}|L_* = O(1)$, where $\boldsymbol{k} = (k, l)$ is the IT horizontal wavevector. The assumption of a geostrophic flow requires a small Rossby number $\mathrm{Ro} = U_*/(fL_*) \ll 1$, where U_* is a typical flow velocity; in turn, this implies that the background flow velocities are small compared with the wave phase speed $\omega/|\boldsymbol{k}|$, where

$$\omega = \sqrt{f^2 + gh|\boldsymbol{k}|^2} \tag{3-2.3}$$

is the IT frequency, since $U_*/(\omega/|\boldsymbol{k}|) = O(U_*/(\omega L_*)) = O(\mathrm{Ro})$, given that $\omega = O(f)$ away from the equator. With the flow timescale T_* taken as the natural advective timescale L_*/U_*, this also implies that the flow evolves slowly compared with the IT timescale since $\omega T_* = O(\mathrm{Ro}) \ll 1$. We further assume that, while the IT phases vary over the lengthscale $|\boldsymbol{k}|^{-1}$, their amplitudes vary over a much larger scale $(\varepsilon|\boldsymbol{k}|)^{-1}$, where $\varepsilon \ll 1$. We adopt the scaling $\varepsilon = O(\mathrm{Ro}^2)$. As emerged in Chapter 2, this is the distinguished scaling that ensures that transport and scattering affect the wave field at the same order and are both captured at leading order by our asymptotic model.

Since our focus is on generic, statistical properties of the IT field, we model the turbulent background flow by a random streamfunction with homogeneous and stationary statistics. With our scaling assumptions, it is then possible to derive a single equation that describes the scattering and transport of IT energy following the theory of Ryzhik *et al.* (1996), as discussed in Chapter 2.

The equation derived by Ryzhik et al. (1996) governs the evolution of a scalar amplitude $a(\boldsymbol{x}, \boldsymbol{k}, t)$ which appears naturally in an eigenvector decomposition of the matrix $\mathsf{W}(\boldsymbol{x}, \boldsymbol{k}, t)$ (see Chapter 2 for details). Physically, this amplitude is interpreted as a wavevector-resolving energy density, related to the (leading-order) energy density of the system by

$$\mathcal{E}_0(\boldsymbol{x}, t) = \frac{1}{2}\int_{\mathbb{R}^2} a(\boldsymbol{x}, \boldsymbol{k}, t)\mathrm{d}\boldsymbol{k}. \tag{3-2.4}$$

To avoid any confusion, we emphasise that $a(\boldsymbol{x}, \boldsymbol{k}, t)$ itself represents a wave-energy density and not a wave amplitude; as its definition in (2-3.11) makes clear, it is a quadratic function of the wave fields, like the Wigner transform $\mathsf{W}(\boldsymbol{x}, \boldsymbol{k}, t)$ defined in (2-2.1).

In Chapter 2, we showed that $a(\boldsymbol{x}, \boldsymbol{k}, t)$ satisfies the kinetic equation

$$\partial_t a + \nabla_{\boldsymbol{k}}\omega \cdot \nabla_{\boldsymbol{x}} a = \mathcal{L}a - \Sigma a, \tag{3-2.5}$$

where the notation $\nabla_{\boldsymbol{x}} = \nabla = (\partial_x, \partial_y)$ emphasises that the spatial gradient applies to functions of both $\boldsymbol{x}$ and $\boldsymbol{k}$, and where $\nabla_{\boldsymbol{k}} = (\partial_k, \partial_l)$. Here ω is determined by the IT dispersion relation (3-2.3), so that $\nabla_{\boldsymbol{k}}\omega$ is the group velocity and the left-hand side of (3-2.5) represents the familiar wave transport. (The term $-\nabla_{\boldsymbol{x}}\omega \cdot \nabla_{\boldsymbol{k}} a$ would be added if ω depended explicitly on $\boldsymbol{x}$.) The right-hand side represents wave scattering by the background flow. The first term, given by

$$\mathcal{L}a(\boldsymbol{x}, \boldsymbol{k}, t) = \int_{\mathbb{R}^2} \sigma(\boldsymbol{k}, \boldsymbol{k}')a(\boldsymbol{x}, \boldsymbol{k}', t)\mathrm{d}\boldsymbol{k}', \tag{3-2.6}$$

quantifies the transfers of energy from all wavevectors $\boldsymbol{k}'$ into wavevector $\boldsymbol{k}$ that result from interactions with the background flow; the second term, where

$$\Sigma = \Sigma(\boldsymbol{k}) = \int_{\mathbb{R}^2} \sigma(\boldsymbol{k}, \boldsymbol{k}')\mathrm{d}\boldsymbol{k}', \tag{3-2.7}$$

is the total scattering cross section, quantifies the energy lost by wavevector $\boldsymbol{k}$ to all other wavevectors.

The function $\sigma(\boldsymbol{k}, \boldsymbol{k}')$ that appears in (3-2.6)–(3-2.7) is the main object of interest. It is known as the differential scattering cross section and measures the rate at which energy is scattered from $\boldsymbol{k}$ to $\boldsymbol{k}'$ at a position $\boldsymbol{x}$ in space.

General formulation

In order to apply the theory developed in Chapter 2 to derive the cross-section, we rewrite (3-2.2) in the abstract form (as in (2-3.1))

$$\partial_t \boldsymbol{\phi} + \left[\boldsymbol{L}(\partial_{\boldsymbol{x}}) + \sqrt{\varepsilon}\boldsymbol{N}(\boldsymbol{x}, \partial_{\boldsymbol{x}}, \sqrt{\varepsilon}t)\right]\boldsymbol{\phi} = 0, \tag{3-2.8}$$

where the vector

$$\boldsymbol{\phi}(\boldsymbol{x}, t) = (u,\ v,\ \eta)^{\mathrm{T}} \tag{3-2.9}$$

groups the dynamical variables and we have introduced the matrix operators

$$\boldsymbol{L}(\partial_x) = \begin{pmatrix} 0 & -f & g\partial_x \\ f & 0 & g\partial_y \\ h\partial_x & h\partial_y & 0 \end{pmatrix} \quad \text{and} \tag{3-2.10}$$

$$\boldsymbol{N}(\boldsymbol{x}, \partial_{\boldsymbol{x}}, \sqrt{\varepsilon}t) = \begin{pmatrix} \psi_x\partial_y - \psi_y\partial_x - \psi_{xy} & -\psi_{yy} & 0 \\ \psi_{xx} & \psi_x\partial_y - \psi_y\partial_x + \psi_{xy} & 0 \\ 0 & 0 & \psi_x\partial_y - \psi_y\partial_x \end{pmatrix}. \tag{3-2.11}$$

In (3-2.8), we have made the relative importance of the various terms explicit by scaling them with the relevant power of the small parameter ε. For convenience, we keep the equations in their dimensional form and treat ε as a bookkeeping parameter that can be set to 1 at the end of the calculation. Note that the dependence of $\boldsymbol{N}$ on $\sqrt{\varepsilon}t$ arises through the slow time dependence of ψ.

Basic ingredients for the kinetic equation

The depth-averaged energy density for the shallow-water system without background flow is given by

$$\mathcal{E}(\boldsymbol{x}, t) = \tfrac{1}{2}\left(h(u^2 + v^2) + g\eta^2\right) = \tfrac{1}{2}\langle \boldsymbol{\phi}, \boldsymbol{\phi} \rangle_{\boldsymbol{M}},$$

where we have defined the inner product

$$\langle \boldsymbol{f}, \boldsymbol{g} \rangle_{\boldsymbol{M}} := \boldsymbol{f}^* \boldsymbol{M} \boldsymbol{g}, \quad \text{with } \boldsymbol{M} := \begin{pmatrix} h & 0 & 0 \\ 0 & h & 0 \\ 0 & 0 & g \end{pmatrix}. \tag{3-2.12}$$

The matrix $\boldsymbol{L}$ in (3-2.10) is known as the dispersion matrix, since its eigenvalues give the dispersion relation. Taking the definition in (3-2.10) and replacing $\partial_{\boldsymbol{x}}$ by $\mathrm{i}\boldsymbol{k}$, we find that the solutions to the eigenvalue equation $\boldsymbol{L}(\mathrm{i}\boldsymbol{k})\boldsymbol{b}_j(\boldsymbol{k}) = \mathrm{i}\omega_j(\boldsymbol{k})\boldsymbol{b}_j(\boldsymbol{k})$ are given by

$$\omega_0 = 0, \quad \omega_\pm(\boldsymbol{k}) = \pm\sqrt{f^2 + gh|\boldsymbol{k}|^2} = \pm\,\omega(\boldsymbol{k}), \tag{3-2.13}$$

which is the usual dispersion relation for the rotating shallow-water model. The three

eigenvectors are given by

$$\boldsymbol{b}_0 = \frac{1}{g\omega^2}\begin{pmatrix} -\mathrm{i}gl \\ \mathrm{i}gk \\ f \end{pmatrix}, \quad \boldsymbol{b}_\pm = \frac{1}{\sqrt{2h}|\omega\boldsymbol{k}|}\begin{pmatrix} \pm\omega k + \mathrm{i}fl \\ \pm\omega l - \mathrm{i}fk \\ h|\boldsymbol{k}|^2 \end{pmatrix}. \tag{3-2.14}$$

These are orthonormal in the sense that

$$\langle \boldsymbol{b}_i, \boldsymbol{b}_j \rangle_{\boldsymbol{M}} = \delta_{ij}, \quad i,j = 0,\pm.$$

The zero eigenvalue ω_0 corresponds to the vortical mode of the system, which is accounted for by the prescribed quasigeostrophic background flow.

Finally, the derivation in Chapter 2 shows that in order to evaluate the cross-section we must transform the matrix (3-2.11). First we extract the linear dependence on the streamfunction by defining

$$\widehat{\boldsymbol{N}}(\boldsymbol{p}, \mathrm{i}\boldsymbol{q}, \sqrt{\varepsilon}t) = \widehat{\boldsymbol{U}}(\boldsymbol{p}, \mathrm{i}\boldsymbol{q})\widehat{\psi}(\boldsymbol{p}, \sqrt{\varepsilon}t),$$

as in (2-3.14). This leads to the matrix

$$\widehat{\boldsymbol{U}}(\boldsymbol{k}'-\boldsymbol{k}, \mathrm{i}\boldsymbol{k}') = \boldsymbol{k}'\times\boldsymbol{k}\, I_3 + \begin{pmatrix} (k'-k)(l'-l) & (l'-l)^2 & 0 \\ -(k'-k)^2 & -(k'-k)(l'-l) & 0 \\ 0 & 0 & 0 \end{pmatrix}, \tag{3-2.15}$$

where here $\boldsymbol{k}'\times\boldsymbol{k} = k'l - kl'$ and I_3 is the 3×3 identity matrix.

Evaluating the cross-section

In order to give an explicit representation of the cross-section for this system, we take the ingredients presented above and substitute them into (2-3.22) which defines

$$\langle \boldsymbol{b}_\pm(\boldsymbol{k}), \widehat{\boldsymbol{U}}(\boldsymbol{k}'-\boldsymbol{k}, \mathrm{i}\boldsymbol{k}')\boldsymbol{b}_\pm(\boldsymbol{k}')\rangle_{\boldsymbol{M}} =: \alpha(\boldsymbol{k},\boldsymbol{k}') \pm \mathrm{i}\beta(\boldsymbol{k},\boldsymbol{k}').$$

Substituting the eigenvectors (3-2.14) and elements of the matrix $\widehat{\boldsymbol{U}}$ from (3-2.15), we find that

$$\alpha(\boldsymbol{k},\boldsymbol{k}') = \frac{\boldsymbol{k}'\times\boldsymbol{k}}{\omega^2|\boldsymbol{k}||\boldsymbol{k}'|}\Big[(\omega^2+f^2)\boldsymbol{k}\cdot\boldsymbol{k}' - f^2|\boldsymbol{k}||\boldsymbol{k}'|\Big],$$

and

$$\beta(\boldsymbol{k},\boldsymbol{k}') = \frac{f\omega}{\omega^2|\boldsymbol{k}||\boldsymbol{k}'|}\Big[|\boldsymbol{k}\times\boldsymbol{k}'|^2 + \boldsymbol{k}\cdot\boldsymbol{k}'(|\boldsymbol{k}||\boldsymbol{k}'| - \boldsymbol{k}\cdot\boldsymbol{k}')\Big].$$

It is clear that these terms satisfy the symmetry properties $\alpha(\boldsymbol{k},\boldsymbol{k}') = -\alpha(\boldsymbol{k}',\boldsymbol{k})$ and $\beta(\boldsymbol{k},\boldsymbol{k}') = \beta(\boldsymbol{k}',\boldsymbol{k})$, so that we may write the cross-section according to (2-3.25) as

$$\sigma(\boldsymbol{k},\boldsymbol{k}') := 2\pi\big(\alpha^2(\boldsymbol{k},\boldsymbol{k}') + \beta^2(\boldsymbol{k},\boldsymbol{k}')\big)\frac{\widehat{E}(\boldsymbol{k}'-\boldsymbol{k})}{|\boldsymbol{k}'-\boldsymbol{k}|^2}\delta\big(\omega(\boldsymbol{k}) - \omega(\boldsymbol{k}')\big).$$

From the dispersion relation (3-2.3) we can re-express the delta function as

$$\delta(\omega(\boldsymbol{k}) - \omega(\boldsymbol{k}')) = \frac{\omega}{gh|\boldsymbol{k}|}\delta(|\boldsymbol{k}| - |\boldsymbol{k}'|),$$

and finally obtain the cross-section in the form

$$\begin{aligned}\sigma(\boldsymbol{k},\boldsymbol{k}') = \frac{2\pi}{gh\omega^3|\boldsymbol{k}|^5}\Big\{&|\boldsymbol{k}\times\boldsymbol{k}'|^2\big[(\omega^2+f^2)\boldsymbol{k}\cdot\boldsymbol{k}' - f^2|\boldsymbol{k}|^2\big]^2 \\ &+ f^2\omega^2\big[|\boldsymbol{k}\times\boldsymbol{k}'|^2 + \boldsymbol{k}\cdot\boldsymbol{k}'(|\boldsymbol{k}|^2 - \boldsymbol{k}\cdot\boldsymbol{k}')\big]^2\Big\}\frac{\widehat{E}(\boldsymbol{k}-\boldsymbol{k}')}{|\boldsymbol{k}-\boldsymbol{k}'|^2}\delta(|\boldsymbol{k}| - |\boldsymbol{k}'|),\end{aligned} \quad (3\text{-}2.16)$$

where $\widehat{E}$ is the energy spectrum of the flow. We note that $\sigma(\boldsymbol{k},\boldsymbol{k}')$ is real, positive, and symmetric with respect to the exchange between $\boldsymbol{k}$ and $\boldsymbol{k}'$. In Chapter 2, we also show that these properties ensure conservation of the leading-order energy density (3-2.4):

$$\partial_t\mathcal{E}_0 + \nabla_{\boldsymbol{x}}\cdot\mathcal{F}_0 = 0,$$

where

$$\mathcal{F}_0(\boldsymbol{x},t) = \int_{\mathbb{R}^2}\nabla_{\boldsymbol{k}}\omega(\boldsymbol{k})\,a(\boldsymbol{x},\boldsymbol{k},t)\mathrm{d}\boldsymbol{k}$$

is the leading-order energy flux (see (2-3.27)).

The presence of the factor $\delta(|\boldsymbol{k}| - |\boldsymbol{k}'|)$ in (3-2.16) implies that energy is only exchanged between wavevectors of the same magnitude, that is, between waves with the same frequency, as a result of the assumed slow time dependence of the background flow. Thus, in the regime considered, the IT energy is confined to the constant-frequency circle $|\boldsymbol{k}| = ((\omega^2-f^2)/(gh))^{1/2}$ in the wavevector plane. This can be related to the observation that the background flow only enters $\sigma(\boldsymbol{k},\boldsymbol{k}')$ through its energy spectrum $\widehat{E}$, which, for the statistically stationary flows considered, is time independent. The scattering described by (3-2.5) results from the resonant

interactions of two ITs, with wavevectors $\boldsymbol{k}$ and $\boldsymbol{k}'$ and identical frequencies, with a vortical flow mode of wavevector $\boldsymbol{k}-\boldsymbol{k}'$ and zero frequency. Because of potential-vorticity conservation, these interactions would leave the vortical mode unaffected even if it were allowed to evolve freely; hence they have been termed catalytic interactions (Lelong and Riley, 1991; Bartello, 1995; Ward and Dewar, 2010). We emphasise that (3-2.5) captures the net effect of multiple triadic interactions acting over long time scales. This is why the time scale of evolution is not linear in the flow amplitude but quadratic, dictated by the energy spectrum of the flow, in a manner familiar from wave turbulence (e.g. Nazarenko, 2011).

3-3 Scattering in isotropic turbulence

3-3.1 Isotropisation

In this section we use the kinetic equation (3-2.5) to make predictions about the scattering process and quantify the time and length scales over which ITs lose their spatial coherence. For simplicity, we assume that the flow is isotropic, $\widehat{E}(\boldsymbol{k})=\widehat{E}(|\boldsymbol{k}|)$. This motivates the use of polar coordinates for the wavevector, such that

$$\boldsymbol{k}=|\boldsymbol{k}|\begin{pmatrix}\cos\theta\\ \sin\theta\end{pmatrix}\quad\text{and}\quad\boldsymbol{k}'=|\boldsymbol{k}'|\begin{pmatrix}\cos(\theta+\theta')\\ \sin(\theta+\theta')\end{pmatrix},$$

where θ' is the angle between $\boldsymbol{k}$ and $\boldsymbol{k}'$. The change of coordinates reduces the scattering operator (3-2.6) to

$$\mathcal{L}a(\boldsymbol{x},|\boldsymbol{k}|,\theta,t)=\int_{-\pi}^{\pi}\sigma'(|\boldsymbol{k}|,\theta')a(\boldsymbol{x},|\boldsymbol{k}|,\theta-\theta',t)\mathrm{d}\theta', \tag{3-3.1}$$

where

$$\sigma'(|\boldsymbol{k}|,\theta'):=\int_0^{\infty}\sigma(\boldsymbol{k},\boldsymbol{k}')\,|\boldsymbol{k}'|\,\mathrm{d}|\boldsymbol{k}'|.$$

Note that we have used the evenness of σ' in θ' to rewrite (3-3.1) as a convolution. Note also that σ' is independent of the direction θ of $\boldsymbol{k}$ because the scattering process is rotationally invariant. The scattering cross section (3-2.16) can be written explicitly

as

$$\sigma'(|\boldsymbol{k}|,\theta)=\frac{\pi|\boldsymbol{k}|^2}{gh\omega^3}\Big\{(1+\cos\theta)\big[(\omega^2+f^2)\cos\theta-f^2\big]^2+\omega^2f^2[1-\cos(3\theta)]\Big\}\widehat{E}(2|\boldsymbol{k}\sin(\theta/2)|), \tag{3-3.2}$$

where we have removed the prime from θ' for convenience. Similarly, the total scattering cross section (3-2.7) reduces to

$$\Sigma(|\boldsymbol{k}|)=\int_{-\pi}^{\pi}\sigma'(|\boldsymbol{k}|,\theta)\mathrm{d}\theta. \tag{3-3.3}$$

In the limit $\omega\to f$ corresponding to near-inertial waves the cross section reduces to

$$\sigma'(|\boldsymbol{k}|,\theta)=\frac{2\pi f|\boldsymbol{k}|^2}{gh}\widehat{E}(2|\boldsymbol{k}\sin(\theta/2)|),$$

which recovers the result obtained by Danioux and Vanneste (2016) starting from the Young–Ben Jelloul model.

With the scattering cross section (3-3.2), the scattering operator (3-3.1) can be diagonalised using a Fourier series, or more precisely a cosine series since a is even in θ. Denoting the cosine transform by a hat, with

$$\widehat{a}_n(\boldsymbol{x},|\boldsymbol{k}|,t)=\frac{1}{2\pi}\int_{-\pi}^{\pi}\cos(n\theta)a(\boldsymbol{x},|\boldsymbol{k}|,\theta,t)\,\mathrm{d}\theta,$$

we find that

$$(\widehat{\mathcal{L}a})_n=\lambda_n\widehat{a}_n,\quad n=0,1,\cdots,$$

with the eigenvalues

$$\lambda_n=\lambda_n(|\boldsymbol{k}|):=2\pi\widehat{\sigma}'=\int_{-\pi}^{\pi}\sigma'(|\boldsymbol{k}|,\theta)\cos(n\theta)\mathrm{d}\theta. \tag{3-3.4}$$

Fourier transforming the kinetic equation (3-2.5) then gives

$$\partial_t\widehat{a}_n+(\widehat{\nabla_{\boldsymbol{k}}\omega\cdot\nabla_{\boldsymbol{x}}a})_n=(\lambda_n-\Sigma)\widehat{a}_n. \tag{3-3.5}$$

It follows from (3-3.4) and the non-negativity of σ' in (3-3.2) that

$$\lambda_0=\Sigma(|\boldsymbol{k}|)\quad\text{and}\quad|\lambda_{n\geq1}|<\lambda_0.$$

Thus the scattering term on the right-hand side of (3-3.5) vanishes for $n = 0$ and represents a damping for $n \geq 1$.

The implications are clearly seen for a wave field that is spatially homogeneous, that is, with $\nabla_{\boldsymbol{x}} a = 0$: the solution of (3-2.5), with initial condition

$$a(|\boldsymbol{k}|, \theta, t = 0) = A(|\boldsymbol{k}|, \theta),$$

is then simply

$$a(|\boldsymbol{k}|, \theta, t) = \sum_{n=0}^{\infty} \widehat{A}_n(|\boldsymbol{k}|)\, \mathrm{e}^{(\lambda_n - \Sigma)t} \cos(n\theta).$$

This describes the relaxation of the solution towards a stationary, isotropic (θ-independent) solution, since

$$\lim_{t\to\infty} a(|\boldsymbol{k}|, \theta, t) = \widehat{A}_0(|\boldsymbol{k}|) = \frac{1}{2\pi} \int_{-\pi}^{\pi} a(|\boldsymbol{k}|, \theta, t = 0)\mathrm{d}\theta.$$

This is a key feature of the scattering: the main impact of the random isotropic flow is to lead to the isotropisation of the IT field regardless of the initial condition. Note that, with $a(|\boldsymbol{k}|, \theta, t)$ the wave-energy density, $\widehat{A}_0$ represents the total, θ-integrated energy at wavevector $|\boldsymbol{k}|$, while the $\widehat{A}_n$ for $n \neq 0$ capture the energy's dependence on θ.

We can identify two timescales for the scattering process. First, the scattering time

$$T_{\text{scat}} = \Sigma^{-1} \tag{3-3.6}$$

estimates the time over which energy concentrated at $\boldsymbol{k}$ in spectral space is reduced by a factor of e^{-1} while converted to waves with other wavevectors. In other words, it is the timescale over which scattering effects become significant. Second, the timescale for convergence to an isotropic wavefield is given by

$$T_{\text{iso}} = (\Sigma - \lambda')^{-1}, \quad \text{where} \quad \lambda' := \max_{n\geq 1} \lambda_n. \tag{3-3.7}$$

This is the time for the last surviving anisotropic (i.e. $n \neq 0$) Fourier mode to decay by a factor of e^{-1}. Scattering lengthscales associated with the timescales (3-3.6) and

(3-3.7) can be defined as

$$L_{\mathrm{scat}} = c_g T_{\mathrm{scat}}, \quad L_{\mathrm{iso}} = c_g T_{\mathrm{iso}}, \tag{3-3.8}$$

where $c_g = |\nabla_{\boldsymbol{k}}\omega| = gh|\boldsymbol{k}|/\omega(|\boldsymbol{k}|)$ is the group speed.

3-3.2 Predicted behaviour

In this section, we use the time- and lengthscales (3-3.6)–(3-3.8) to examine how the scattering depends on the Coriolis parameter f, and on the strength and horizontal scales of the eddies as encoded in $\widehat{E}$. Since we focus on ITs, we regard the frequency ω as fixed and deduce $|\boldsymbol{k}|$ from the dispersion relation (3-2.3). We test some of our predictions against numerical simulations in §3-4.

We assume an isotropic energy spectrum of the form

$$\widehat{\mathcal{E}}(|\boldsymbol{k}|) := 2\pi\,|\boldsymbol{k}|\,\widehat{E}(|\boldsymbol{k}|) = \begin{cases} c_1|\boldsymbol{k}| & |\boldsymbol{k}| \le \kappa, \\ c_2|\boldsymbol{k}|^{-3.5} & |\boldsymbol{k}| \ge \kappa. \end{cases} \tag{3-3.9}$$

This depends on two parameters: κ, a peak wavenumber which sets the dominant lengthscale of the flow, and the root-mean-square velocity defined by $v_{\mathrm{rms}}^2 = \int_0^\infty \widehat{\mathcal{E}}\mathrm{d}|\boldsymbol{k}|$. The constants c_1 and c_2 are determined by κ and v_{rms} and the requirement of continuity at $|\boldsymbol{k}| = \kappa$. In practice, we choose κ so that the correlation length $l_c := \pi/k_c$, where $k_c := \iint |\boldsymbol{k}|\widehat{E}\mathrm{d}\boldsymbol{k}/\iint \widehat{E}\mathrm{d}\boldsymbol{k}$, is similar to the wavelength of the IT; calculation of the integrals using (3-3.9) gives $\kappa = 9\pi/(10\,l_c)$. Although quasi-geostrophic theory predicts a kinetic energy spectrum that decays as $|\boldsymbol{k}|^{-3}$ for balanced geostrophic turbulence, the slope is often observed to be slightly steeper, a result which is typically attributed to the presence of large-scale coherent structures that emerge in the turbulent flow (McWilliams *et al.*, 1994; Bartello, 1995; Kafiabad and Bartello, 2016). This motivates the form of (3-3.9) as representative of balanced geostrophic eddy fields in the ocean. Note that we have chosen an energy spectrum with non-zero energy for all $|\boldsymbol{k}|$. This matters because only the range $[0, 2|\boldsymbol{k}|]$ of the energy spectrum contributes to the scattering of ITs with wavenumber $|\boldsymbol{k}|$, as the factor $\widehat{E}(2|\boldsymbol{k}\sin(\theta'/2)|)$ in the scattering cross section (3-3.2) indicates. A lower cutoff of the spectrum, say at some wavenumber k_{cut}, would then imply that waves with $|\boldsymbol{k}| \le k_{\mathrm{cut}}/2$ are unaffected by scattering. This is related to the resonant triad view

that two ITs with the same wavenumber $|\boldsymbol{k}|$ and hence the same frequency can only form a resonant triad with a flow mode if this has a wavenumber in $[0, 2|\boldsymbol{k}|]$. We emphasise that while the form of (3-3.9) has been chosen to mimic a typical oceanic spectrum, the general theory developed in Chapter 2 does not require the spectrum to take any particular form or power law, other than the requirement of integrability to be physically meaningful. We demonstrate in Figures 3-1 and 3-2 that the scattering process itself, any thus any predictions made with the kinetic equation, depend strongly on the particular details of the energy spectrum $\widehat{\mathcal{E}}$ as it dictates the set of resonant triads that can be formed between the wave modes and the vortical mode.

Figure 3-1 shows the scattering cross section σ' in (3-3.2) as a function of θ and κ for $v_{\rm rms} = 0.25\,{\rm m\,s^{-1}}$ and for $f = 1.028 \times 10^{-4}\,{\rm s^{-1}}$ corresponding to 45° latitude. The equivalent depth is set to $h = 1.2$ m, as appropriate for the first baroclinic mode (Olbers *et al.*, 2012), and the frequency to $\omega = 2\pi/12.42$ hours, corresponding to the M_2 tide. The horizontal wavenumber is then $|\boldsymbol{k}| = 3 \times 10^{-5}\,{\rm m^{-1}}$ corresponding to a wavelength of about 200 km. The figure indicates that scattering is local in the angular coordinate, that is, ITs are preferentially scattered into waves with nearby directions. This is especially the case for small values of κ, corresponding to flows with typical scales much larger than the IT wavelength (left panel), when the values of σ' are also the largest. For larger values of κ, that is, for flows with smaller scales, the energy transfers are slower, but less localised in the angular direction (right panel).

The net effect of the scattering depends on both the value of σ' at fixed θ and the range of θ where σ' is substantial; it is best measured by the scattering and isotropisation time- and lengthscales introduced in (3-3.6)–(3-3.8). These scales are deduced from the cosine transform of σ' which give the eigenvalues of the scattering operator. The eigenvalues are shown in Figure 3-2a for $\kappa = 1.45 \times 10^{-5}\,{\rm m^{-1}}$, corresponding to a flow correlation length $l_c \approx 180$ km, with all other parameters as in Figure 3-1. The most important eigenvalues are the two largest, $n = 0$ and here $n = 1$, since they control the scattering and isotropisation time- and lengthscales. These scales are displayed as functions of κ in Figure 3-2b. The figure shows that large-scale flows lead to rapid scattering but slow isotropisation. This can be easily understood: large-scale flows cause rapid energy transfers but, because of the localised nature of the scattering, these transfers are limited to waves of similar directions and a long time is needed for energy to be distributed near-uniformly in the angular direction. (The large-scale-flow regime can be tackled using ray tracing as has frequently been applied

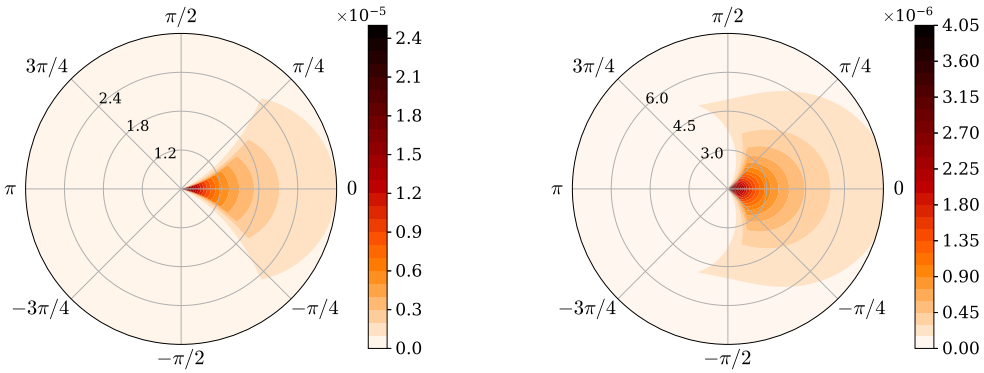

Figure 3-1. Scattering cross section σ' in (3-3.2) for the energy spectrum (3-3.9) as a function of the peak wavenumber κ and angle θ treated as polar coordinates. The IT wavenumber is fixed as $|\boldsymbol{k}| = 3 \times 10^{-5}\,\mathrm{m}^{-1}$ corresponding to the mode-1 M_2 tide at $45°$ latitude, and the flow's root-mean-square velocity as $v_{\mathrm{rms}} = 0.25\,\mathrm{m\,s}^{-1}$. The left panel shows the range $0.2|\boldsymbol{k}| \leq \kappa \leq |\boldsymbol{k}|$, the right panel the range $0.5|\boldsymbol{k}| \leq \kappa \leq 2.5|\boldsymbol{k}|$. Three (circular) contours of κ are labelled in each panel in units of 10^{-5} m^{-1}.This figure depicts how the scattering process behaves for waves in relatively large-scale flows (left), or flows comprised of lengthscales similar to the IT scale (right). (Note that the points closest to the origin correspond to the largest-scale flows.) The larger-scale flows lead to a concentration of σ' in a narrow region close to $\theta = 0$ such that the scattering is localised in wavenumber space, and wave energy redistributes slowly and diffusively. When the flow scales are comparable to the IT scale, waves are able to scatter nonlocally in wavenumber space such that their angular direction can deflect by $\pi/2$ or more, leading to a more rapid isotropisation of the IT wavefield. Note that the waves do not change lengthscale, $|\boldsymbol{k}'| = |\boldsymbol{k}|$ in this model so that the IT lengthscale remains fixed after scattering.

for deterministic flows (e.g. Rainville and Pinkel, 2006; Chavanne *et al.*, 2010). For weak random flows as assumed here, the ray equations can be analysed asymptotically using methods developed for noisy Hamiltonian systems (e.g. Bal *et al.*, 2010) to show that the IT wavevector diffuses along the constant frequency circle $|\boldsymbol{k}| = \text{const}$, consistent with the kinetic-equation description; see Müller (1976, 1977) for early treatments in this spirit.) Isotropisation is most effective when κ has an order of magnitude similar to $|\boldsymbol{k}|$: for the chosen energy spectrum, isotropisation is fastest for $\kappa \approx 6 \times 10^{-5}\,\mathrm{m}^{-1}$ corresponding to a flow correlation length of about $50\,\mathrm{km}$. Isotropisation slows down for larger values of κ simply because the total flow energy in the useful range $[0, 2|\boldsymbol{k}|]$ decreases with κ.

Figure 3-2c shows the scattering and isotropisation times and lengths as functions of v_{rms} and for $\kappa = 1.45 \times 10^{-5}\,\mathrm{m}^{-1}$. The dependence is simply in v_{rms}^{-2}. The figure suggests that full isotropisation of ITs generated at localised topographical features is rare in the ocean since the lengthscales required exceed the basin scales even for strong flows. On the other hand, scattering is effective over much shorter spatial scales, of the order of a few hundreds of kilometers, and over time scales of a week or so, comparable to other dynamical time scales in the ocean. The conclusion, then, is that typical ITs are strongly influenced by the quasigeostrophic flow, though not to the extent that they become completely isotropic. As highlighted by Ward and Dewar (2010), the timescale of a week or so is shorter than the characteristic timescales of nonlinear wave–wave interactions except, perhaps, for the special case of parametric subharmonic instability at the critical latitude of 29° (MacKinnon and Winters, 2005). It is likely, then, that scattering by the geostrophic flow plays a more important role than wave–wave interactions in determining the characteristics of oceanic IGWs. We should note, however, that the most energetic regions of the ocean, such as western boundary currents, where scattering is most effective, are also strongly inhomogeneous so that our theory does not apply in a strict sense.

Figure 3-2d explores the dependence of scattering on latitude. Latitude affects the cross section σ' through f and also through $|\boldsymbol{k}|$ if we consider a fixed frequency as is done here. In the ocean, different latitudes may also lead to different energy spectra. For simplicity, in plotting Figure 3-2d we have taken the same spectrum for each latitude, keeping κ fixed. The figure shows that the scattering time increases with latitude. The isotropisation time, however, decreases with latitude with, as far as we can tell, no obvious interpretation; the scattering is determined as the

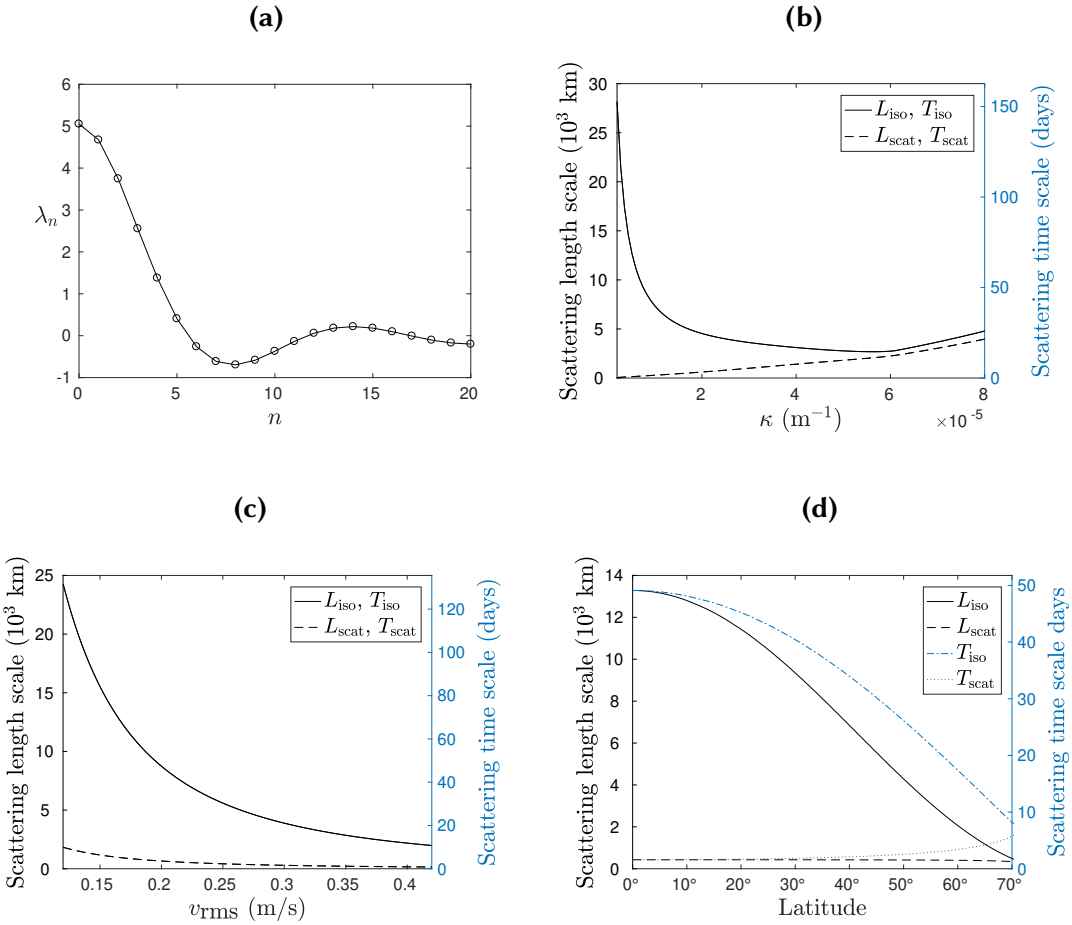

Figure 3-2. (a) Eigenvalues λ_n of the scattering operator, given by (3-3.4), for the energy spectrum in (3-3.9) with $\kappa = 1.45 \times 10^{-5}\,\mathrm{m}^{-1}$ and $v_{\rm rms} = 0.25\,\mathrm{m\,s}^{-1}$, and for an IT with $|\boldsymbol{k}| = 3 \times 10^{-5}\,\mathrm{m}^{-1}$ and $f = 1.028 \times 10^{-4}\,\mathrm{s}^{-1}$. (b) Scattering and isotropisation length and time scales $L_{\rm scat}$, $L_{\rm iso}$, $T_{\rm scat}$ and $T_{\rm iso}$ as functions of the peak wavenumber κ, with all the other parameters as in (a). (c) As in (b) but as functions of $v_{\rm rms}$ and for $\kappa = 1.45 \times 10^{-5}\,\mathrm{m}^{-1}$. (d) As in (b) but as functions of latitude. This figure demonstrates some of the information about the scattering process accessible from the knowledge of the cross-section, and in particular about how the typical scales of spatial coherence for the internal tide vary according to physical parameters.

difference between two eigenvalues and is hence difficult to intuit. The scattering and isotropisation lengths both decrease with latitude, partly as a result of a decrease of the group velocity. We note that Ward and Dewar (2010) conclude from simulations that scattering and isotropisation weaken with latitude, leading to longer propagation distances (see their Figure 11). This apparent contradiction is likely resolved by the fact that their non-dimensional formulation implies that their energy spectrum also changes with latitude, keeping the energy in the range $[0, 2|\boldsymbol{k}|]$ constant as f changes. A general conclusion we can draw from the form of σ' and our parameter-dependence study is the fact that the quasigeostrophic energy spectrum is the key factor determining the strength of the scattering.

3-4 Simulations

In this section we analyse numerical simulations of the linearised equivalent shallow-water system (3-2.2) and compare them with the theoretical predictions of the previous section and with direct simulations of the kinetic equation (3-2.5).

3-4.1 Shallow-water simulations

We solve (3-2.2) numerically, adding a harmonic forcing term to generate a coherent plane wave. The numerical scheme relies on pseudospectral and splitting methods: the terms independent of the background flow are integrated exactly in Fourier space, while the terms that depend on the background flow are integrated using an Euler scheme in physical space. In particular this is achieved by writing the solution to the shallow-water system (3-2.8) by integrating to obtain

$$\boldsymbol{\phi}(\boldsymbol{x}, t) = \mathrm{e}^{-\boldsymbol{L}t}\big[\boldsymbol{\phi}_0(\boldsymbol{x}) - \sqrt{\varepsilon}\int_0^t \mathrm{e}^{\boldsymbol{L}s}\boldsymbol{N}(\boldsymbol{x}, \partial_{\boldsymbol{x}})\boldsymbol{\phi}(\boldsymbol{x}, s)\mathrm{d}s\big], \tag{3-4.1}$$

where $\boldsymbol{\phi}_0(\boldsymbol{x}) = \boldsymbol{\phi}(\boldsymbol{x}, t = 0)$. The linear part of (3-2.8) is solved exactly in terms of the matrix exponential, $\exp(-\boldsymbol{L}(\partial_{\boldsymbol{x}})t)$, while the terms involving the flow appear in the integral term of (3-4.1). We simplify the integrand by assuming that the evolution of the dynamics is dominated by the linear contribution over one timestep such that $\boldsymbol{\phi}(\boldsymbol{x}, \Delta s) \approx \exp(-\boldsymbol{L}\Delta s)\boldsymbol{\phi}_0(\boldsymbol{x})$, and by Taylor expanding the exponentials. We

therefore approximate the solution (3-4.1) over a timestep as

$$\boldsymbol{\phi}^{j+1}(\boldsymbol{x}) = \mathcal{F}^{-1}_{\boldsymbol{k}\to\boldsymbol{x}}\Big\{\mathrm{e}^{-\boldsymbol{L}(\mathrm{i}\boldsymbol{k})\Delta t}\mathcal{F}_{\boldsymbol{x}\to\boldsymbol{k}}\big\{\big[1-\sqrt{\varepsilon}\Delta t\boldsymbol{N}(\boldsymbol{x},\partial_{\boldsymbol{x}})\big]\boldsymbol{\phi}^{j}(\boldsymbol{x})\big\}\Big\} + O(\varepsilon\Delta t^2),$$

where $\boldsymbol{\phi}^j(\boldsymbol{x}) = \boldsymbol{\phi}(\boldsymbol{x}, t_j)$ is the solution at the j-th timestep, and $\mathcal{F}\{\cdot\}$ ($\mathcal{F}^{-1}\{\cdot\}$) denotes the FFT (inverse FFT).

The domain is a 7168 km $\times$ 1024 km channel on an f-plane centred at $45°$N. We use a spatial resolution of 1792×256, with that $\Delta x = \Delta y = 4$ km, with periodic boundary conditions in the y-direction, and absorbing layers 30-gridpoints wide at each end of the domain in the x-direction, and take timesteps of $\Delta t = 4000$ s. The absorbing layers are imposed as the "pretty good sponge" described by Modave *et al.* (2010). We run an ensemble of 100 simulations with random realisations of the background flow in order to study statistics. Each simulation corresponds to 80 days, which is long enough to study isotropisation in a moderately energetic flow. A wavemaker forces an IT through a term of the form

$$F = A\sin(\Omega t)\,\mathrm{e}^{-(x-x_0)^2/\Delta^2},$$

added to the continuity equation (cf. Ponte and Klein, 2015). Here, $x_0 = 400$ km is the position of the wavemaker in the x-direction and $\Delta = 10$ km its width; Ω is the tidal frequency. The amplitude A is arbitrary since we solve a linear system. The forcing is ramped up slowly to reach its maximum amplitude over approximately 1 week. The resulting plane waves that are generated have a wavelength of approximately 150 km, as expected for a first baroclinic mode wave at $45°$ latitude.

For the background flow we take a homogeneous isotropic Gaussian random field, tapered in the region $0 < x < 1000$ km so as not to interfere with the wavemaker. This field is generated numerically as a Fourier series with random coefficients. The energy spectrum is that in (3-3.9), with $v_{\mathrm{rms}} = 0.25\,\mathrm{ms}^{-1}$ and $\kappa = 1.45\times10^{-5}\,\mathrm{m}^{-1}$ leading to flows with a correlation length of about 200 km. The other parameters are those of the mode-1 M_2 tide at $45°$, as in §3-3.2. The results presented below use a time-independent flow. We carried out additional simulations with slowly time-varying flows to confirm the theoretical prediction of Chapter 2 that IT scattering is essentially unaffected by the time dependence of stationary random flows with timescales $O(\mathrm{Ro}^{-1})$ longer than the IT period. Note that the modelling of the background flow by a Gaussian random field is a choice motivated by practicality

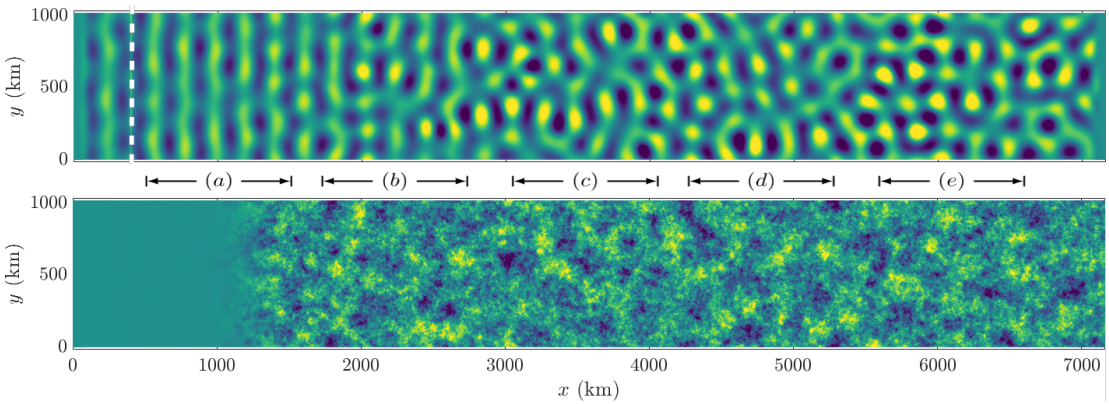

Figure 3-3. Top: sea-surface elevation η in an equivalent shallow-water simulation of the mode-1 M_2 tide in a turbulent flow with $v_{\text{rms}} = 0.25\,\text{m}\,\text{s}^{-1}$ at $45°$ latitude. Bottom: vorticity field of the turbulent flow. Plane waves generated at $x = 400$ km (indicated by the dashed line in the top panel) propagate and interact with the turbulent flow, leading to a scattered wavefield with an increasingly scrambled appearance as distance increases from the wavemaker.

and the fact that, according to our theory, the only statistical property of the flow that influences the scattering is its energy spectrum. An alternative would be to carry out a large number of quasigeostrophic simulations to generate an ensemble of flows with more realistic statistics. This would however be computationally expensive; it would also require great care to control the flow parameters and to ensure stationary statistics.

The top panel of Figure 3-3 shows one realisation of the IT height field η at $t = 80$ days, when plane waves generated by the wavemaker (indicated by a dashed line) have propagated across the eddy field shown in the bottom panel. Close to the wavemaker the wave field has a plane-wave structure which becomes scrambled in appearance as the phases randomise due to flow scattering. In agreement with our scattering theory, the wave field retains a single lengthscale – the wavelength set by the tidal frequency – throughout its evolution: scattering does not lead to a scale cascade. This is consistent with the earlier simulation results of Ward and Dewar (2010), Wagner *et al.* (2017), Ponte and Klein (2015) and Dunphy *et al.* (2017), the latter two in a three-dimensional setup. Note that, since we solve the linearised system, there is no harmonic generation and consequent formation of smaller wave scales as described by Ward and Dewar (2010). The eigenvalues λ_n for the IT and flow parameters chosen are those shown

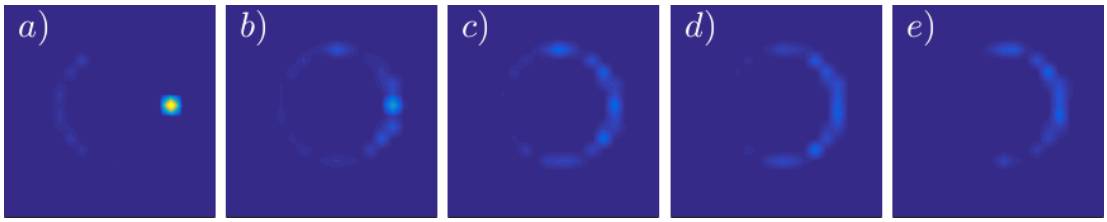

Figure 3-4. Energy density in the $\boldsymbol{k}$ plane of a single mode in different regions along the channel, from an ensemble of 100 shallow-water simulations. The regions are five 1024 km $\times$ 1024 km boxes centred about the midpoints $x = \{1000, 2250, 3500, 4750, 6000\}$ km. Note that full isotropy isn't achieved since the absorbing layers at the ends of the channel prevent wave energy scattered further downstream from returning. The absence of left-propagating energy near the end of the channel is responsible for the semi-annular appearance of the distributions in boxes (d)–(e).

in Figure 3-2(a) and correspond to $L_{\text{scat}} = 420\,\text{km}$ and $L_{\text{iso}} = 5,600\,\text{km}$. This is qualitatively consistent with the wave field in Figure 3-3.

Projection of simulation data onto modes

To assess our theoretical results in more detail, we need to estimate the energy density $a(\boldsymbol{x}, \boldsymbol{k}, t)$ from the simulations. To this end, we take Fourier transforms of the wave fields in five 1024 km $\times$ 1024 km square boxes spanning the length of the domain. For each realisation of the flow, we compute the Fourier transform of u, v and η in each box at the end of the simulation, project onto the IT eigenmode then average over the ensemble to obtain an approximation $\tilde{a}(\boldsymbol{k}, t)$, say, of $a(\boldsymbol{x}, \boldsymbol{k}, t)$ in the box.

Using the Fourier representation of the Wigner function given in (2-2.6) (with $\varepsilon = 1$), it is easily verified that the projection property

$$\int_{\mathbb{R}^2} W(\boldsymbol{x}, -\boldsymbol{k}, t)\mathrm{d}\boldsymbol{x} = |\widehat{\boldsymbol{\phi}}(\boldsymbol{k})|^2$$

holds. In order to discriminate between the energy contributions from the different modes, we expand the fields in the eigenvectors basis according to

$$\widehat{\boldsymbol{\phi}}(\boldsymbol{k}, t) = \sum_{j=\pm} A^{(j)}(\boldsymbol{k}, t)\boldsymbol{b}_j(\boldsymbol{k}),$$

so that the energy for each wavenumber is given by

$$\tilde{\mathcal{E}}(\boldsymbol{k},t)=\frac{1}{2}\langle\widehat{\boldsymbol{\phi}},\widehat{\boldsymbol{\phi}}\rangle_{\boldsymbol{M}}=\frac{1}{2}(|A^{(+)}(\boldsymbol{k},t)|^2+|A^{(-)}(\boldsymbol{k},t)|^2),$$

with $\langle\,\cdot\,,\,\cdot\,\rangle_{\boldsymbol{M}}$ as defined in (3-2.12). Orthonomality of the eigenvectors means that we can extract the modal energy contributions by projection to find

$$|A^{(j)}(\boldsymbol{k},t)|^2=|\langle\boldsymbol{b}_j(\boldsymbol{k}),\widehat{\boldsymbol{\phi}}(\boldsymbol{k},t)\rangle_{\boldsymbol{M}}|^2.$$

In terms of the energy density, the leading-order energy is given by

$$\tilde{\mathcal{E}}_0(\boldsymbol{k},t)=\frac{1}{2}\int_{\mathbb{R}^2}\sum_{j=\pm}a_j(\boldsymbol{x},-\boldsymbol{k},t)\mathrm{d}\boldsymbol{x}.$$

Thus, we may track the energy from the '+' mode by projecting the Fourier transform of the wave fields:

$$\int_{\mathbb{R}^2}a_+(\boldsymbol{x},-\boldsymbol{k},t)\mathrm{d}\boldsymbol{x}=\left\langle|\langle\boldsymbol{b}_+(\boldsymbol{k}),\widehat{\boldsymbol{\phi}}(\boldsymbol{k},t)\rangle_{\boldsymbol{M}}|^2\right\rangle=\left\langle|\omega\widehat{\eta}/|\boldsymbol{k}||^2\right\rangle,$$

with $\langle\cdot\rangle$ denoting the ensemble average. This relates to the leading-order energy density of a single wave mode to the sea-surface height.

The results are shown in Figure 3-4. For the first box, located immediately to the right of the wavemaker, most of the energy is concentrated at the single point $\boldsymbol{k}=(k_0,0)$, where $k_0=\sqrt{(\omega^2-f^2)/gh}$, indicating a pure plane wave propagating to the right. (There is also a faint signal of left-propagating waves resulting from scattering at larger x.) In the next boxes, energy spreads around the circle of constant radius $|\boldsymbol{k}|=k_0$. The spectrum is in fact distributed over a finite-width annulus rather than a circle, as a result of off-resonant interactions between waves and flow.

We obtain a clearer view of the distribution of energy as a function of θ by integrating $a(\boldsymbol{x},\boldsymbol{k},t)$ in the 90 angular sectors $2(n-1)\pi/90\le\theta\le 2n\pi/90$, $n=1,\cdots,90$. The results are shown in Figure 3-5a. They enable a better assessment of the validity of the lengthscale estimates $L_{\mathrm{scat}}=420\,\mathrm{km}$ and $L_{\mathrm{iso}}=5600\,\mathrm{km}$. Note that these lengths should be measured from the point where the background flow starts, which is at approximately $x=1000$ km, so that we would expect to see the fields isotropise at $x>6000$ km along the channel, corresponding to the rightmost box of Figure 3-4. We see however that the field is not fully isotropic in that region. An

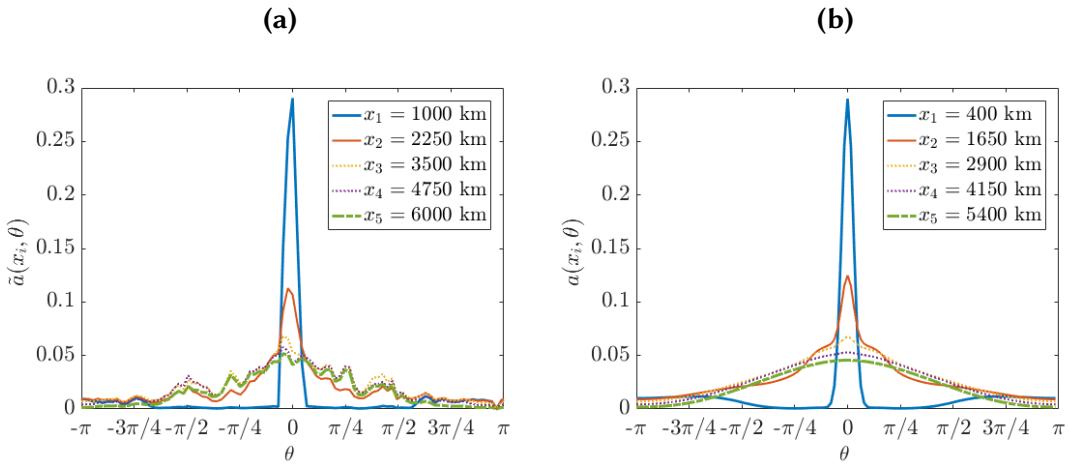

Figure 3-5. (a) Energy density as a function of θ estimated from the ensemble of shallow-water simulations as $\tilde{a}(x_i, \theta)$, with the x_i taken as the box midpoints, and (b) the energy density $a(x_i, \theta)$ as simulated from kinetic equation (3-4.2). The parameters are those of Figure 3-3 and the time corresponds to the end of the simulation. The agreement between the two distributions instils confidence in the validity and usefulness of the kinetic equation.

explanation is that the numerical simulation includes an absorbing layer near the right boundary of the domain, which allows energy to exit the channel but not to re-enter it. As a result, there are no left-propagating waves at the end of the channel. In addition, we emphasise that L_{iso} is only an order-of-magnitude estimate which, by converting timescale into lengthscale using the group speed, ignores the directional properties of the transport of wave energy with the group velocity. We next go beyond this order-of-magnitude estimate and make direct predictions for the scattering by solving the kinetic equation numerically.

3-4.2 Kinetic equation simulations

We simulate the kinetic equation (3-2.5) under the assumption of homogeneity in the y-direction, consistent with the periodic boundary conditions, and using the angle θ, with $\boldsymbol{k} = k_0(\cos\theta, \sin\theta)$, as an independent variable. This reduces the number of independent variables to 3, with $a(x, \theta, t)$, so that the kinetic equation becomes

$$\partial_t a + c_g \cos\theta \, \partial_x a = (\mathcal{L} - \Sigma)a + F(x, \theta), \tag{3-4.2}$$

where $\mathcal{L}$ and Σ are given by (3-3.1) and (3-3.3), and $F(x,\theta)$ is a forcing term mimicking the wavemaker of the shallow-water simulations. We take F to be a Gaussian centred about $x = 400$ km, $\theta = 0$, with width parameters $\Delta_x = 40$ km and $\Delta_\theta = 0.1$, and an amplitude that is scaled to match the initial energy peak from the shallow-water simulation data.

We simulate (3-4.2) using a pseudospectral splitting method, breaking the equation into subproblems. First the advection term is integrated using a semi-Lagrangian explicit finite-difference scheme. Then, the scattering terms on the right-hand side are integrated exactly in Fourier space. We use a Fourier transform, as in (3-3.5), to write the solution to the scattering subproblem $\partial_t a = (\mathcal{L} - \Sigma)a$ in the form

$$a(x,\theta,t_{j+1}) = \mathcal{F}^{-1}_{n\to\theta}\{\mathrm{e}^{(\lambda_n-\Sigma)\Delta t}\widehat{a}_n(x,t_j)\},$$

where FFTs are used to obtain λ_n and $\widehat{a}_n$ numerically, and $\mathcal{F}^{-1}\{\cdot\}$ is an inverse FFT. Finally the forcing term $F(x,\theta)$ and the damping, due to absorbing layers, are imposed in the physical (x,θ) space. The domain is 7168 km $\times$ 2π, with a resolution of 1792 $\times$ 256, and time step $\Delta t = 900$ s up to a final time of 80 days. We apply periodic boundary conditions in the θ-direction, and place absorbing layers 30-gridpoints wide at each end of the domain in the x-direction, as in the shallow-water simulation. The evolution of $a(x,\theta,t)$ is illustrated in Figure 3-6. The wave energy, initially concentrated at $(x,\theta) = (400,0)$, gets advected by the group velocity in the x-direction and spreads in the angular direction. Once energy reaches $|\theta| > \pi/2$, it propagates to the left, leading to the weak signal for $k < 0$ observed in the first panel of Figure 3-4.

At the end of the simulation, we evaluate $a(x,\theta,t)$ at different points along the channel to get a set of curves $a(x_i,\theta,t = 80\,\mathrm{days})$, $1 \le i \le 5$. The points x_i are taken to be spaced along the channel in the same way as the windows shown in Figure 3-4. Note that we have to take into account the fact that there is no flow in the shallow-water simulations from the point of generation at $x = 400$ km to approximately $x = 1000$ km (see Figure 3-3), whereas the kinetic equation assumes a flow is present throughout the domain. To resolve the discrepancy, the values of x_i are taken 600 km less than the midpoints of the boxes used for the shallow-water simulations. The functions $a(x_i,\theta)$ are shown next to the equivalent shallow-water estimates in Figure 3-5. There is a remarkably good agreement between the solution of the kinetic equation and the shallow-water simulation results. This demonstrates

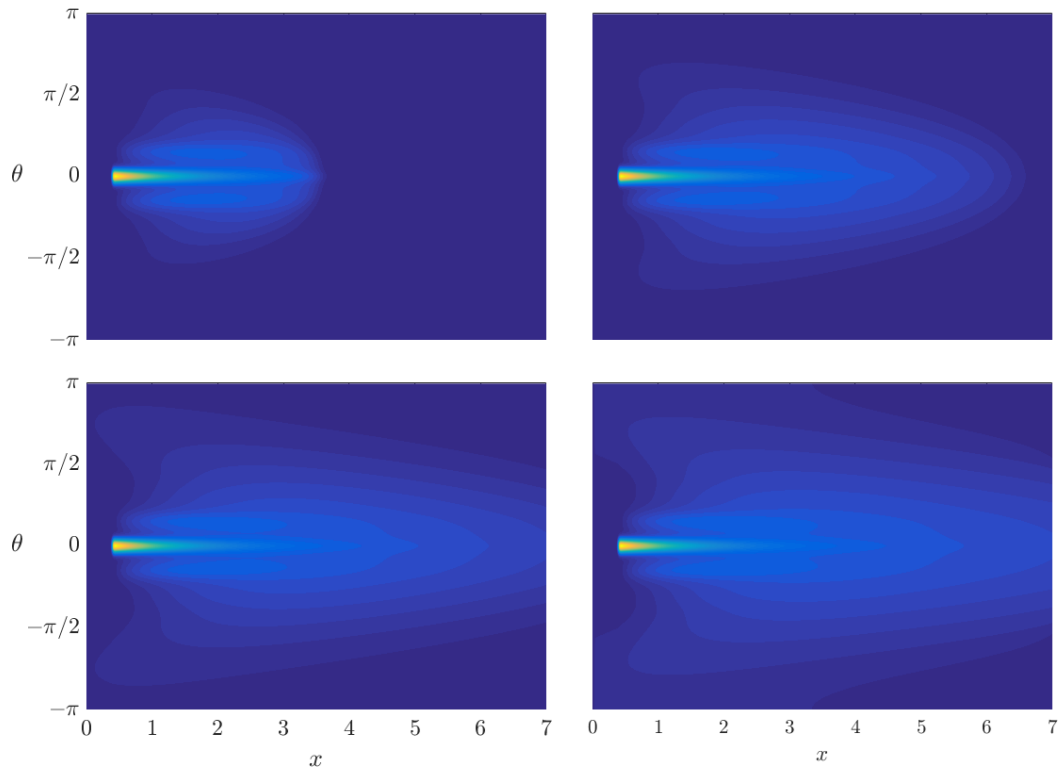

Figure 3-6. Wave-energy density $a(x, \theta, t)$ at $t = 8,\ 16,\ 32$ and 80 days obtained by solving the kinetic equations numerically with parameters matching those of Figure 3-3. The x-axis is in units of 1000 km. Note that for $|\theta| > \pi/2$ the group velocity changes sign so we observe energy propagating to the left. This return of energy from larger values of x is responsible for the faint signal observed for $k < 0$ in panel (a) of Figure 3-4, which corresponds to the region where the IT is forced at $x = 400$ km.

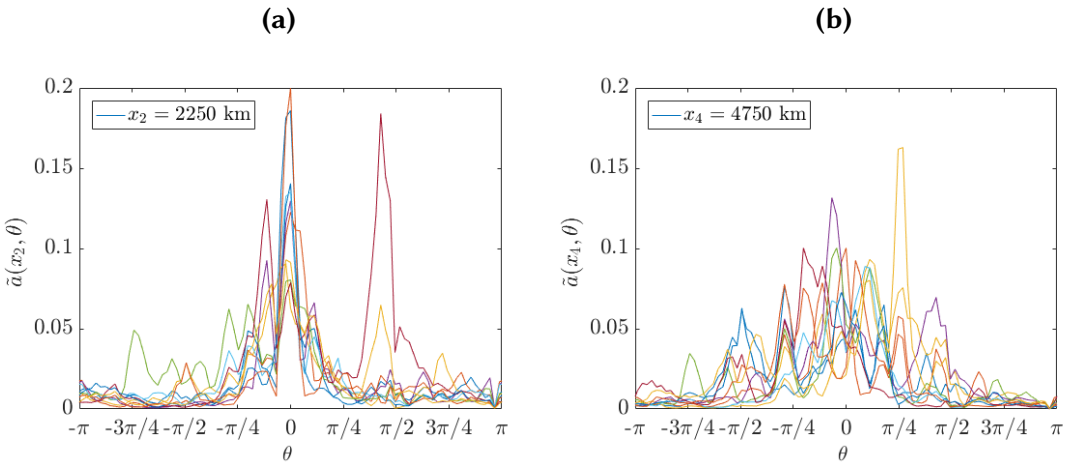

Figure 3-7. Energy density from 10 realisations of shallow-water simulations evaluated (a) in the second box of Figure 3-4), centred about $x_2 = 2250$ km, and (b) in the fourth box, centred about $x_4 = 4750$ km. This figure illustrates the limited predictive power of the kinetic equation, which is based upon ensemble averaged quantities, for any single realisation.

the value of the kinetic equation in predicting the generic properties of the scattering and their dependence on the various parameters in the problem.

We emphasise that the kinetic equation yields only ensemble average predictions and cannot describe the details of the effect of a single flow realisation on the IT. To illustrate how the scattering fluctuates between realisations, we show in Figure 3-7 the energy density $\tilde{a}$ estimated from single shallow-water simulations. While fluctuations can be large, the typical behaviour is a redistribution of energy in the angular direction that is well captured by the ensemble-averaged predictions. Furthermore, ergodicity implies that the ensemble average deductions of the kinetic equation apply accurately to quantities that are spatial averages over many eddy scales.

3-5 Discussion

This chapter examines the scattering of oceanic ITs – or indeed of any IGW – caused by the turbulent mesoscale flow in which they propagate. Assuming that the flow is barotropic, weak (small Rossby number) and random with stationary and homogeneous statistics, we derive the kinetic equation (3-2.5) governing energy exchanges between waves travelling in different directions. A key outcome is the

scattering cross section (3-2.16), or (3-3.2) for an isotropic flow, which measures the energy transfer rate as a function of the wavevectors involved and other parameters. The scattering cross section depends linearly on the energy spectrum of the flow.

The form of the scattering cross section shows that the energy exchanges between waves are restricted to waves with the same frequency and hence the same horizontal wavenumber. Therefore, while scattering results in a complex random wavefield, this field has a single spatial scale determined by the forcing frequency. This is obvious for a time-independent flow but perhaps less so for the time-dependent flows we consider for which it is a consequence of the statistical stationarity of the flows. Note that this does not imply that the wavefield is completely phase-locked in time: slow phase variations result from the interaction with a time-dependent flow (Ponte and Klein, 2015; Dunphy *et al.*, 2017), but these are not described by our analysis, which focuses on the wave amplitude as measured by the energy density $a(\boldsymbol{x}, \boldsymbol{k}, t)$. It would be of interest to study the phase variations from the statistical viewpoint taken here.

For an isotropic flow, scattering leads to an equilibrium isotropic wavefield over a time scale that we can estimate from the Fourier transform of the scattering cross section (3-3.2). At equilibrium, and in the absence of spatial modulations, the wave energy density is $a(\boldsymbol{k}) = a(|\boldsymbol{k}|) \propto \delta(|\boldsymbol{k}| - k_0)$ with $k_0 = \sqrt{(\omega^2 - f^2)/gh}$, corresponding to a correlation function $\int a(|\boldsymbol{k}|)\, \mathrm{e}^{\mathrm{i}\boldsymbol{k}\cdot\boldsymbol{x}}\, \mathrm{d}\boldsymbol{k} \propto \int \delta(|\boldsymbol{k}| - k_0)\, \mathrm{e}^{\mathrm{i}\boldsymbol{k}\cdot\boldsymbol{x}}\, \mathrm{d}\boldsymbol{k}$ that is proportional to the Bessel function $J_0(k_0|\boldsymbol{x}|)$. Thus, while the flow controls the speed of convergence towards the isotropic wave-energy distribution, it has no effect on the form of this distribution.

The time scale necessary for scattering to significantly alter the wave field is deduced from the scattering cross section and found to be of the order of a few days to a week. This is short compared with time scales associated with nonlinear wave–wave interactions (see Ward and Dewar, 2010), which raises the possibility that scattering is as crucial as the more widely considered wave–wave interactions in shaping the IGW spectrum in the ocean. Note however that, as this asymptotic treatment makes clear, the large time-scale separation between IGWs and the quasigeostrophic flow implies that scattering causes little frequency broadening and so cannot by itself explain the continuum of observed frequencies.

The conclusion that scattering simply relaxes wave energy towards an isotropic equilibrium depends crucially on the two-dimensional setup implied by our assumption of barotropic flow. It holds because scattering redistributes wave energy in

Fourier space over constant-frequency curves which, in this case, are just circles, hence compact. As we see in later chapters, this picture changes radically in the presence of vertical shear since this causes energy exchanges between different vertical wavenumbers. The relevant constant-frequency set is then a cone in wavevector space. Because this cone is unbounded, no finite-energy equilibrium exists, and the energy of an initially plane wave can be expected to cascade to small scales, both horizontally and vertically and with a fixed aspect ratio, as it spreads on the cone. This scenario, already envisioned by Lelong and Riley (1991) and Bartello (1995), is potentially important for the dissipation of oceanic IGWs, with implications for their impact on mixing and mesoscale dynamics and for the maintenance of balance. The framework we have adopted, which regards the flow as a prescribed random field and examines the wave statistics on the basis of a kinetic equation, generalises to the case of vertically sheared flow. It is well suited to describe and quantify the scale cascade that results from what is then a fully three-dimensional scattering.

Chapter 4

Diffusion of IGWs by geostrophic turbulence

4-1 Introduction

The dynamics of rotating stratified fluids, most notably the atmosphere and ocean, are characterised by the coexistence of vortical flow and inertia-gravity waves (IGWs). These evolve independently at a linear level but interact to an increasing degree as flow strength and wave amplitude increase. It is important to understand the various processes affecting the propagation and evolution of IGWs since they play a key role in the energy balance of the atmosphere and ocean. IGWs are able to propagate freely for great distances of hundreds of kilometres in the ocean before they break, transferring energy in both physical and spectral space as a result. We highlighted in Chapter 1 some of the other important ways IGWs affect the climate and general circulation.

The overwhelming majority of the previous work in this direction has been dedicated to studying the process of nonlinear wave–wave interactions, and how they might explain the observed properties of IGWs such as the "universal" Garrett and Munk spectrum (Müller *et al.*, 1986). This focus was partly due to the early recognition that such interactions can provide the link from large to small scales through processes such as parametric subharmonic instability and induced diffusion (e.g.McComas and Bretherton (1977); Olbers (1976); Henyey and Pomphrey (1983); Meiss and Watson (1982)), and partly since the original Lagrangian–based approaches

specifically preclude interactions with the vortical mode from appearing (Müller *et al.*, 1986; Flatté *et al.*, 1985; Staquet and Sommeria, 2002). Much of this earlier work focused on the interactions of short-waves scattered by larger-scale waves, in order to take advantage of convenient analytic techniques such as the WKB (or eikonal) approximation (Müller *et al.*, 1986; Henyey and Pomphrey, 1983; McComas and Bretherton, 1977; Flatté *et al.*, 1985; Olbers, 1976; Müller, 1976; Watson, 1985).

Work which included the wave–vortical mode interactions came later, notably Warn (1986); Lelong and Riley (1991) and Bartello (1995), showing that in weakly nonlinear regimes the balanced mode can facilitate IGW energy cascades to small scales through so-called 'catalytic interactions' – triadic interactions that leave the energy of the balanced mode unchanged while redistributing IGW energy in wavenumber space. The importance of this mechanism has been investigated for rotating shallow–water models which, though they do not support a scale cascade, have established that the IGW field can be scattered and isotropised by interactions with the balanced flow on time scales that rival the fastest wave–wave interactions (Ward and Dewar, 2010; Savva and Vanneste, 2018). It has been demonstrated through a combination of statistical mechanics based arguments and numerical investigations that a cascade of wave energy to small scales can also be achieved through catalytic interactions (Bartello, 1995; Waite and Bartello, 2006a), though there has been no quantitative theory to describe how the cascades unfold.

In this chapter we provide a quantitative description by deriving a simplified model for the dynamics of IGWs in a low-Rossby-number, homogeneous and horizontally isotropic turbulent flow in geostrophic balance. We derive a diffusion equation that captures the spreading of IGWs in wavenumber space or, more precisely, on a cone in this space corresponding to fixed-frequency IGWs. The diffusivity components associated with radial and angular diffusion on the cone are obtained in closed forms involving the IGW parameters and the energy spectrum of the geostrophic flow. Early versions were proposed by Müller and Olbers (1975) and Müller (1976, 1977).

We solve the diffusion equation for an initial-value problem (§4-3) and a steady forced problem (§4-4), assuming horizontally isotropic IGW fields, and we test the results against numerical simulations of the three-dimensional Boussinesq equations, finding good agreement in both cases. With forcing, the diffusion equation predicts a constant-flux, steady energy spectrum scaling with wavenumber as k^{-2} which is realised numerically.

Our results are relevant to important open questions about the nature of submesoscale motion in the ocean and mesoscale motion in the atmosphere. As described in Chapter 1, analyses by Bühler *et al.* (2014) and Callies *et al.* (2014, 2016) led them to hypothesise these motions are dominated by almost linear IGWs. The prediction of a k^{-2} spectrum lends support to this hypothesis by identifying a robust mechanism – diffusion by turbulence – that produces a spectrum consistent with observations (see §4-4). As for the initial-value predictions, they provide estimates for the time scale of the scale cascade of the IGWs that leads ultimately to their dissipation.

This chapter has been adapted from *Diffusion of inertia–gravity waves by geostrophic turbulence*, published in the Journal of Fluid Mechanics (Kafiabad *et al.*, 2019). The simulations of the Boussinesq equations in this chapter were carried out by H. A. Kafiabad, and the derivations were completed collaboratively.

4-2 Diffusion in wavenumber space

We consider the dynamics of IGWs propagating in a turbulent vortical flow of much larger spatial scale so that the WKB approximation applies. Chapter 2 presented a recipe for deriving a kinetic equation in the form of a scattering integral that is valid in the scattering, or radiative transfer, regime which was based on the method of Ryzhik *et al.* (1996). Similarly, in the diffusion approximation (see Figure 2-1) for which the WKB approximation holds, Bal *et al.* (2010) §4 describes a rigorous procedure for deriving a diffusion equation based on the conservation of wave energy in the $(\boldsymbol{x}, \boldsymbol{k})$ phase space.

We take the appropriate equation from Bal *et al.* (2010) as given for our starting point, written here as

$$\partial_t a + \nabla_{\boldsymbol{k}}\Omega \cdot \nabla_{\boldsymbol{x}} a - \nabla_{\boldsymbol{x}}\Omega \cdot \nabla_{\boldsymbol{k}} a = 0. \tag{4-2.1}$$

Here $a(\boldsymbol{x}, \boldsymbol{k}, t)$ is the IGW energy density, and $\Omega = \omega + \boldsymbol{U}\cdot\boldsymbol{k}$ is the absolute frequency which sums the intrinsic frequency

$$\omega = \sqrt{f^2\cos^2\theta + N^2\sin^2\theta}, \tag{4-2.2}$$

where $f < N$ are the Coriolis and buoyancy frequencies and θ is the angle between the wavevector $\boldsymbol{k}$ and the vertical, and the Doppler shift $\boldsymbol{U} \cdot \boldsymbol{k}$, where $\boldsymbol{U} = \boldsymbol{U}(\boldsymbol{x}, t)$ is the vortical flow velocity.

Equation 4-2.1 is the Liouville equation, describing conservation of energy density in phase space. The Liouville equation arises in phase space descriptions of geometrical optics (Jin and Wen, 2006), which is the classical mechanics approximation of wave propagation. It is thus applicable for the scaling regime we consider with waves varying on spatial scales much smaller than the inhomogeneities of the background medium – the turbulent flow in this case. Exploiting this approximation allows us to take a direct and simple route to obtain a kinetic equation of the form (2-1.4), by taking a phase space description as a starting point rather than extending the full model for wave propagation into phase space by way of the Wigner transform, as in Chapter 2. This route further departs from the derivation of the kinetic equation outlined in Chapter 2 since energy conservation is built in from the outset, whereas the conservation in the scattering regime was shown to be contingent on just the linear equations for the waves conserving energy. The route to the kinetic equation described in Chapter 2 is more general but more complicated. In this regime we can choose to avoid the complexity of taking a full model for waves propagating in a background flow, instead incorporating the effect of the flow through its impact on the IGW frequency.

In particular, assuming that the flow is (i) weak enough that $\omega \gg \boldsymbol{U} \cdot \boldsymbol{k}$, (ii) evolving on a time scale much longer than ω^{-1}, and (iii) well modelled by a homogeneous and stationary random field, we can approximate (4-2.1) by

$$\partial_t a + \boldsymbol{c} \cdot \nabla_{\boldsymbol{x}} a = \nabla_{\boldsymbol{k}} \cdot (\mathbf{D} \cdot \nabla_{\boldsymbol{k}} a) \,, \tag{4-2.3}$$

where $\boldsymbol{c} = \nabla_{\boldsymbol{k}} \omega$ is the intrinsic group velocity and $\mathbf{D}$ a $\boldsymbol{k}$-dependent diffusivity tensor. We relegate the details of the derivation to Appendix C.

Note that although we have omitted some details in this chapter by appealing to the method of Bal *et al.* (2010), we present the alternate derivation of (4-2.3) in Chapter 5 by taking the WKB limit of the scattering integral form of a kinetic equation which is derived in full detail, starting from the full model for wave propagation. The resulting kinetic equations for the leading-order phase space energy density are identical, and taking the two approaches provides a valuable opportunity to cross-check for correctness.

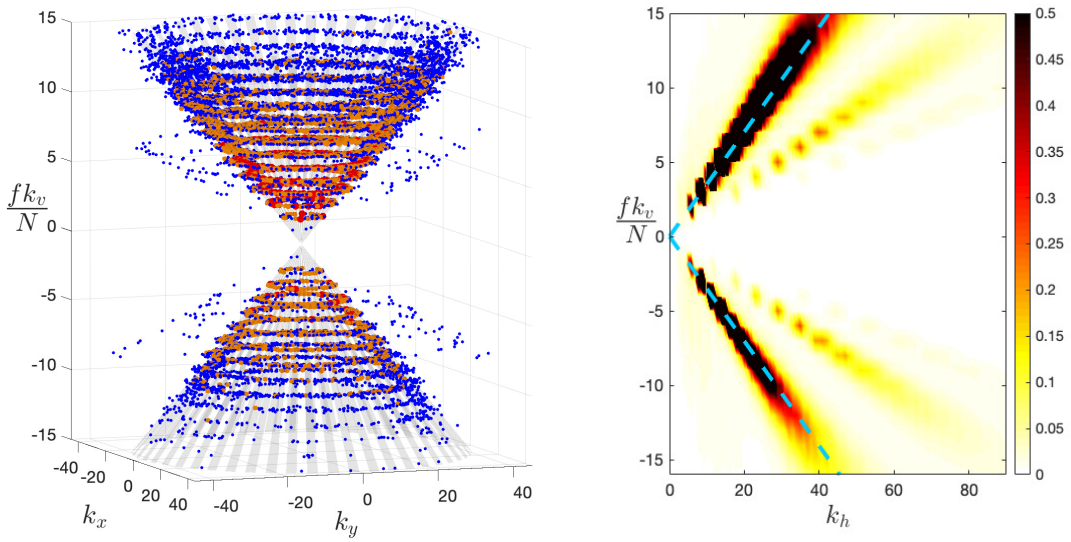

Figure 4-1. Left: IGW energy density $e(\boldsymbol{k})$ in $\boldsymbol{k}$-space at $t = 389f^{-1}$ for the initial-value simulation of §4-3 with $\omega = 3f$ and $\mathrm{Ro} = 0.057$. • represents the wave modes with $e(\boldsymbol{k})/e_{\max} > 0.1$ (e_{max} the maximum energy density), • $0.01 < e(\boldsymbol{k})/e_{\max} < 0.1$, and • $0.03 < e(\boldsymbol{k})/e_{\max} < 0.01$. Right: projection of $e(\boldsymbol{k})$ onto the $(k_\mathrm{h}, k_\mathrm{v})$-plane. The constant-frequency cone defined by (4-2.2) is indicated by grey stripes on the left and dashed lines on the right.

The right-hand side of (4-2.3) captures the scattering of wave energy that results from small-but-sustained random Doppler shifting by the flow; in the regime considered, this naturally leads to diffusion in $\boldsymbol{k}$-space. In Cartesian coordinates, the diffusivity tensor takes the form

$$D_{ij}(\boldsymbol{k}) = -\frac{1}{2}k_m k_n \int_{-\infty}^{\infty} \frac{\partial^2 \Pi_{mn}}{\partial x_i \partial x_j}(\boldsymbol{c}(\boldsymbol{k})s)\,\mathrm{d}s, \tag{4-2.4}$$

where $\Pi_{mn}(\boldsymbol{x}) = \langle U_m(\boldsymbol{y}+\boldsymbol{x})U_n(\boldsymbol{y})\rangle$ is the velocity correlation tensor, with $\langle\cdot\rangle$ denoting ensemble average, and summation over repeated indices is implied. An analogous expression was obtained by McComas and Bretherton (1977) in the context of wave–wave interactions in the induced-diffusion regime (see Müller *et al.*, 1986, §5, for a review). Müller and Olbers (1975) and Müller (1976, 1977) discussed a flow-induced diffusivity that differs from (4-2.4) to account heuristically for wave–wave interactions and dissipation.

A key property of (4-2.4) is that $\mathbf{D}(\boldsymbol{k}) \cdot \boldsymbol{c}(\boldsymbol{k}) = 0$ since

$$D_{ij}(\boldsymbol{k}) \cdot c_j(\boldsymbol{k}) = -\frac{1}{2} k_m k_n \int_{-\infty}^{\infty} \frac{\mathrm{d}}{\mathrm{d}s} \left(\frac{\partial \Pi_{mn}}{\partial x_i}(\boldsymbol{c}(\boldsymbol{k})s) \right) \mathrm{d}s = 0.$$

Thus there is no diffusion in the direction of the group velocity $\boldsymbol{c}$. Since $\boldsymbol{c}$ is perpendicular to constant-frequency surfaces, for the IGW dispersion relation (4-2.2) diffusion is restricted to the cones $\theta = \mathrm{const}$, see Fig. 4-1. This is because diffusion in $\boldsymbol{k}$-space stems from resonant-triad interactions between two IGWs and one vortical mode (also termed balanced mode) associated with the flow. The flow is treated as a zero-frequency mode because it evolves slowly compared with ω^{-1}, so the resonance condition implies that the interacting IGWs have the same frequency. The restriction to a single frequency means that wave action and wave energy only differ by a constant multiple and can be identified with one another.

We particularise (4-2.4) to IGWs and geostrophic flows using the dispersion relation (4-2.2) and the geostrophic balance satisfied by the velocity in Π_{mn}. It is natural to use spherical polar coordinates (k, φ, θ) in $\boldsymbol{k}$-space and a Fourier counterpart to Π_{mn} in the form of the vortical flow kinetic energy spectrum $E(K_\mathrm{h}, K_\mathrm{v})$, which we assume to be horizontally isotropic so that it only depends on the horizontal and vertical wavenumbers K_h and K_v (for clarity we systematically use lowercase symbols for coordinates in the IGW wavenumber space and uppercase symbols for coordinates in the flow wavenumber space). Computations detailed in Appendix C then reduce (4-2.3) to

$$\partial_t a = \frac{1}{k^2} \partial_k (k^2 D_{kk} \partial_k a) + \frac{D_{\varphi\varphi}}{k^2 \sin^2\theta} \partial_{\varphi\varphi} a, \tag{4-2.5}$$

under the further assumption of spatial homogeneity $\nabla_{\boldsymbol{x}} a = 0$. This makes it plain that there is no diffusion in the direction of θ. Hence, θ, or equivalently ω, can be treated as a fixed parameter. The only non-zero components of the diffusivity tensor are given by

$$D_{kk} = Bk^3 \iint\limits_{K_\mathrm{h}^2/K_\mathrm{v}^2 > \tan^2\theta} \frac{K_\mathrm{v}^2}{K_\mathrm{h}} \left(\cot^2\theta - \frac{K_\mathrm{v}^2}{K_\mathrm{h}^2} \right)^{1/2} E(K_\mathrm{h}, K_\mathrm{v}) \, \mathrm{d}K_\mathrm{h} \mathrm{d}K_\mathrm{v}, \tag{4-2.6a}$$

$$\frac{D_{\varphi\varphi}}{\sin^2\theta} = Bk^3 \iint\limits_{K_\mathrm{h}^2/K_\mathrm{v}^2 > \tan^2\theta} K_\mathrm{h} \left(\cot^2\theta - \frac{K_\mathrm{v}^2}{K_\mathrm{h}^2} \right)^{3/2} E(K_\mathrm{h}, K_\mathrm{v}) \, \mathrm{d}K_\mathrm{h} \mathrm{d}K_\mathrm{v},$$

where

$$B = \frac{\omega \sin^2\theta}{4\pi^3(N^2 - f^2)|\cos^5\theta|}$$

depends solely on θ, N and f.

Along with suitable boundary conditions, eqs. (4-2.5)–(4-2.6) provide a full description of the diffusion of IGW on the constant-frequency cone in $\boldsymbol{k}$-space for a turbulent flow of given energy spectrum. In the angular φ-direction, this diffusion leads to an isotropisation of the wave field with rate $\mathsf{D}_{\varphi\varphi}/(k^2\sin^2\theta)$. In the radial k-direction, the diffusion leads to a forward cascade of the wave energy to high wavenumbers where it is efficiently dissipated by viscous processes. We impose the boundary conditions $a(\boldsymbol{k} = 0, t) = 0$, at the apex of the cone, and $\lim_{k\to\infty} a(k, \varphi, \theta, t) = 0$. Note that wave energy remains confined to one nappe of the cone corresponding to either upward- or downward-propagating IGWs. This is only an approximation; exchanges between upward- and downward-propagating waves do occur, but they are asymptotically small and not captured by the WKB approximation. In what follows, we concentrate on radial diffusion by assuming wave statistics independent of φ, $\partial_\varphi a = 0$, leaving the study of horizontal isotropisation for future work.

4-3 Initial-value problem

For $a = a(k, t)$, we rewrite (4-2.5) as

$$\partial_t e = \partial_k \left(Q k^5 \partial_k \left(k^{-2} e \right) \right), \tag{4-3.1}$$

where we have introduced $e(k, t) = 2\pi k^2 \sin\theta\, \omega a(k, t)$ and the k-independent parameter $Q = \mathsf{D}_{kk}/k^3$. The function $e(k, t)$ is the IGW energy density in k, with $e(k, t)\,\mathrm{d}k$ the energy contained within the interval $[k, k + \mathrm{d}k]$. We solve (4-3.1) with initial condition $e(k, 0) = \delta(k - k_*)$ corresponding to the excitation of IGWs with a single wavenumber k_*. (The solution associated with arbitrary initial condition can be deduced by integration over k_*.) We show in Appendix C-3 that

$$e(k, t) = \tfrac{1}{2} k_*^{-2} \int_0^\infty J_4(k^{-1/2}\lambda) J_4(k_*^{-1/2}\lambda) \mathrm{e}^{-Q\lambda^2 t/4} \lambda \,\mathrm{d}\lambda, \tag{4-3.2}$$

where J_4 is a Bessel function of the first kind (*NIST Digital Library of Mathematical Functions*, 2018). The large-time behaviour of $e(k,t)$ is readily deduced as $e(k,t) \propto k^{-2}t^{-5}$ away from an asymptotically small neighbourhood of $k = 0$ (see Appendix C-3). An inverse diffusion time scale can be read off from (4-3.2) as Qk_*. Using (4-2.6) this can be written in the dimensionless form

$$\frac{Qk_*}{\omega} = \gamma \frac{N^2}{N^2 - f^2} \frac{k_*}{K_{\mathrm{h}*}} \mathrm{Ro}^2, \tag{4-3.3}$$

where γ is a dimensionless 'geometric' factor that depends only on θ and the shape (but not the magnitude) of the flow kinetic-energy spectrum and $\mathrm{Ro} = K_{\mathrm{h}*}\langle|\boldsymbol{U}|^2\rangle^{1/2}/f$ is a flow Rossby number. The typical horizontal and vertical inverse flow scales $K_{\mathrm{h}*}$ and $K_{\mathrm{v}*}$ are assumed to be related by $K_{\mathrm{v}*} = NK_{\mathrm{h}*}/f$. Eq. (4-3.3) captures the dependence of the diffusion time scale on the Rossby number and on the scale separation between IGWs and flow. The diffusion approximation requires $Qk_*/\omega \ll 1$ in addition to the WKB conditions $k_* \sin\theta \gg K_{\mathrm{h}}$ and $k_* \cos\theta \gg K_{\mathrm{v}}$.

We verify the solution of (4-3.1) against simulations of the three-dimensional non-hydrostatic Boussinesq equations. These are solved using a code adapted from that in Waite and Bartello (2006b) which relies on a de-aliased pseudospectral method and a third-order Adams–Bashforth scheme with timestep $0.015/f$. The triply-periodic domain, $(2\pi)^3$ in the scale coordinates $(x, y, z' = Nz/f)$, is discretised uniformly with 768^3 grid points. A hyperdissipation of the form $-\nu(\partial_x^2 + \partial_y^2 + \partial_{z'}^2)^4$, with $\nu = 2 \times 10^{-17}$, is employed in the momentum and density equations. We take $N/f = 32$, a representative value of mid-depth ocean stratification. The initial condition is the superposition of a turbulent flow, obtained by running a quasigeostrophic model to a statistically stationary state, and IGWs. The initial spectrum of the vortical flow peaks at $K_{\mathrm{h}*} \simeq 4$ and has an inertial subrange scaling approximately as K_{h}^{-3} and K_{v}^{-3}. This spectrum evolves slowly over the IGW-diffusion timescale, and an average is used to calculate D_{kk} in (4-2.6a), and hence Q in (4-3.1). We report experiments with the two Rossby numbers $\mathrm{Ro} = K_{\mathrm{h}*}\langle|\boldsymbol{U}|^2\rangle^{1/2}/f = 0.057,\ 0.117$ (or $\langle\zeta^2\rangle^{1/2}/f = 0.1,\ 0.2$ for the alternative Rossby numbers based on the vertical vorticity ζ), and the two IGW frequencies $\omega = 2f,\ 3f$. Upward-propagating IGWs are initialised as a ring in $\boldsymbol{k}$-space with $k_{\mathrm{h}*} = 16$, $k_{\mathrm{v}} = \cot\theta\, k_{\mathrm{h}}$, random phases, and an initial kinetic energy $\langle|\boldsymbol{u}|^2\rangle/2 = 0.1\langle|\boldsymbol{U}|^2\rangle/2$. The IGW spectrum $e(k,t)$ is computed following the normal-mode decomposition of Bartello (1995).

Fig. 4-1, obtained for the lower Ro and $\omega = 3f$, illustrates the confinement

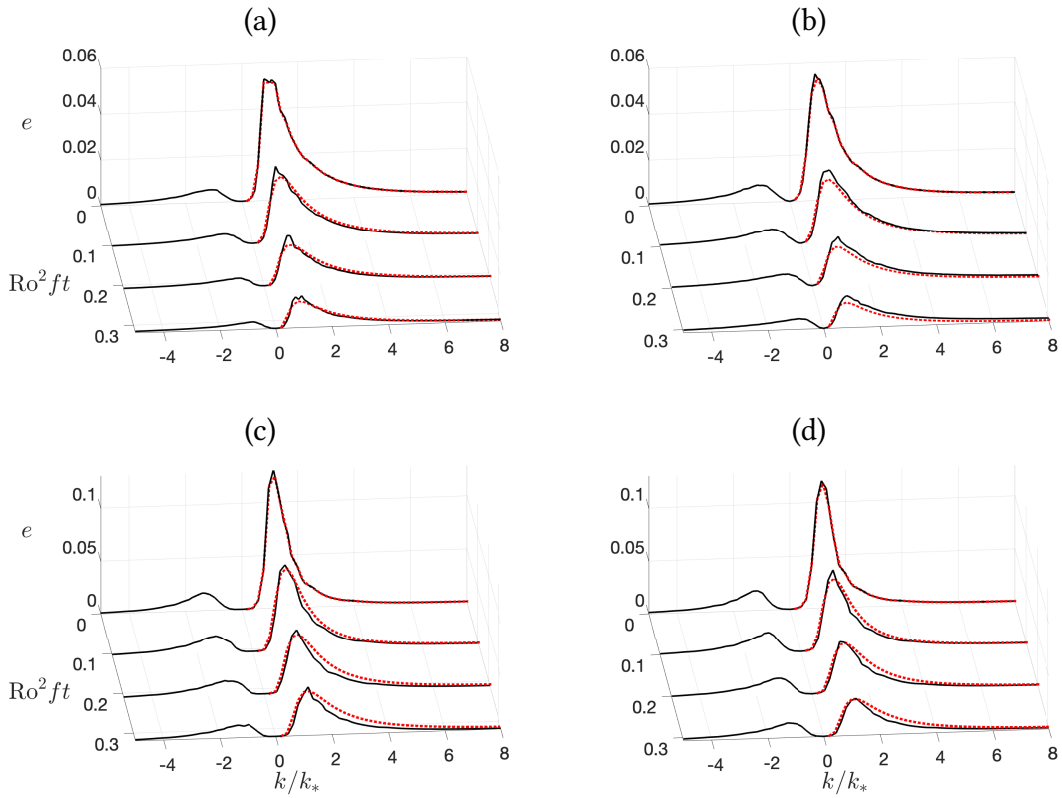

Figure 4-2. Evolution of the IGW energy $e(k,t)$ in Boussinesq simulations (solid, black) and as predicted by the diffusion approximation (dotted, red) for (a) $\omega = 2f$, $\mathrm{Ro} = 0.057$, (b) $\omega = 2f$, $\mathrm{Ro} = 0.117$, (c) $\omega = 3f$, $\mathrm{Ro} = 0.057$ and (d) $\omega = 3f$, $\mathrm{Ro} = 0.117$. Conventionally, $k > 0$ ($k < 0$) corresponds to upward- (downward-)propagating IGWs. This figure illustrates robustness of the diffusion approximation over a range of finite Ro.

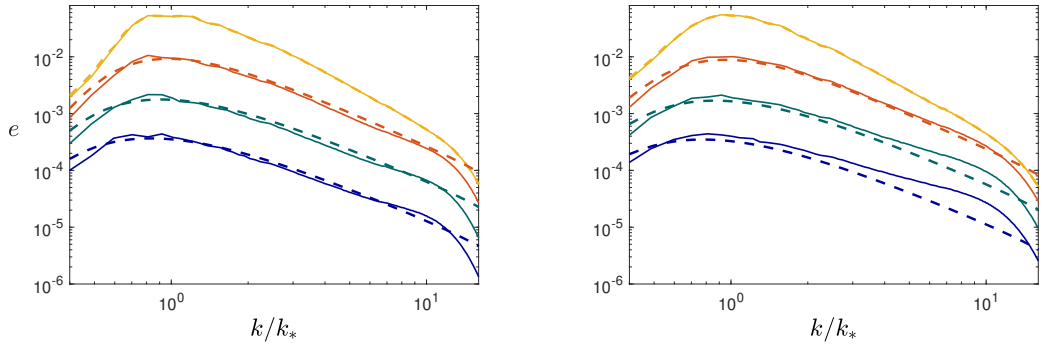

Figure 4-3. Log-log representation of the IGW spectra in Figs. 4-2(a) (left, $\omega = 2f$, $\mathrm{Ro} = 0.057$) and 4-2(b) (right, $\omega = 2f$, $\mathrm{Ro} = 0.117$). The solid lines are the results of the Boussinesq simulation and the dashed lines the predictions of the diffusion approximation. The curves correspond to the times shown in Fig. 4-2(a–b) and are successively shifted downward by half a decade for clarity.

of wave energy on the constant-frequency cone, one of the keys to the validity of the diffusion approximation. The confinement is of course not perfect and some energy appears around the cones associated with the harmonic frequencies 2ω and 3ω. Fig. 4-2 shows the evolution of $e(k,t)$ for the four sets of values of (Ro,ω). The numerical results are compared with the predictions of the diffusion equation obtained by solving (4-3.1) initialised with the form of $e(k,t_\mathrm{a})$ extracted from the simulation after an adjustement time $t_\mathrm{a} > 0$. This procedure accounts for the fact that the diffusion equation (4-2.3) is only valid after an adjustment period, requiring $t_\mathrm{a} \gg (K_*|\boldsymbol{c}|)^{-1}$, the time to traverse typical eddies at the IGW group speed (cf. Müller *et al.*, 1986, §5). The agreement between the numerical simulation and the diffusion approximation is remarkable considering the complexity of the full Boussinesq dynamics and the moderate separation of spatial scales between IGWs and flow. As the diffusion approximation predicts, the simulations with different Rossby numbers behave similarly when t is scaled suitably. The decay is slower for $\omega = 3f$ than $\omega = 2f$, consistent with a decrease in Q obtained when evaluating (4-2.6a). Scattering from upward-propagating to downward-propagating IGWs, neglected in the diffusion approximation, occurs; it is more substantial for the larger ω because the two nappes of the constant-frequency cones are closer together, facilitating energy transfers. Fig. 4-3 displays the wave energy spectrum $e(k,t)$ obtained for $\omega = 2f$ (top row of Fig. 4-2) in log–log coordinates. It shows that the good agreement between numerical and predicted spectra extends to large wavenumbers for $\mathrm{Ro} = 0.057$ but

not for the larger Rossby, $\mathrm{Ro} = 0.117$, at the later times. We note that the wave energy is then very small and may be affected by a contribution associated with spontaneous generation (cf. Kafiabad and Bartello, 2018)

4-4 Forced response and observed ocean and atmosphere spectra

We now turn to the steady solution of (4-3.1) in the presence of a forcing of the form $\delta(k - k_*)$. Eq. (4-3.2) admits two steady solutions: the no-flux solution $e(k) \propto k^2$ and the constant-flux solution $e(k) \propto k^{-2}$. Matching these at k_* yields the steady spectrum

$$e(k) = \frac{1}{4Qk_*^2} \begin{cases} (k/k_*)^2 & \text{for } 0 < k < k_* \\ (k_*/k)^2 & \text{for } k > k_* \end{cases}. \tag{4-4.1}$$

Note that for IGWs with a single frequency and correspondingly a single angle θ_*, the horizontal energy spectrum $e_\mathrm{h}(k_\mathrm{h})$ satisfies the same power laws as $e(k)$ since

$$e_\mathrm{h}(k_\mathrm{h}) = \iiint \delta(k\sin\theta - k_\mathrm{h}) \frac{e(k)\delta(\theta - \theta_*)}{2\pi k^2 \sin\theta} \,\mathrm{d}\boldsymbol{k} = \csc\theta_* e(k_\mathrm{h}\csc\theta_*),$$

using that the energy density in $\boldsymbol{k}$-space is $e(k)\delta(\theta - \theta_*)/(2\pi k^2 \sin\theta)$. Thus, (4-4.1) implies a k_h^{-2} horizontal spectrum at large k_h. This remains true for a superposition of IGWs with different frequencies, corresponding to an integration over θ_*.

We confirm the prediction (4-4.1) by the simulation of the Boussinesq equations in the presence of forcing. In the simulation reported, all the specifications are the same as in §4-3 except for the initial condition, which is devoid of IGWs. Instead, an Ornstein–Uhlenbeck forcing with short correlation time (3 timesteps) is applied to the waves with $\omega = 2f$ (see Waite, 2017). The forcing amplitude is adjusted so that the wave energy is about 0.01 of the vortical flow energy after reaching a stationary state. Fig. 4-4 shows the stationary spectra for $\mathrm{Ro} = 0.057$ and 0.117. For the low Rossby number, the prediction (4-4.1) is well borne out by the simulation results with a clean k_h^{-2} spectrum spanning nearly a decade from the forcing scale down to dissipation. For the high Rossby number, the spectrum shallows a little from wavenumber 40 or so to take a shape more consistent with $k_\mathrm{h}^{-5/3}$. Two mechanisms can be invoked to explain this shallowing: the Doppler term is not weak compared with the intrinsic

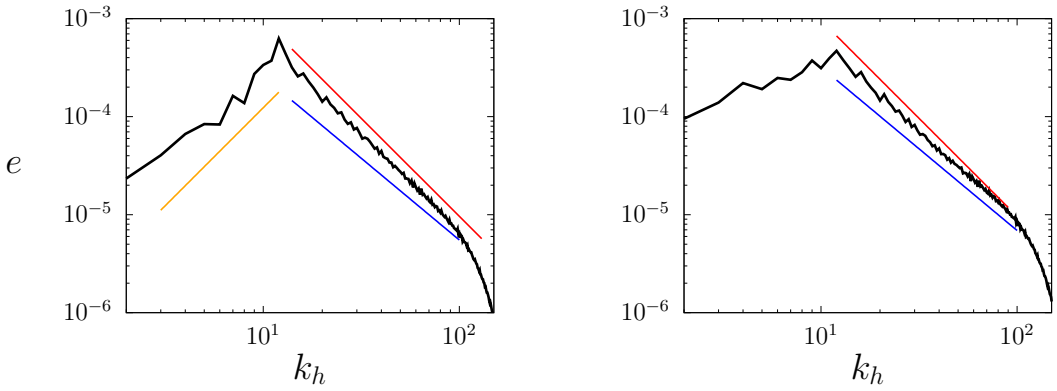

Figure 4-4. Stationary horizontal energy spectrum $e(k_\mathrm{h})$ for the forced simulations in §4-4 with $\mathrm{Ro} = 0.057$ (left) and 0.117 (right). Straight lines indicate the power laws: — k^{-2}, — $k^{-5/3}$ and — k^{2}.

IGW frequency, invalidating the diffusion approximation, or nonlinear wave–wave interactions become significant. We can roughly estimate the wavenumbers at which each of these mechanisms is important as

$$k_\mathrm{h} \sim \frac{\omega}{\langle|\boldsymbol{U}|^2\rangle^{1/2}} \sim \frac{K_{\mathrm{h}*}}{\mathrm{Ro}} \quad \text{and} \quad k_\mathrm{h} \sim \frac{K_{\mathrm{h}*}}{\mathrm{Ro}} \frac{\langle|\boldsymbol{U}|^2\rangle^{1/2}}{\langle|\boldsymbol{u}|^2\rangle^{1/2}},$$

corresponding to order-one Rossby numbers based on the wave lengthscale k_h^{-1} and on the root-mean-square velocity of, respectively, the vortical flow and the IGWs. For the simulation with $\mathrm{Ro} = 0.117$, these wavenumbers are about 40 and 400, suggesting that the shallowing of the spectrum is associated with the breakdown of the assumption of weak Doppler shift.

The prediction of a k_h^{-2} spectrum is significant in view of the ubiquity of this scaling in ocean and atmosphere observations. In the ocean, kinetic energy spectra show a k_h^{-2} dependence in the submesoscale range, say below 20 km, in regions of high mesoscale activity and in a larger range, below 200 km, in less active regions (see Callies and Ferrari (2013) for a comprehensive discussion). Recent analyses by Bühler *et al.* (2014) and Rocha *et al.* (2016) which separate the contribution of IGWs from that of geostrophic motion indicate that the IGW part of the spectrum follows a k_h^{-2} scaling in almost the entirety of its range. Our results above suggest that this may result from IGW energy diffusion by the geostrophic flow. Scales below 10 km or so are the realm of the Garrett and Munk (1972) spectrum, also associated with a k_h^{-2}

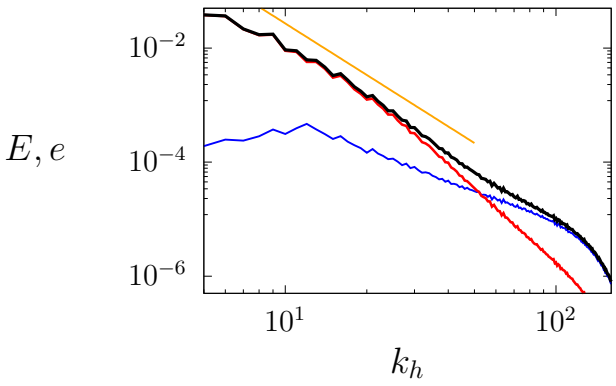

Figure 4-5. Stationary horizontal energy spectrum for the forced simulations in §4-4 with $\mathrm{Ro} = 0.117$: — total energy, — vortical energy E, — IGW energy e (same as on the right panel of Fig. 4-4), and — k_h^{-3} power law.

dependence. While this spectrum is generally attributed to wave–wave interactions (e.g. Müller *et al.*, 1986; Lvov *et al.*, 2012), interactions with the geostrophic flow may play a significant role, dominating for wavenumbers much smaller than (4-4b). We emphasise that theories based on linear IGWs, be it the diffusion approximation of this chapter or a more general theory accounting for strong Doppler shift, cannot predict the level of IGW spectrum nor its frequency content since both are determined by the forcing.

In the atmosphere, similarly, there is a broad range of scales, from 500 km to 10 km, where the energy spectrum scales approximately as k_h^{-2}. This is the shallow, mesoscale part of the celebrated Nastrom and Gage (1985) spectrum, which is traditionally interpreted as a $k_\mathrm{h}^{-5/3}$ spectrum but is also consistent with k_h^{-2}. There is ongoing debate about the nature of this part of the spectrum: Callies *et al.* (2014, 2016) attribute it to nearly linear IGWs on the basis of their separation between IGWs and geostrophic motion, but this interpretation is controversial (see Li and Lindborg (2018) for a recent critique). Callies *et al.* (2016) note that 'the wave interpretation is … not inconsistent with the observed power-law spectra … but an explanation for the spectral shape is so far missing'. Our results provide a possible explanation.

The total spectrum in the high-Ro simulation, shown in Fig. 4-5, is reminiscent of atmospheric observations, with a k_h^{-3} range at large scales associated with the

vortical flow, a k_{h}^{-2} range associated with nearly linear IGWs at intermediate scales, and a further shallowing at small scales (best seen in Fig. 4-4, right panel). While the diffusion approximation explains the k_{h}^{-2} range in our simulations, a degree of caution is required to draw a similar conclusion for the atmospheric spectrum since some of the underlying assumptions – weak flow with homogeneous statistics and relevance of the equilibrium spectrum in particular – are questionable.

4-5 Discussion

This chapter has examined the impact of a turbulent geostrophic flow on the statistics of small-amplitude IGWs. This impact has received less attention than that paid to wave–wave interactions. Yet the timescale found for a substantial effect of the geostrophic flow, of the order of $0.1\,\mathrm{Ro}^{-2}f^{-1}$ (see Fig. 4-2) corresponding to tens of days for ocean parameters, is similar to that of the fastest wave–wave interaction process (parametric subharmonic instability of internal tides at the critical latitude 29°, MacKinnon and Winters (2005)). This confirms the conclusions of Ward and Dewar (2010) and the work of the previous chapter (Savva and Vanneste, 2018) that scattering by the flow could dominate over wave–wave interactions in many ocean circumstances. A similar conclusion has been drawn from numerical simulations (Waite and Bartello, 2006a).

We have focused on the diffusive regime of IGW scattering that arises for weak flows and small-scale, linear IGWs. A remarkable feature of this regime is the prediction of a k_{h}^{-2} energy spectrum consistent with observations in both the ocean and atmosphere. We show in the next chapter that when the assumption of small scales is relaxed the wave energy obeys a kinetic equation, generalising the equations obtained by Danioux and Vanneste (2016) and the previous chapter in the case of inertial waves and IGWs in a barotropic flow respectively. The kinetic equation captures the transfer of energy between upward and downward-propagating IGWs which is negligible in the diffusive regime. When the assumption of weak flow is relaxed, as required for wavenumbers not small compared with (4-4a), IGWs are in the eikonal regime considered by Henyey and Pomphrey (1983) in the context of wave–wave interactions (see also Müller *et al.*, 1986, §5). It would be desirable to study the scattering by the geostrophic flow in this regime. We conclude by noting that the consistency between predicted and observed spectral slopes is only indicative:

further investigations are needed to establish the importance of IGW scattering in determining oceanic and atmospheric spectra.

Chapter 5

Scattering of IGWs by geostrophic turbulence

5-1 Introduction

It has become apparent in recent years that IGWs exist at larger scales and at greater energies, relative to vortical motions, than traditionally expected in the atmosphere and ocean. This has been seen particularly clearly as a consequence of the wave–balanced flow decomposition techniques due to Bühler *et al.* (2014) and Callies *et al.* (2014, 2016) where data obtained from flight paths and ship tracks are analysed using the linear modes and polarisation relations described in Chapter 1, §2. The method enables the empirical energy spectra to be partitioned into contributions due to the linear IGWs and a balanced geostrophic remainder, subject to assumptions on the underlying data such as isotropy, homogeneity, and linear dynamics. It was found that in some regions of the ocean, particularly those with less turbulent activity or at sites with significant internal tide generation, IGWs can dominate over the balanced flow even up to scales of around 100 km (Bühler *et al.*, 2014; Qiu *et al.*, 2017). Furthermore, this observation has been repeated using high-resolution global-scale simulations (e.g. Qiu *et al.* (2018)). Likewise, in the atmosphere IGWs can dominate through the submesoscale range up to around 500 km (e.g. Chapter 1 Figure 1-1; Callies *et al.* (2014, 2016)).

The work in the previous chapter (Kafiabad, Savva and Vanneste, 2019) demonstrates how important characteristics of IGWs could be understood as a result of interactions with the balanced mode, while also providing a faithful statistical description of the IGW energy cascades seen in a Boussinesq system in the form of a diffusion equation. The results of the previous chapter though are restricted to the WKB regime of short-waves weakly interacting with a large scale flow. In this chapter we extend our study of interactions of IGWs with the vortical mode by relaxing the assumption of spatial scale separation. This is achieved by applying the theory presented in Chapter 2 which yields a closed form kinetic equation capturing, in a statistically averaged sense, the possibly non-local redistribution of IGW energy across wavenumber space, as opposed to the local diffusive behaviour of Chapter 4. The theory is formulated in terms of a wavevector-resolving energy density $a(\boldsymbol{x}, \boldsymbol{k}, t)$ to capture spatial variations as well as the temporal evolution of the IGW energy spectrum. One of the key aspects of the kinetic equation is the restriction of transfers to a resonant surface of IGWs with equal frequencies. Whereas Chapter 3 was concerned with barotropic flows, which led to a shallow-water like system with no mechanism to transfer energy to different vertical wavenumbers, and hence to energy cascade to different spatial scales, in this chapter the resonant surface is a double cone in wavenumber space and cascades are supported. In testing the kinetic equation we restrict ourselves to spatially homogeneous and horizontally isotropic IGWs and flows (i.e. such that $\nabla_{\boldsymbol{x}} a = \partial_\varphi a = 0$, where φ is the azimuthal angle of the IGW wavevector in spherical coordinates), allowing a direct comparison with the results of Chapter 4. We leave the study of isotropisation and the effect of spatially inhomogenous flows for future work.

The plan for the chapter is as follows. We describe the standard equations satisfied by linear IGWs propagating in a weak geostrophic background flow in §5-2, along with details of an elimination of diagnostic variables to cast the system into a simple form. The calculations of Chapter 2 are then used to derive the kinetic equation in §5-2.2, and we discuss some of the properties of IGW scattering revealed by the kinetic equation in §5-4. In §5-5 we present comparisons of the kinetic equation with direct simulations of the fully nonlinear non-hydrostatic Boussinesq equations. First, in the short-wave regime where we can contrast the kinetic equation with the diffusion equation of Chapter 4, followed by simulations in the shared spatial-scale regime where the diffusion approximation breaks down, but the kinetic equation is valid. We conclude in §5-6 with a summary. The simulations of the Boussinesq equations in this chapter were carried out by H. A. Kafiabad.

5-2 Model for IGWs in geostrophic turbulence

5-2.1 Governing equations

We model the propagation of IGWs through a turbulent quasigeostrophic eddy field using the non-hydrostatic Boussinesq equations linearised about a background flow. The background flow is slowly dependent on time and geostrophically and hydrostatically balanced, given in terms of a random streamfunction ψ with homogeneous and stationary statistics. The background flow velocity and buoyancy are then given by $\boldsymbol{U} = (U, V, 0) = (-\partial_y\psi, \partial_x\psi, 0)$ and $B = f\partial_z\psi$ (in this chapter we systematically denote flow variables in upper-case). With these assumptions, the linearised non-hydrostatic Boussinesq equations read

$$\left.\begin{aligned} \partial_t\boldsymbol{u} + \nabla\boldsymbol{U}\cdot\boldsymbol{u} + \boldsymbol{U}\cdot\nabla\boldsymbol{u} + f\hat{\boldsymbol{z}}\times\boldsymbol{u} &= -\nabla p + b\hat{\boldsymbol{z}}, \\ \partial_t b + \boldsymbol{u}\cdot\nabla B + \boldsymbol{U}\cdot\nabla b + N^2 w &= 0, \\ \nabla\cdot\boldsymbol{u} &= 0, \end{aligned}\right\} \tag{5-2.1}$$

where $\boldsymbol{u} = (u, v, w)$ denotes the wave velocity, $\nabla = (\partial_x, \partial_y, \partial_z)$ is the full gradient operator, $\hat{\boldsymbol{z}}$ is the vertical unit vector, p is the pressure normalised by a constant reference density, b the buoyancy, f the Coriolis parameter, and N the buoyancy frequency which is assumed to be constant. The equations have further assumed incompressibility, f-plane dynamics, and we neglect dissipative effects. We note that the difference between this system and the one with a barotropic flow is that new terms have appeared due to the buoyancy of the flow B, contributions due to the vertically sheared flow, $\partial_z\boldsymbol{U}w$, and the wave pressure, now not assumed to be hydrostatic, may have a non-trivial vertical structure. This turns out to have a dramatic effect on the resulting dynamics.

It was described in detail in Chapter 2 §2-1 that a key requirement of our analysis is a separation of time scales between the balanced motion and IGWs as estimated by the Rossby number

$$\mathrm{Ro} = U_* K_{h*}/f \ll 1,$$

where $U_* = \langle|\boldsymbol{U}|^2\rangle^{1/2}$ is the average velocity of the background flow and K_{h*} is a typical horizontal inverse flow scale. This ensures that the coupling between IGWs and the background motion is weak.

We assume that while IGW phases vary over the length scale $|\boldsymbol{k}|^{-1}$, where $\boldsymbol{k} = (k_1, k_2, k_3) = (\boldsymbol{k}_h, k_3)$ is the IGW wavevector, the IGW amplitudes vary over a much larger scale $(\varepsilon|\boldsymbol{k}|)^{-1}$, where $\varepsilon \ll 1$. We adopt the scaling $\varepsilon = O(\mathrm{Ro}^2)$, which ensures that transport and scattering affect the wave field at the same order and emerge at leading order of our asymptotic model.

As in Chapter 4, we assume that the typical horizontal and vertical inverse flow scales K_{h*} and K_{v*} are related by $K_{v*} = NK_{h*}/f$. Now though, we relax the assumption that IGWs should be small in length scale relative to the background flow. The only requirement is that the IGW wavenumber $k_h = |\boldsymbol{k}_h|$ remains small enough for $(k_h/K_{h*})\mathrm{Ro} < O(1)$ to hold (see Chapter 2: §2-1 and Figure 2-1 for a more discussion). This assumption then implies that for low frequency waves with $\omega = O(f)$, where

$$\omega(\boldsymbol{k}) = \sqrt{N^2k_h^2 + f^2k_3^2}/|\boldsymbol{k}| \tag{5-2.2}$$

is the IGW dispersion relation, the background flow velocities are small compared with the wave phase speed $c_p = \omega/|\boldsymbol{k}|$ since

$$U_*/c_p = O\big((U_*K_*/\omega)\cdot(k_*/K_*)\big) = O\big(\mathrm{Ro}\cdot(k_*/K_*)\big) < O(1).$$

5-2.2 General formulation

The system (5-2.1) consists of five equations for the variables (u, v, w, b, p), however only three of these variables are prognostic while two may be diagnosed given knowledge of the others. For example we may use the incompressibility constraint to find the vertical velocity as

$$w = -\partial_z^{-1}(\nabla_h \cdot \boldsymbol{u}_h),$$

where $\nabla_h = (\partial_x, \partial_y, 0)$ is the horizontal gradient operator. Likewise, taking the full divergence of the momentum equation in (5-2.1) allows the diagnosed pressure to be written as

$$p = \nabla^{-2}[\partial_z b - f\zeta - \nabla\cdot(\boldsymbol{u}\cdot\nabla\boldsymbol{U} + \boldsymbol{U}\cdot\nabla\boldsymbol{u})], \tag{5-2.3}$$

where $\zeta = \partial_x v - \partial_y u$ is the vertical vorticity. We may incorporate the constraints of the dynamics and describe the wave motion with a reduced set of purely prognostic variables. It is convenient to project the weakly nonlinear dynamics onto a linear

basis, however there is some ambiguity in the choice of variables one can take for the basis. The choice of expansion variables should not affect the resulting linear problem – the dispersion relation and relations between the linear variables, for example. The nonlinear terms can take on complicated representations however, depending on the choice of the basis (Müller *et al.*, 1986). We choose a set of variables presented in Vanneste (2013) that have then been linearised to contain only wave quantities. This reduced set of variables is given by

$$\left.\begin{aligned} \gamma_l &= f\zeta - \nabla_h^2 p_l, \\ \delta &= \partial_x u + \partial_y v, \\ q_l &= f\partial_z b + N^2\zeta. \end{aligned}\right\}$$

Here, γ_l is the linearised ageostrophic vorticity, with $p_l = \nabla^{-2}[\partial_z b - f\zeta]$ a linearised version of the pressure in (5-2.3), δ is the horizontal divergence of the wave velocity, and q_l is the linearised potential vorticity (PV). This results in a relatively simple form for the operator involving the weakly nonlinear interaction terms.

Schematically, the new equations of motion are in the form

$$\left.\begin{aligned} \partial_t\gamma_l + \Omega^2\delta &= \mathcal{N}_{\gamma_l}, \\ \partial_t\delta - \gamma_l &= \mathcal{N}_\delta, \\ \partial_t q_l + 0 &= \mathcal{N}_{q_l}, \end{aligned}\right\} \tag{5-2.4}$$

where we have grouped the nonlinear interaction terms into the $\mathcal{N}$ terms, and we introduce the linear pseudodifferential operator

$$\Omega(\partial_{\boldsymbol{x}}) = [(N^2\nabla_h^2 + f^2\partial_{zz})\nabla^{-2}]^{1/2}.$$

The linear dynamics are given by setting the right hand sides of (5-2.4) to zero. As discussed in Chapter 1 and shown in Appendix A, linear IGW modes have $q_l \equiv 0$ so that the PV plays no role in the IGW energy or dynamics, while the PV-containing vortical mode is prescribed by the random streamfunction ψ. There is therefore no need to retain the variable q_l, and we drop the final equation from (5-2.4).

We group the remaining variables for the wave dynamics into a state vector

$$\boldsymbol{\phi} = \begin{pmatrix} \gamma_l \\ \delta \end{pmatrix}. \tag{5-2.5}$$

From here we can define the operators $\boldsymbol{L}$ and $\boldsymbol{N}$, which group the transformed linear and nonlinear terms of (5-2.1) respectively, such that they satisfy the evolution equation for $\boldsymbol{\phi}$ given by

$$\partial_t \boldsymbol{\phi} + \boldsymbol{L}(\partial_x)\boldsymbol{\phi} + \sqrt{\varepsilon}\boldsymbol{N}(\boldsymbol{x}, \partial_{\boldsymbol{x}}, \sqrt{\varepsilon}t)\boldsymbol{\phi} = 0. \tag{5-2.6}$$

As in Chapter 2, we have included $\sqrt{\varepsilon}$ as a bookkeeping parameter for the weak background flow that we set to unity at the end. Time dependence of $\boldsymbol{N}$ enters via the slow time dependence of the background flow in the streamfunction $\psi(\boldsymbol{x}, \sqrt{\varepsilon}t)$, but we suppress the explicit dependence for the remainder of the chapter. The coefficients of the linear terms could additionally depend on space to give a linear operator of the form $\boldsymbol{L}(\boldsymbol{x}, \partial_{\boldsymbol{x}})$, for example through a spatially varying buoyancy frequency N or Coriolis parameter f, and would lead to a slightly modified kinetic equation as discussed in Chapter 2.

The operator $\boldsymbol{L}$ is written explicitly here as

$$\boldsymbol{L}(\partial_{\boldsymbol{x}}) = \begin{pmatrix} 0 & \Omega^2 \\ -1 & 0 \end{pmatrix}, \tag{5-2.7}$$

and the components of the interaction operator $\boldsymbol{N}(\boldsymbol{x}, \partial_{\boldsymbol{x}})$ can be expressed as (with $\psi_x = \partial_x \psi$ etc.):

$$\begin{aligned}
\boldsymbol{N}_{11}\gamma_l &= (\Omega\nabla)^{-2}\partial_z\Big\{f^2\partial_z\Big([(\psi_x\partial_y - \psi_y\partial_x) - ((\nabla_h^2\psi_x)\partial_y - (\nabla_h^2\psi_y)\partial_x)\nabla_h^{-2}]\gamma_l\Big) \\
&\quad + f^2\nabla_h^2\Big([(\psi_{xz}\partial_y - \psi_{yz}\partial_x)\nabla_h^{-2}]\gamma_l\Big) + N^2\nabla_h^2\Big((\psi_x\partial_y - \psi_y\partial_x)\partial_z^{-1}\gamma_l\Big)\Big\}, \qquad (5\text{-}2.8) \\
\boldsymbol{N}_{12}\,\delta &= \nabla^{-2}(f\partial_z)\Big\{\partial_z\Big([((\nabla_h^2\psi_x)\partial_x + (\nabla_h^2\psi_y)\partial_y)\nabla_h^{-2} + (\nabla_h^2\psi) \\
&\quad - (\psi_{xz}\partial_x + \psi_{yz}\partial_y + \nabla_h^2\psi_z)\partial_z^{-1}]\delta\Big) - \nabla_h^2\Big([(\psi_{xz}\partial_x + \psi_{yz}\partial_y)\nabla_h^{-2} - \psi_{zz}\partial_z^{-1}]\delta\Big)\Big\},
\end{aligned}$$

$$\begin{aligned}
\boldsymbol{N}_{21}\gamma_l &= -2f(\Omega\nabla)^{-2}\partial_{zz}\Big\{[\psi_{yy}\partial_{xx} - 2\psi_{xy}\partial_{xy} + \psi_{xx}\partial_{yy}]\nabla_h^{-2}\gamma_l\Big\}, \\
\boldsymbol{N}_{22}\,\delta &= \nabla^{-2}\Big\{\partial_{zz}\Big([(\psi_x\partial_y - \psi_y\partial_x) + 2((\psi_{xx} - \psi_{yy})\partial_{xy} - \psi_{xy}(\partial_{xx} - \partial_{yy}))\nabla_h^{-2} \\
&\quad - (\psi_{xz}\partial_y - \psi_{yz}\partial_x)\partial_z^{-1}]\delta\Big) + \nabla_h^2\Big([(\psi_x\partial_y - \psi_y\partial_x) + (\psi_{xz}\partial_y - \psi_{yz}\partial_x)\partial_z^{-1}]\delta\Big)\Big\}.
\end{aligned}$$

We have derived a set of equations that are reduced from (5-2.1) to contain only

the prognostic variables governing the evolution of IGWs. We show next how to pass from the equations expressed in the general form (5-2.6) to the kinetic equation, drawing from the theory presented in Chapter 2.

5-3 Kinetic equation for IGW scattering

5-3.1 Derivation of the kinetic equation

The formalism of Chapter 2 allows the scattering cross-section for a given system to be written almost immediately given a few ingredients which we present here. We first find the orthonormal basis of eigenvectors and their eigenvalues for the linearised Boussinesq system.

Operators and eigenvectors

Upon transforming (5-2.6) to wavenumber space, the linear operator $\boldsymbol{L}$ shown in (5-2.7) becomes

$$\boldsymbol{L}(\mathrm{i}\boldsymbol{k}) = \begin{pmatrix} 0 & \omega^2 \\ -1 & 0 \end{pmatrix},$$

with $\omega(\boldsymbol{k})$ the IGW frequency given by (5-2.2). This matrix is known as the dispersion matrix since it defines an eigenvalue equation of the form $\boldsymbol{L}\boldsymbol{b}_\pm = \pm\mathrm{i}\omega\boldsymbol{b}_\pm$, where its eigenvalues give the IGW dispersion relation. Note that in the previous section we dropped the equation for the PV-containing mode which would have had the eigenvalue $\omega_0 = 0$. The eigenvectors of $\boldsymbol{L}$ are given by

$$\boldsymbol{b}_\pm(\boldsymbol{k}) = \frac{|\boldsymbol{k}_h||k_3|}{\sqrt{2}\,|\boldsymbol{k}|} \begin{pmatrix} \pm\mathrm{i}\omega \\ -1 \end{pmatrix}. \tag{5-3.1}$$

As described in Chapter 2, the eigenvectors are orthonormal with respect to a weighted inner-product, that is

$$\langle \boldsymbol{b}_i, \boldsymbol{b}_j \rangle_{\boldsymbol{M}} = \boldsymbol{b}_i^* \boldsymbol{M} \boldsymbol{b}_j = \delta_{ij}, \tag{5-3.2}$$

where the symmetric matrix $\boldsymbol{M}$ is given by

$$\boldsymbol{M}(\boldsymbol{k}) = \frac{|\boldsymbol{k}|^2}{\omega^2|\boldsymbol{k}_h|^2|k_3|^2}\begin{pmatrix} 1 & 0 \\ 0 & \omega^2 \end{pmatrix}. \tag{5-3.3}$$

We recall from Chapter 2 that this matrix and inner-product emerges naturally when writing the energy density of the linear system in terms of the dynamical variables in the form

$$\widehat{\mathcal{E}}(\boldsymbol{k},t) = \tfrac{1}{2}(|\widehat{\boldsymbol{u}}|^2 + |\widehat{b}|^2/N^2) = \tfrac{1}{2}\langle\widehat{\boldsymbol{\phi}},\widehat{\boldsymbol{\phi}}\rangle_{\boldsymbol{M}}.$$

Evaluating the scattering cross-section

Following the prescription of Chapter 2, we take the components in (5-2.8) and Fourier transform according to (2-3.14) so that

$$\boldsymbol{N}(\boldsymbol{x},\partial_{\boldsymbol{x}}) \to \widehat{\boldsymbol{N}}(\boldsymbol{q},\mathrm{i}\boldsymbol{p}) = \widehat{\boldsymbol{U}}(\boldsymbol{q},\mathrm{i}\boldsymbol{p})\widehat{\psi}(\boldsymbol{q}), \tag{5-3.4}$$

where we extract the linear dependence on the streamfunction by introducing the matrix operator $\widehat{\boldsymbol{U}}$. In Chapter 2, §2-3.1 it was assumed that the pseudodifferential operator $\boldsymbol{N}(\boldsymbol{x},\partial_{\boldsymbol{x}})$ should have all derivatives $\partial_{\boldsymbol{x}}$ to the right of its $\boldsymbol{x}$-dependence, which enters solely through $\psi(\boldsymbol{x})$. We see that the components of $\boldsymbol{N}$ given by (5-2.8), however, have derivatives to the left of the streamfunction terms which act both on $\psi(\boldsymbol{x})$ and on the vector $\boldsymbol{\phi}(\boldsymbol{x},t)$. This does not change the result of the kinetic equation derivation in Chapter 2, but extra care must be taken in making the transformation (5-3.4) as it does not transform as straightforwardly as (2-3.2).

In order to keep track of how the derivatives to the left of the $\boldsymbol{x}$-dependence transform, we assume an operator of the form

$$\boldsymbol{N}(\boldsymbol{x},\partial_{\boldsymbol{x}})F(\boldsymbol{x}) = \partial_{\boldsymbol{x}}^{\boldsymbol{\alpha}}\Big[G(\boldsymbol{x})\partial_{\boldsymbol{x}}^{\boldsymbol{\beta}}F(\boldsymbol{x})\Big],$$

where $\boldsymbol{\alpha}$, $\boldsymbol{\beta}$ are multi-indices and G is a spatially dependent function, similarly positioned with respect to the differential operators as ψ is in the equations of motion.

Such an operator now transforms as

$$\begin{aligned}\boldsymbol{N}(\boldsymbol{x},\partial_{\boldsymbol{x}})F(\boldsymbol{x}) &= \partial_{\boldsymbol{x}}^{\boldsymbol{\alpha}}\Big[G(\boldsymbol{x})\partial_{\boldsymbol{x}}^{\boldsymbol{\beta}}F(\boldsymbol{x})\Big]\\ &= \partial_{\boldsymbol{x}}^{\boldsymbol{\alpha}}\left[\int e^{-\mathrm{i}\boldsymbol{x}\cdot\boldsymbol{q}}\widehat{G}(\boldsymbol{q})\mathrm{d}\boldsymbol{q}\,\partial_{\boldsymbol{x}}^{\boldsymbol{\beta}}\int e^{-\mathrm{i}\boldsymbol{x}\cdot\boldsymbol{p}}\widehat{F}(\boldsymbol{p})\mathrm{d}\boldsymbol{p}\right]\\ &= \iint e^{-\mathrm{i}\boldsymbol{x}\cdot(\boldsymbol{q}+\boldsymbol{p})}(-\mathrm{i}(\boldsymbol{q}+\boldsymbol{p}))^{\boldsymbol{\alpha}}(-\mathrm{i}\boldsymbol{p})^{\boldsymbol{\beta}}\widehat{G}(\boldsymbol{q})\widehat{F}(\boldsymbol{p})\mathrm{d}\boldsymbol{q}\mathrm{d}\boldsymbol{p}\\ &= \iint e^{-\mathrm{i}\boldsymbol{x}\cdot(\boldsymbol{q}+\boldsymbol{p})}\widehat{\boldsymbol{N}}(\boldsymbol{q},-\mathrm{i}\boldsymbol{p})\widehat{F}(\boldsymbol{p})\mathrm{d}\boldsymbol{q}\mathrm{d}\boldsymbol{p}.\end{aligned}$$

The penultimate line demonstrates how the derivatives in $\boldsymbol{N}$ acting on products of functions, as indexed by $\boldsymbol{\alpha}$, should transform. The operator $\boldsymbol{N}$ arises in the Chapter 2 derivation in the form $\widehat{\boldsymbol{N}}(\boldsymbol{k}'-\boldsymbol{k},\mathrm{i}\boldsymbol{k}')$ (see (2-3.21)), and so its arguments combine as $(-\mathrm{i}(\boldsymbol{k}'-\boldsymbol{k}-\boldsymbol{k}'))^{\boldsymbol{\alpha}}=(\mathrm{i}\boldsymbol{k})^{\boldsymbol{\alpha}}$.

Following this transformation rule and extracting the dependence on $\widehat{\psi}$ by exploiting the form of (5-3.4), we can explicitly write the components of $\widehat{\boldsymbol{U}}(\boldsymbol{k}'-\boldsymbol{k},\mathrm{i}\boldsymbol{k}')$ in the form required for deriving the cross-section as

$$\begin{aligned}\widehat{U}_{11} &= \frac{\hat{\boldsymbol{k}}_3\cdot\boldsymbol{k}_h'\times\boldsymbol{k}_h}{|\boldsymbol{k}_h'|^2}\frac{|k_3|^2}{|\boldsymbol{k}|^2}\Big[\frac{f^2}{\omega^2}(2\boldsymbol{k}_h\cdot\boldsymbol{k}_h'-|\boldsymbol{k}_h||\boldsymbol{k}_h'|\mathrm{sgn}\,(k_3k_3'))+\frac{N^2}{\omega^2}\frac{|\boldsymbol{k}_h|^2|\boldsymbol{k}_h'|^2}{k_3k_3'}\Big],\\ \widehat{U}_{22} &= \frac{\hat{\boldsymbol{k}}_3\cdot\boldsymbol{k}_h'\times\boldsymbol{k}_h}{|\boldsymbol{k}_h'|^2}\frac{|k_3|^2}{|\boldsymbol{k}|^2}\Big[2\boldsymbol{k}_h\cdot\boldsymbol{k}_h'-|\boldsymbol{k}_h||\boldsymbol{k}_h'|\mathrm{sgn}\,(k_3k_3')+\frac{|\boldsymbol{k}_h|^2|\boldsymbol{k}_h'|^2}{k_3k_3'}\Big],\\ \widehat{U}_{12} &= \frac{f}{|\boldsymbol{k}_h'|^2}\frac{|k_3|^2}{|\boldsymbol{k}|^2}\Big[(k_3'-k_3)^2\frac{|\boldsymbol{k}_h'||\boldsymbol{k}_h|}{|k_3'||k_3|}-|\boldsymbol{k}_h'-\boldsymbol{k}_h|^2\Big]\boldsymbol{k}_h'\cdot\boldsymbol{k}_h,\\ \widehat{U}_{21} &= 2\frac{f}{\omega^2}\frac{|k_3|^2}{|\boldsymbol{k}|^2}\frac{|\boldsymbol{k}_h'\times\boldsymbol{k}_h|^2}{|\boldsymbol{k}_h'|^2},\end{aligned}\tag{5-3.5}$$

where we have used $\Omega(\mathrm{i}\boldsymbol{k})=\omega(\boldsymbol{k})$.

In order to finally arrive at an explicit representation of the the cross-section we follow the intermediate steps (2-3.22)–(2-3.25) in Chapter 2 which requires the calculation of

$$\langle\boldsymbol{b}_\pm(\boldsymbol{k}),\widehat{\boldsymbol{U}}(\boldsymbol{k}'-\boldsymbol{k},\mathrm{i}\boldsymbol{k}')\boldsymbol{b}_\pm(\boldsymbol{k}')\rangle_{\boldsymbol{M}}=:\alpha(\boldsymbol{k},\boldsymbol{k}')\pm\mathrm{i}\beta(\boldsymbol{k},\boldsymbol{k}'),\tag{5-3.6}$$

with the inner product as defined in (5-3.2). As the derivation in Chapter 2 shows, scattering is constrained to a resonant surface where $\omega(\boldsymbol{k})=\omega(\boldsymbol{k}')=\pm\omega$, and so we

may write

$$\langle \boldsymbol{b}_{\pm}, \widehat{\boldsymbol{U}}\boldsymbol{b}_{\pm}\rangle_{\boldsymbol{M}} = \frac{1}{2\omega}\frac{|\boldsymbol{k}||\boldsymbol{k}_h'||k_3'|}{|\boldsymbol{k}'||\boldsymbol{k}_h||k_3|}[\omega(\widehat{U}_{11}+\widehat{U}_{22}) \pm \mathrm{i}(\widehat{U}_{12}-\omega^2\widehat{U}_{21})]. \tag{5-3.7}$$

We can read off the functions $\alpha(\boldsymbol{k},\boldsymbol{k}')$ and $\beta(\boldsymbol{k},\boldsymbol{k}')$ by comparing (5-3.6) with (5-3.7). Evaluating this with the components listed in (5-3.5) confirms that the symmetries $\alpha(\boldsymbol{k},\boldsymbol{k}') = -\alpha(\boldsymbol{k}',\boldsymbol{k})$ and $\beta(\boldsymbol{k},\boldsymbol{k}') = \beta(\boldsymbol{k}',\boldsymbol{k})$ hold. As discussed in Chapter 2 this is a sufficient condition for energy conservation, and for evaluating the cross-section simply, as in (2-3.25), in the form

$$\sigma(\boldsymbol{k},\boldsymbol{k}') := 2\pi\big(\alpha^2(\boldsymbol{k},\boldsymbol{k}')+\beta^2(\boldsymbol{k},\boldsymbol{k}')\big)\widehat{R}(\boldsymbol{k}'-\boldsymbol{k})\delta\big(\omega(\boldsymbol{k})-\omega(\boldsymbol{k}')\big). \tag{5-3.8}$$

The function $\widehat{R}(\boldsymbol{k})$ is the power spectrum of the flow (see (2-3.16)) which we relate to the energy spectrum of the flow by

$$\widehat{R}(\boldsymbol{k}) = \frac{\widehat{E}(\boldsymbol{k})}{|\boldsymbol{k}_h|^2}.$$

Having substituted and simplified the relevant terms into (5-3.8), we obtain the differential scattering cross-section explicitly as

$$\begin{aligned}\sigma(\boldsymbol{k},\boldsymbol{k}') =& \frac{\pi|k_3|^2|k_3'|^2}{2\omega^4|\boldsymbol{k}|^2|\boldsymbol{k}'|^2|\boldsymbol{k_h}|^2|\boldsymbol{k_h'}|^2}\Bigg[|\boldsymbol{k}_h'\times\boldsymbol{k}_h|^2\big[(N^2+\omega^2)\frac{|\boldsymbol{k_h}|^2|\boldsymbol{k_h'}|^2}{|k_3||k_3'|}\mathrm{sgn}\,(k_3k_3') \\ &+(f^2+\omega^2)(2\boldsymbol{k}_h\cdot\boldsymbol{k}_h'-|\boldsymbol{k_h}||\boldsymbol{k_h'}|\mathrm{sgn}\,(k_3k_3'))\big]^2+f^2\omega^2\Big(2|\boldsymbol{k}_h'\times\boldsymbol{k}_h|^2 \\ &+\big[|\boldsymbol{k}_h'-\boldsymbol{k}_h|^2-(k_3'-k_3)^2\frac{|\boldsymbol{k_h'}||\boldsymbol{k_h}|}{|k_3'||k_3|}\big]\boldsymbol{k}_h'\cdot\boldsymbol{k}_h\Big)^2\Bigg]\frac{\widehat{E}(\boldsymbol{k}'-\boldsymbol{k})}{|\boldsymbol{k}_h'-\boldsymbol{k}_h|^2}\delta(\omega(\boldsymbol{k}')-\omega(\boldsymbol{k})).\end{aligned} \tag{5-3.9}$$

This cross-section is the main object of interest and main result of this thesis. With it we are able to quantitatively investigate and characterise the catalytic interactions of IGWs with geostrophic turbulence, with no assumption of spatial-scale separation and with non-trivial vertical dynamics. With this cross-section, the kinetic equation reads

$$\partial_t a(\boldsymbol{x},\boldsymbol{k},t)+\nabla_{\boldsymbol{k}}\omega\cdot\nabla_{\boldsymbol{x}}a = \int_{\mathbb{R}^3}\sigma(\boldsymbol{k},\boldsymbol{k}')a(\boldsymbol{x},\boldsymbol{k}',t)\mathrm{d}\boldsymbol{k}'-\Sigma(\boldsymbol{k})a(\boldsymbol{x},\boldsymbol{k},t). \tag{5-3.10}$$

We would subtract $\nabla_{\boldsymbol{x}}\omega \cdot \nabla_{\boldsymbol{k}} a$ from the left side of the equation if the operator $\boldsymbol{L}(\partial_{\boldsymbol{x}})$, and consequently the dispersion relation, had a spatial dependence of $\boldsymbol{L}(\boldsymbol{x}, \partial_{\boldsymbol{x}})$. We note that $\sigma(\boldsymbol{k}, \boldsymbol{k}')$ is real, positive, and symmetric with respect to swapping the wavevectors $\boldsymbol{k}$ and $\boldsymbol{k}'$.

We can establish a connection with the kinetic equation of Chapter 3 by considering purely horizontal transfers, with no change in the vertical dimension. We consider $k_3 = k_3'$ in (5-3.9), which together with the resonance constraint $\omega(\boldsymbol{k}) = \omega(\boldsymbol{k}')$ implies that $|\boldsymbol{k}_h| = |\boldsymbol{k}_h'|$ and $|\boldsymbol{k}| = |\boldsymbol{k}'|$. The model in Chapter 3 applies to hydrostatic waves such that the horizontal scales are much larger than the vertical, or equivalently that $|\boldsymbol{k}| \approx |k_3|$ (Olbers *et al.*, 2012). In such a limit we obtain

$$\sigma(\boldsymbol{k}, \boldsymbol{k}') = \frac{2\pi}{\omega^4 |\boldsymbol{k_h}|^4} \Bigg[|\boldsymbol{k}_h' \times \boldsymbol{k}_h|^2 \big[(\omega^2 + f^2)\boldsymbol{k}_h \cdot \boldsymbol{k}_h' - f^2 |\boldsymbol{k}_h|^2\big]^2 \\ + f^2\omega^2 \Big(|\boldsymbol{k}_h' \times \boldsymbol{k}_h|^2 + \boldsymbol{k}_h \cdot \boldsymbol{k}_h' \big(|\boldsymbol{k}_h|^2 - \boldsymbol{k}_h \cdot \boldsymbol{k}_h' \big) \Big)^2 \Bigg] \frac{\widehat{E}(\boldsymbol{k}' - \boldsymbol{k})}{|\boldsymbol{k}_h' - \boldsymbol{k}_h|^2} \delta(\omega(\boldsymbol{k}') - \omega(\boldsymbol{k})),$$

which is identical to the cross-section (3-2.16) derived for the rotating shallow water system in Chapter 3, where the vertical modes correspond to a superposition of upward- and downward-propagating waves of equal vertical wavenumber.

5-3.2 Scattering on the resonant double cone

The delta-function appearing in (5-3.9) indicates that energy transfers are restricted to a resonant surface of constant frequency. For IGWs the surface is a double cone, with the surface of each cone known as a *nappe*. This surface is observed by transforming to spherical coordinates which shows that the wave frequency depends on a single parameter – the angle the wavevector makes with the vertical, θ. We employ the following coordinate system (see Figure 5-1):

$$\boldsymbol{k} = k \begin{pmatrix} \sin\theta\cos\varphi \\ \sin\theta\sin\varphi \\ \cos\theta \end{pmatrix}, \quad \boldsymbol{k}' = k' \begin{pmatrix} \sin\theta'\cos(\varphi + \varphi') \\ \sin\theta'\sin(\varphi + \varphi') \\ \cos\theta' \end{pmatrix}. \tag{5-3.11}$$

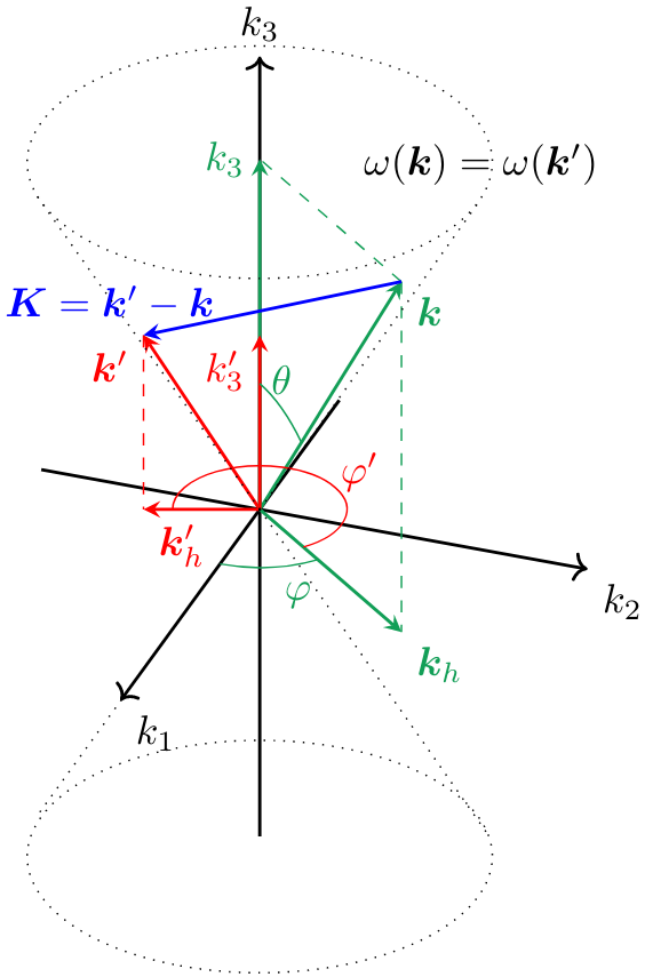

Figure 5-1. Illustration of the coordinate system described by (5-3.11) for transfers on the cone defined by $\omega(\boldsymbol{k}) = \text{constant}$. Note that the angle of the cone θ determines the wave frequency. Low frequency waves, such as near-inertial waves with $\omega \approx f$, exist on a very narrow cone with $\theta \ll 1$.

In these coordinates the dispersion relation (5-2.2) is written

$$\omega(\theta) = \sqrt{N^2 \sin^2\theta + f^2 \cos^2\theta},$$

such that the constant frequency constraint $\omega(\theta') = \omega(\theta)$ implies the coordinate $\theta' = \{\theta,\, \pi - \theta\}$, where

$$\theta = \sin^{-1}\sqrt{\frac{\omega^2 - f^2}{N^2 - f^2}}$$

is a constant.

The delta function in (5-3.9) can be expressed in the new coordinates (5-3.11) as

$$\delta(\omega(\boldsymbol{k}') - \omega(\boldsymbol{k})) = \frac{2\,\omega(\theta')}{|\sin(2\theta')|(N^2 - f^2)}\Big[\delta(\theta' - \theta) + \delta(\theta' - (\pi - \theta))\Big].$$

We define a pair of cross-sections by

$$\int_0^\pi \sigma \sin\theta' \mathrm{d}\theta' = \sum_{i=\pm} \sigma_i(k, k', \varphi, \varphi', \theta), \tag{5-3.12}$$

with σ_+ quantifying the rate of scattering for waves with $\theta' = \theta$ (transfers remaining on one nappe of the double cone), and σ_- for waves scattering to $\theta' = \pi - \theta$ (transfers from one nappe across to the other) which corresponds to a reflection of upward- to downward-propagating waves or vice-versa. We can define a total cross-section for each type of transfer by

$$\Sigma_\pm(k, \varphi, \theta) = \int_0^\infty \int_{-\pi}^\pi \sigma_\pm(k, k', \varphi, \varphi', \theta) k'^2 \mathrm{d}\varphi' \mathrm{d}k', \tag{5-3.13}$$

with the usual total cross-section for the system then given by $\Sigma(k, \varphi, \theta) = \Sigma_+ + \Sigma_-$.

In order to explicitly represent the cross-sections (5-3.12) in the new coordinates (5-3.11), it is useful to note the relations appearing in (5-3.9) become

$$\begin{aligned}
|\boldsymbol{k}_h| = k\sin\theta, \quad k_3 = k\cos\theta,\\
\boldsymbol{k}_h \cdot \boldsymbol{k}'_h = kk' \sin^2\theta\cos\varphi',\\
\hat{\boldsymbol{k}}_3 \cdot \boldsymbol{k}_h \times \boldsymbol{k}'_h = kk' \sin^2\theta \sin\varphi',\\
|\boldsymbol{k}'_h - \boldsymbol{k}_h| = \sin\theta\sqrt{k^2 + k'^2 - 2k'k\cos\varphi'}.
\end{aligned}$$

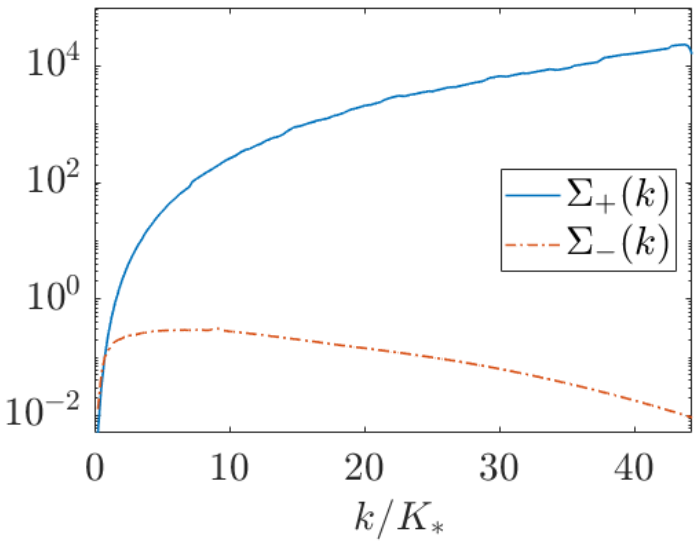

Figure 5-2. Total cross-sections for same-nappe ($\Sigma_+(k)$) and across-nappe ($\Sigma_-(k)$) transfers as given by (5-3.13), shown here for $\omega = 3f$, $N/f = 32$, and Rossby number $\mathrm{Ro} = 0.099$. (Arbitrary units.) The energy spectrum is as described in §4-3. Note that $\Sigma_- \to 0$ in the WKB limit of large k/K_*, consistent with the results of the previous chapter that reflections in z are suppressed in the short-wave limit.

Substituting these into (5-3.9) and integrating according to (5-3.12) leads to a reduced (defined on a lower-dimension space) pair of cross-sections of the form

$$\sigma_{\pm}(k,k',\varphi,\varphi',\theta) = \frac{\pi k^2 k'^2}{16\omega^3}\frac{|\sin(2\theta)|^3}{\sin\theta(N^2-f^2)}\Big\{4f^2\omega^2\Big[\cos\varphi'(\cos\varphi'\mp 1)-\sin^2\varphi'\Big]^2 + \sin^2\varphi'\Big[(\omega^2+f^2)(2\cos\varphi'\mp 1)\pm(N^2+\omega^2)\tan^2\theta\Big]^2\Big\}\frac{\widehat{E}(\boldsymbol{k}'-\boldsymbol{k})}{(k^2+k'^2-2k'k\cos\varphi')}, \tag{5-3.14}$$

where it is understood that $\boldsymbol{k}'$ in the argument of the spectrum $\widehat{E}(\boldsymbol{k}'-\boldsymbol{k})$ is restricted to represent the set of wavevectors on the same nappe as $\boldsymbol{k}$ for σ_+ or across to the other nappe of the double cone for σ_-.

It is important to note that the dependence of the cross-section on the azimuthal angle φ is solely through the spectrum of the turbulent background flow, that is through $\widehat{E}$. If horizontally isotropic flows are considered then the cross-section has no φ-dependence. It is then possible to simplify the kinetic equation further by Fourier transforming in the azimuthal variable φ as in Chapter 3.

We show an example of the cross-sections σ_+ and σ_- in Figure 5-3 corresponding to the scattering of a wave with a fixed intial wavenumber $k = k_*$, where the energy spectrum in (5-3.14) was obtained from an average of horizontally isotropic geostrophic turbulence simulations as described in §4-3. The σ_+ cross-sections appear to show greater concentration in the φ'-direction than the k'-direction for fixed $k = k_*$. This suggests that waves redistribute azimuthally much more rapidly than they cascade to different lengthscales. We do not study or compare the rate of azimuthal scattering in this thesis, but simulations performed of the Boussinesq equations showed a rapid horizontal isotropisation of IGWs propagating in horizontally isotropic geostrophic turbulence on a faster timescale than the scale cascades, consistent with such an interpretation of Figure 5-3. Note that the relative magnitude of Σ_+ and Σ_-, as seen in Figure 5-2, gives a clearer view of the rates of reflections (transfers between nappes) than by viewing the magnitudes of Figure 5-3, since it is the integrated value that is significant. Figure 5-2 shows that reflections are markedly suppressed for waves that are shorter than the background flow by a factor of 5 or more, consistent with the WKB view that reflection is negligible for short IGWs.

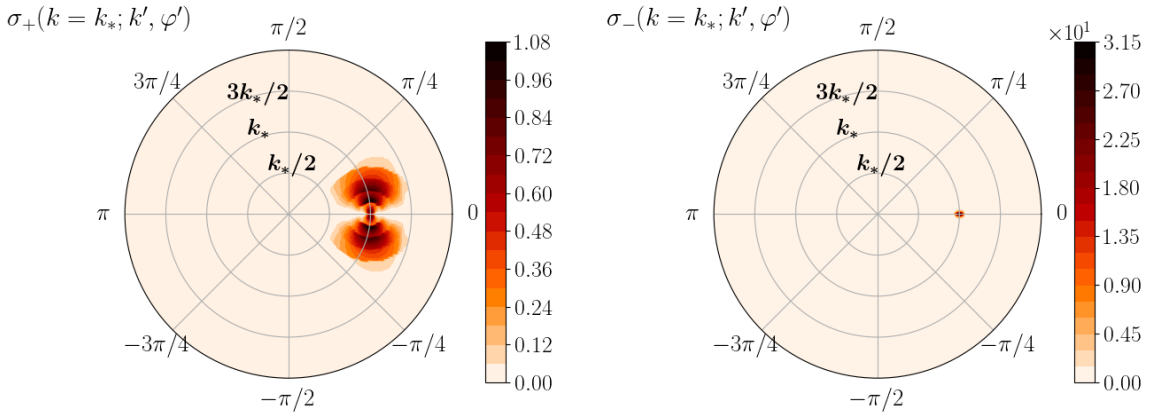

(a) $\omega = 3f$, $\mathrm{Ro} = 0.099$, $N/f = 32$, $k_*/K_* \simeq 1$ (scattering regime).

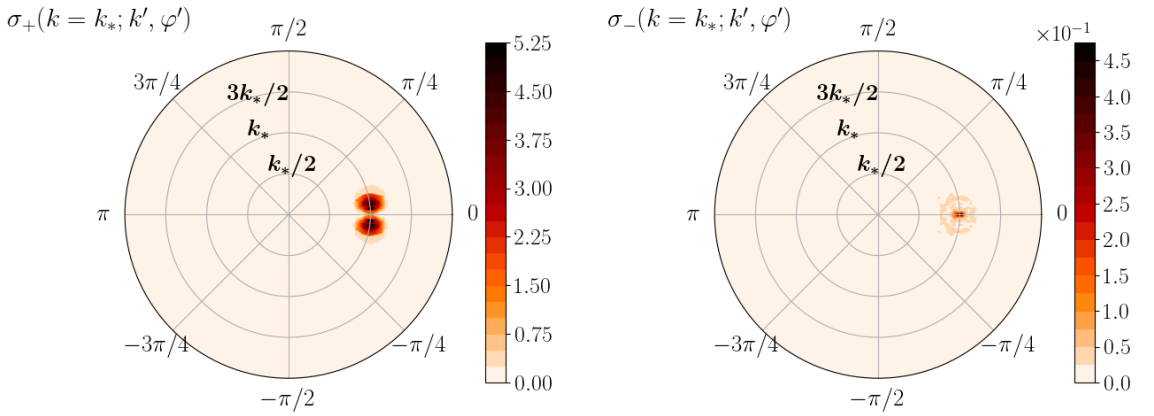

(b) $\omega = 3f$, $\mathrm{Ro} = 0.099$, $N/f = 32$, $k_*/K_* \simeq 4$ (WKB regime).

Figure 5-3. Scattering cross-sections $\sigma_\pm$ as in (5-3.14) for the ranges $k' \in [0, 2k_*]$ and $\varphi' \in (-\pi, \pi)$. This function dictates how IGW energy initially at $k' = k_*$, $\varphi' = 0$ will redistribute – the greater the magnitude of $\sigma_\pm$, the greater the rate at which energy transfers will occur. These figures demonstrate that the greatest concentration of $\sigma_\pm$ is found for small departures in the φ' direction rather than for scale cascades in k' (with $\varphi' = 0$). This is consistent with the observation in simulations that isotropisation occurs at a greater rate than scale cascades. We have chosen a range of parameters to demonstrate that the process is fairly robust in preserving that ordering, but the magnitudes of $\sigma_\pm$ (and so the rate of scattering) may vary significantly.

This figure differs from Figure 3-1 because the flow scale here is fixed, whereas Figure 3-1 displayed σ' as a function of the flow scale κ. Furthermore there was no vertical scattering to consider in the barotropic case, so there was no σ_- counterpart to quantify the rate of reflections for wave scattering in the vertical.

5-3.3 Kinetic equation in spherical coordinates

To take advantage of the geometry of the resonant transfers it is convenient to write a version of the kinetic equation for the energy density on the surface of the double cone, rather than for the density in the full three-dimensions of wavenumber space. We partition the energy density by the nappe that it occupies, equivalently into upwards- and downwards-propagating IGWs, by defining

$$b^+(\boldsymbol{x}, k, \varphi, \theta, t) := b(\boldsymbol{x}, k, \varphi, \theta, t)_{|\theta\in[0,\pi/2]},$$
$$b^-(\boldsymbol{x}, k, \varphi, \theta, t) := b(\boldsymbol{x}, k, \varphi, \theta, t)_{|\theta\in(\pi/2,\pi]},$$

where we have introduced the variable $b := \sin\theta k^2 a(\boldsymbol{x}, k, \varphi, \theta, t)$. It is also convenient to formulate the kinetic equation in terms of a vector-valued phase-space energy density

$$\boldsymbol{b}(\boldsymbol{x}, k, \varphi, \theta, t) := \begin{pmatrix} b^+ \\ b^- \end{pmatrix},$$

and a matrix-valued cross-section

$$\underline{\underline{\sigma}} := \begin{pmatrix} \sigma_+ & \sigma_- \\ \sigma_- & \sigma_+ \end{pmatrix}$$

which has its components defined by (5-3.14). We can then express the kinetic equation (5-3.10) in the spherical coordinate system as

$$\partial_t \boldsymbol{b} + \nabla_{\boldsymbol{k}}\omega \cdot \nabla_{\boldsymbol{x}}\boldsymbol{b} = k^2 \iint \underline{\underline{\sigma}}(k, k', \varphi, \varphi', \theta)\, \boldsymbol{b}(\boldsymbol{x}, k', \varphi - \varphi', \theta, t)\mathrm{d}k'\mathrm{d}\varphi' - \Sigma(k, \varphi, \theta)\, \boldsymbol{b}(\boldsymbol{x}, k, \varphi, \theta, t). \quad (5\text{-}3.15)$$

This has the advantage of being defined on a lower dimension subset of the phase-space, with θ constant, and results in one fewer integral to compute for the scattering terms. Further simplifications are possible with horizontally isotropic turbulence where the φ-dependence drops out of the cross-section.

5-4 Properties of the kinetic equation

Some of the important properties of linear IGW scattering contained in the kinetic equations (5-3.10) and (5-3.15) are presented here.

5-4.1 Conservation of energy

As described in Chapter 2 §3, provided the scattering cross-section has the reversibility symmetry $\sigma(\boldsymbol{k}, \boldsymbol{k}') = \sigma(\boldsymbol{k}', \boldsymbol{k})$ then the leading-order energy density given by

$$\mathcal{E}_0(\boldsymbol{x}, t) = \frac{1}{2} \int_{\mathbb{R}^3} a(\boldsymbol{x}, \boldsymbol{k}, t) \mathrm{d}\boldsymbol{k}$$

obeys a continuity equation of the form

$$\partial_t \mathcal{E}_0 + \nabla_{\boldsymbol{x}} \cdot \boldsymbol{\mathcal{F}}_0 = 0,$$

where the leading-order energy flux is given by

$$\boldsymbol{\mathcal{F}}_0(\boldsymbol{x}, t) = \frac{1}{2} \int_{\mathbb{R}^3} [\nabla_{\boldsymbol{k}} \omega(\boldsymbol{k})] a(\boldsymbol{x}, \boldsymbol{k}, t) \mathrm{d}\boldsymbol{k}.$$

The total leading-order energy,

$$E = \frac{1}{2} \iint a(\boldsymbol{x}, \boldsymbol{k}, t) \mathrm{d}\boldsymbol{k} \mathrm{d}\boldsymbol{x},$$

is then also constant. The wave action $\mathcal{A} = E/\omega$ is usually found to be the conserved quantity in wave–mean flow interacting systems (e.g. Salmon (1998); Olbers *et al.* (2012)), but here the energy is conserved as it differs from the action by only a small amount of order Ro.

5-4.2 Equilibration of energy

We can define a function to represent the difference of the energy densities on the two nappes of the double cone, and show that this difference vanishes in time, implying that the energy must equilibrate between the nappes. Physically this corresponds to an energy equipartition between upward and downward propagating waves. To see

this, we define $\delta(k,\varphi,t) := b^+ - b^-$, and use (5-3.15):

$$\begin{aligned}
&\frac{\partial}{\partial t}\iint \delta(k,\varphi,t)\mathrm{d}k\mathrm{d}\varphi \\
&\quad= \iiiint k^2\big[\sigma_+(k,k',\varphi,\varphi') - \sigma_-(k,k',\varphi,\varphi')\big]\delta(k',\varphi-\varphi',t)\mathrm{d}k\mathrm{d}k'\mathrm{d}\varphi\mathrm{d}\varphi' \\
&\qquad- \iint\left(\iint k'^2\big[\sigma_+(k,k',\varphi,\varphi') + \sigma_-(k,k',\varphi,\varphi')\big]\mathrm{d}k'\mathrm{d}\varphi'\right)\delta(k,\varphi,t)\mathrm{d}k\mathrm{d}\varphi \\
&\quad= \iiiint k'^2\big[\sigma_+(k',k,\varphi-\varphi',\varphi') - \sigma_-(k',k,\varphi-\varphi',\varphi')\big]\delta(k,\varphi,t)\mathrm{d}k\mathrm{d}k'\mathrm{d}\varphi\mathrm{d}\varphi' \\
&\qquad- \iiiint k'^2\big[\sigma_+(k,k',\varphi,\varphi') + \sigma_-(k,k',\varphi,\varphi')\big]\,\delta(k,\varphi,t)\mathrm{d}k'\mathrm{d}\varphi'\mathrm{d}k\mathrm{d}\varphi \\
&\quad= -2\iint \Sigma_-(k,\varphi)\delta(k,\varphi,t)\mathrm{d}k\mathrm{d}\varphi, \qquad \text{(5-4.1)}
\end{aligned}$$

having used the evenness of $\sigma_\pm$ in φ', and the reversibility symmetry $\sigma'_\pm(k,k',\varphi,\varphi') = \sigma'_\pm(k',k,\varphi+\varphi',-\varphi')$ to reach the final step. This result shows that the function δ decays in time at a rate controlled by the cross-section Σ_-. The function Σ_- is a measure of the coupling between upward- and downward-propagating waves, and if it were identically zero there would be no reflections of one type to the other. It is clear that the reflections are necessary to distribute energy over both nappes of the double cone.

It is possible to obtain an upper-bound on the rate of decay to equilibrium using Hölder's inequality, which states

$$\|fg\|_1 \le \|f\|_p\|g\|_q \quad \text{such that} \quad \frac{1}{p}+\frac{1}{q}=1,$$

where $\|\cdot\|_p$ is the L^p norm (e.g. Wheeden and Zygmund, 2015). Taking $p=1$ and $q=\infty$ and applying Hölder's inequality to (5-4.1) gives

$$\partial_t\|\delta\|_1 = -2\|\Sigma_-\delta\|_1 \ge -2\|\Sigma_-\|_\infty\|\delta\|_1,$$

where $\|\Sigma_-\|_\infty = \max_{k,\varphi}\Sigma_-(k,\varphi)$. Integrating this inequality leads to the bound

$$\Delta(t) \ge \Delta(0)\exp(-2\|\Sigma_-\|_\infty t),$$

with the function $\Delta := \|\delta\|_1 = \iint |\delta| \mathrm{d}k\mathrm{d}\varphi$ representing the total energy difference between the two nappes of the double cone. We see that $\|\Sigma_-\|_\infty$ can be used as a reference for how rapidly the IGW distribution achieves parity between upward- and downward-propagating waves, so we could assess which parameters might be important for inhibiting or enhancing the reflections. The function $\Delta(t)$ obtained from simulations of the kinetic equation and Boussinesq equations is presented in Figure 5-11 for a selection of different parameters.

5-4.3 H-theorem

Following Boltzmann (Villani, 2008), we can define a function

$$H(t) := \iint a \ln a \, \mathrm{d}\boldsymbol{k}\mathrm{d}\boldsymbol{x},$$

which is known simply as the H-function. It is related to the more familiar entropy S, which we prefer to demonstrate the so-called H-theorem in terms of, via $S(t) = -H(t)$.

Assuming spatial homogeneity for simplicity so that we have just $a(\boldsymbol{k}, t)$ and can avoid integrals over $\boldsymbol{x}$ in all the following steps, we find

$$\begin{aligned}\frac{\mathrm{d}S}{\mathrm{d}t} &= -\int \partial_t a(\ln a + 1)\mathrm{d}\boldsymbol{k} \\ &= -\int \partial_t a \ln a \mathrm{d}\boldsymbol{k},\end{aligned}$$

since conservation of energy gives $\int \partial_t a \mathrm{d}\boldsymbol{k} = 0$. Thus, using the kinetic equation in the Cartesian form of (5-3.10) we see

$$\begin{aligned}\frac{\mathrm{d}S}{\mathrm{d}t} &= \iint \sigma(\boldsymbol{k}, \boldsymbol{k}')\big(a(\boldsymbol{k}) - a(\boldsymbol{k}')\big) \ln a(\boldsymbol{k}) \mathrm{d}\boldsymbol{k}\mathrm{d}\boldsymbol{k}' \\ &= \iint \sigma(\boldsymbol{k}, \boldsymbol{k}')\big(a(\boldsymbol{k}') - a(\boldsymbol{k})\big) \ln a(\boldsymbol{k}') \mathrm{d}\boldsymbol{k}'\mathrm{d}\boldsymbol{k} \\ &= \frac{1}{2}\iint \sigma(\boldsymbol{k}, \boldsymbol{k}')\big(a(\boldsymbol{k}) - a(\boldsymbol{k}')\big) \ln \frac{a(\boldsymbol{k})}{a(\boldsymbol{k}')} \mathrm{d}\boldsymbol{k}\mathrm{d}\boldsymbol{k}' \geq 0,\end{aligned}$$

having used $\sigma(\boldsymbol{k}, \boldsymbol{k}') = \sigma(\boldsymbol{k}', \boldsymbol{k}) \geq 0$, and that $(x - y)\ln(x/y) \geq 0$ for any $x, y \in \mathbb{R}^+$. Therefore we see that the entropy of the system increases, and is at a maximum for the stationary solution of the kinetic equation where $\partial_t a = 0$.

Famously, the H-theorem is result that points to a time-irreversible spreading of the distribution of $a(\boldsymbol{k}, t)$ in $\boldsymbol{k}$-space, despite the time-reversible dynamics governing its evolution (a phenomenon described as Loschmidt's paradox (Villani, 2008)). In this case the theorem supports the picture that energy density in phase-space should be spread out by scattering, forbidding the energy density from coming together to form a Dirac distribution concentrated at a particular point. The nature of the interactions described by the kinetic equation is to smooth and spread energy across the double cone, including cascades of energy to smaller scales. We note that no entropy maximum can be achieved for IGWs as the double cone is a non-compact surface, and so the system remains out of equilibrium for all time.

5-4.4 Isotropisation of wave fields

We exploit the convolution structure and linearity in (5-3.15) that emerges when the cross-section (5-3.14) is independent of the azimuthal variable, φ, by Fourier transforming both sides to give

$$\frac{\partial \widehat{\boldsymbol{b}}_n}{\partial t} = 2\pi k^2 \int_0^\infty \underline{\underline{\widehat{\sigma}}}_n(k, k')\, \widehat{\boldsymbol{b}}_n(k', t)\mathrm{d}k' - \Sigma(k)\, \widehat{\boldsymbol{b}}_n(k, t), \tag{5-4.2}$$

where the Fourier transform is given by

$$\widehat{\boldsymbol{b}}_n(t) = \frac{1}{2\pi} \int_{-\pi}^{\pi} \mathrm{e}^{\mathrm{i}n\varphi} \boldsymbol{b}(\varphi, t)\, \mathrm{d}\varphi$$

such that $\widehat{\boldsymbol{b}}_0$ simply represents the φ-averaged horizontally isotropic energy spectrum. This is possible when the background flow is horizontally isotropic, as its energy spectrum $\widehat{E}$ is the only place dependence on φ appears in the cross-section $\sigma(\boldsymbol{k}, \boldsymbol{k}')$.

In contrast with the analysis of barotropic flows explored in Chapter 3, where it was possible to separate the vertical dynamics from the governing equations, it is not possible to diagonalise the scattering operator corresponding to the right hand side of (5-4.2), because there is the integral over k' remaining. This reflects the ability of waves to scatter not just into different directions, but also to different lengthscales due to vertical shear by the flow. Nevertheless we can show that ultimately the wavefield isotropises (horizontally) due to interactions with a horizontally isotropic flow.

Integrating (5-4.2) over k and summing the contributions from both nappes of the

double cone, we define $\widehat{B}_n := \widehat{b_+}_n + \widehat{b_-}_n$ to obtain

$$\frac{\mathrm{d}}{\mathrm{d}t}\int_0^\infty \widehat{B}_n(k,t)\mathrm{d}k = -\int_0^\infty \big(\Sigma(k) - \Lambda_n(k)\big)\widehat{B}_n(k,t)\mathrm{d}k, \tag{5-4.3}$$

where we define

$$\Lambda_n(k) = 2\pi\int_0^\infty (\widehat{\sigma_+}_n + \widehat{\sigma_-}_n)k'^2\mathrm{d}k'. \tag{5-4.4}$$

From (5-4.4), and the properties of the Fourier transform, we have

$$\Lambda_0(k) = \Sigma(k) \quad \text{and} \quad |\Lambda_{n\geq 1}(k)| < \Lambda_0(k).$$

Thus the scattering term on the right-hand side of (5-4.3) vanishes for $n = 0$ and is negative for $n \geq 1$, so that all amplitudes $\widehat{B}_{n\geq 1}$ decay leaving a final state where the IGW wavefield is horizontally isotropic (energy in $n = 0$ mode only) for arbitrary initial conditions.

5-4.5 Diffusion limit of the kinetic equation

Scattering in the WKB regime, also known as the diffusion or short-wave regime, is a process consisting of energy transfers that are localised in wavenumber space. Waves are scattered by a small amount from $\boldsymbol{k}$ to a nearby wavevector $\boldsymbol{k}' = \boldsymbol{k} + \epsilon\boldsymbol{K}$, with $\boldsymbol{K}$ a large scale flow wavevector, to make up a triad $(\boldsymbol{k}, \boldsymbol{K}, \boldsymbol{k}')$ (cf. McComas and Bretherton (1977) Figure 1a). We include $\epsilon \ll 1$ as a bookkeeping parameter indicating the ratio of typical IGW and background flow length scales such that $K_*/k_* = O(\epsilon)$, as in the WKB regime. Note that this is not the same small parameter as $\varepsilon = \mathrm{Ro}^2$ which measures the separation of time scales between the IGWs and geostrophic background flow.

In this regime we describe in Appendix D how the scattering cross-section given by (5-3.9) reduces to a simple form given by

$$\sigma_{\mathrm{WKB}}(\boldsymbol{k}, \boldsymbol{k} + \epsilon\boldsymbol{K}) = 2\pi\epsilon^{-3}|\boldsymbol{k}_h \times \boldsymbol{K}_h|^2\widehat{R}_\epsilon(\boldsymbol{K})\delta\big(\boldsymbol{K}\cdot\boldsymbol{c}_g\big), \tag{5-4.5}$$

where $\boldsymbol{c}_g = \nabla_{\boldsymbol{k}}\omega$ is the IGW group velocity, and the notation $\widehat{R}_\epsilon$ indicates that the power spectrum – similarly, the energy spectrum – of the background flow is localised

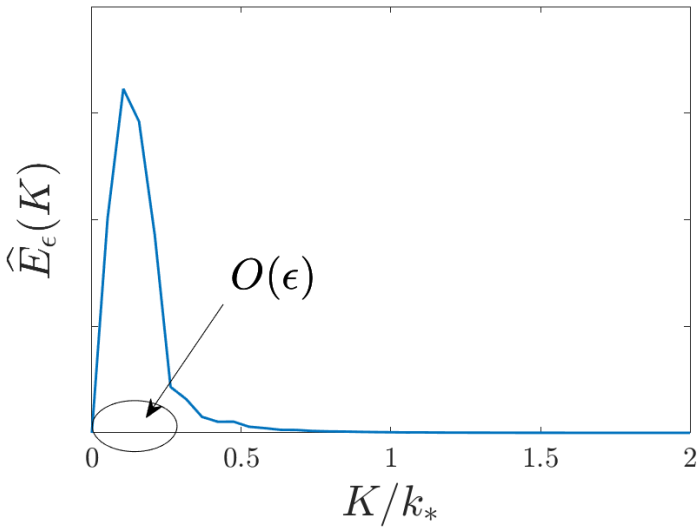

Figure 5-4. A representative horizontally isotropic geostrophic energy spectrum in the WKB regime, demonstrating energy localisation within an $O(\epsilon)$ region of the flow wavevector relative to the typical IGW scale. The localisation is modest (large ϵ) since this is taken from a simulation.

to small wavenumbers of order ϵ (see Figure 5-4) with

$$\widehat{R}_\epsilon(\boldsymbol{K}) := \widehat{R}(\epsilon\boldsymbol{K})/\epsilon^2.$$

We note that this is the same cross-section that would be obtained by including the effect of a weak random Doppler shift through advection as the sole effect of the background flow in the governing equations for the IGWs. In other words, starting from

$$\partial_t \boldsymbol{u} + \boldsymbol{U}\cdot\nabla\boldsymbol{u} + f\hat{\boldsymbol{z}}\times\boldsymbol{u} = -\nabla p + b\hat{\boldsymbol{z}},$$
$$\partial_t b + \boldsymbol{U}\cdot\nabla b + N^2 w = 0,$$
$$\nabla\cdot\boldsymbol{u} = 0,$$

and working through the procedure outlined in Chapter 2 yields a kinetic equation with the scattering cross-section (5-4.5).

The delta function $\delta(\boldsymbol{c}_g\cdot\boldsymbol{K})$ defining the resonant surface in this regime does not provide a route for waves to transfer across the nappes of the double cone. The group velocity vector is perpendicular to a given nappe, and so the flow wavevectors $\boldsymbol{K}$ must lie in a plane tangent to the cone at a point $\boldsymbol{k}$. In the limit $\epsilon\to 0$, waves scatter

by very small steps to carry out a random walk on a single nappe of the double cone. The averaged description of this process is diffusion, as described in Chapter 4.

We show in Appendix D that starting from the kinetic equation (5-3.10) in the WKB regime, it is possible to recover the diffusion equation from Chapter 4 in the short-wave limit $\epsilon \to 0$. We write the diffusion equation for $b = \sin\theta k^2\, a(\boldsymbol{x}, \boldsymbol{k}, t)$ in the form

$$\partial_t b + \nabla_{\boldsymbol{k}}\omega \cdot \nabla_{\boldsymbol{x}} b = \partial_k(k^2 \mathsf{D}_{kk}\partial_k(k^{-2}b)) + \frac{\mathsf{D}_{\varphi\varphi}}{k^2\sin^2\theta}\partial_{\varphi\varphi} b, \tag{5-4.6}$$

with θ a constant parameter. The right hand side of (5-4.6) describes a combination of an azimuthal relaxation of energy to a horizontally isotropic state at a given wavenumber k, controlled by $\mathsf{D}_{\varphi\varphi}(k,\theta)$, and a cascade of energy to different length scales controlled by the diffusivity $\mathsf{D}_{kk}(k,\theta)$. The calculations detailed in Appendix D show that these can be written in the form

$$\begin{aligned}\mathsf{D}_{\varphi\varphi}(k,\theta) &= \frac{1}{2}\int_{\mathbb{R}^3} \sigma_{\mathrm{WKB}}(\boldsymbol{k},\boldsymbol{k}')(\hat{\boldsymbol{e}}_\varphi\cdot(\boldsymbol{k}'-\boldsymbol{k})/\epsilon)^2 \mathrm{d}\boldsymbol{k}',\\ \mathsf{D}_{kk}(k,\theta) &= \frac{1}{2}\int_{\mathbb{R}^3} \sigma_{\mathrm{WKB}}(\boldsymbol{k},\boldsymbol{k}')(\hat{\boldsymbol{e}}_k\cdot(\boldsymbol{k}'-\boldsymbol{k})/\epsilon)^2 \mathrm{d}\boldsymbol{k}' = Qk^3,\end{aligned} \tag{5-4.7}$$

where $\hat{\boldsymbol{e}}_i$ denotes the unit vector in the i-direction. These expressions are exactly equivalent to those of Chapter 4. In Chapter 4 (4-2.6a) we show the less-than-obvious relation that the diffusivity D_{kk} has a simple powerlaw dependence on k, scaled by a constant $Q(\theta; f, N)$ which depends on physical parameters, and also on details of the flow which enter through its energy spectrum $\widehat{E}$. The azimuthal diffusivity $\mathsf{D}_{\varphi\varphi}$ is likewise the same as in Chapter 4 (4-2.6), and as before there is no diffusion in θ to leading order.

In Figure 5-5 we plot a version of D_{kk} where we have replaced the cross-section σ_{WKB} in (5-4.7) with the full cross-section (5-3.9), retaining only the same-nappe transfers $\theta' = \theta$, given by

$$\widetilde{\mathsf{D}}_{kk}(k,\theta) = \frac{1}{2}\int_{\mathbb{R}^3} \sigma(\boldsymbol{k},\boldsymbol{k}';\theta'=\theta)(\hat{\boldsymbol{e}}_k\cdot(\boldsymbol{k}'-\boldsymbol{k})/\epsilon)^2 \mathrm{d}\boldsymbol{k}'. \tag{5-4.8}$$

Figure 5-5 shows the convergence of $\widetilde{\mathsf{D}}_{kk} \to \mathsf{D}_{kk} = Qk^3$ for large values of k/K_*, as $\sigma \to \sigma_{\mathrm{WKB}}$.

Making the connection of the kinetic equation in this chapter with the diffusion equation of Chapter 4 provides a valuable cross-checking tool. We can use the simple

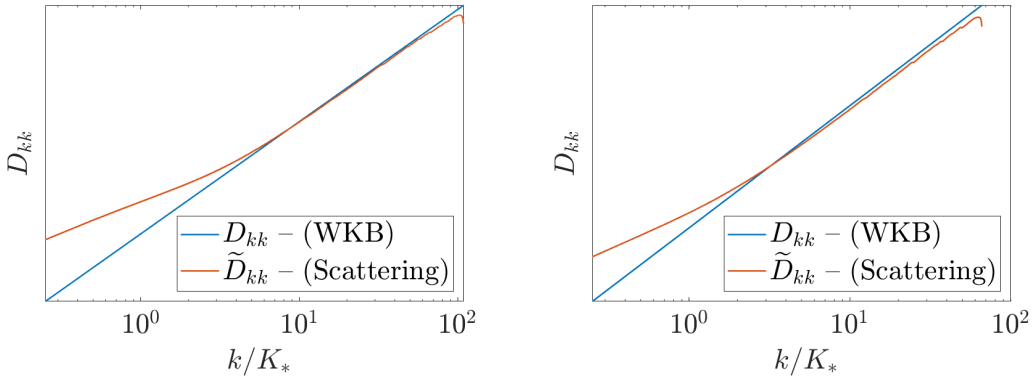

(a) Low Ro 2f **(b)** High Ro 3f

Figure 5-5. Diffusion coefficient associated with full cross-section σ, given by (5-4.8), against the WKB diffusion coefficient (5-4.7) which follows a k^3-power law.

results from the diffusion approximation to gain insight and intuition for what the kinetic equation can show. Showing that the diffusivities obtained by two separate, algebraically cumbersome routes agree in their formal representations provides a high degree of confidence in their correctness. Further, we later show simulations of the kinetic equation in the diffusion regime compared with the diffusion equation itself, and their agreement provides confidence in the numerical implementation of the equations and their results.

5-5 Simulations of horizontally isotropic IGWs

In this section we focus exclusively on horizontally isotropic IGWs. We compare simulations of the three-dimensional non-hydrostatic Boussinesq equations with the kinetic equation (5-3.15). The Boussinesq simulations were carried out by H. A. Kafiabad. We summarise the numerical details before presenting the results of the simulations.

Simulation details

As in Chapter 4, the Boussinesq equations are solved using a code adapted from that in Waite and Bartello (2006b) which relies on a de-aliased pseudospectral method and a third-order Adams–Bashforth scheme with timestep $0.015/f$. The triply-periodic

domain, $(2\pi)^3$ in the scale coordinates $(x, y, z' = Nz/f)$, is discretised uniformly with 768^3 grid points. A hyperdissipation of the form $-\nu(\partial_x^8+\partial_y^8+\partial_{z'}^8)$, with $\nu = 2\times10^{-17}$, is employed in the momentum and density equations. Again we take $N/f = 32$, a representative value of mid-depth ocean stratification. The initial condition is the superposition of a turbulent flow, obtained by running a quasigeostrophic model to a statistically stationary state, and IGWs. The initial spectrum of the flow peaks at $K_{\mathrm{h}*} \simeq 4$ and has an inertial subrange scaling approximately as K_{h}^{-3} and K_{v}^{-3}. This spectrum evolves slowly over the IGW-diffusion timescale, and its time-average defines $\widehat{E}$ which is used to calculate the cross-section $\sigma(\boldsymbol{k}, \boldsymbol{k}')$ in (5-3.9).

Simulations are performed for two Rossby numbers $\mathrm{Ro} = K_{\mathrm{h}*}\langle|\boldsymbol{U}|^2\rangle^{1/2}/f = 0.049,\ 0.099$ (or $\langle\zeta^2\rangle^{1/2}/f = 0.1,\ 0.2$ for the alternative Rossby numbers based on the vertical vorticity ζ), which we refer to as 'low' and 'high' Rossby numbers. We simulate the two IGW frequencies $\omega = 2f,\ 3f$. Upward-propagating horizontally isotropic IGWs are initialised as a ring in $\boldsymbol{k}$-space with $k_h = k_{h*}$, $k_v = \cot\theta k_{h*}$, random phases, and an initial kinetic energy $\langle|\boldsymbol{u}|^2\rangle/2 = 0.1\langle|\boldsymbol{U}|^2\rangle/2$. For the WKB regime experiments $k_{\mathrm{h}*} = 16 \simeq 4K_{h*}$, and for the scattering regime $k_{\mathrm{h}*} = 4 \simeq K_{h*}$. The IGW spectrum is computed at each step following the normal-mode decomposition of Bartello (1995). We retain data for a grid of size $(k_h, fk_v/N) \in [0, 254]\times[-255, 255]$, and then projecting this onto the double cone results in usable data on a one-dimensional grid of $k \in [-254/\sin\theta, 254/\sin\theta]$ with $\lfloor 511\cot\theta/(N/f)\rfloor$ evenly-spaced points (for our range of frequencies $\cot\theta/(N/f) \approx 1/2$). We take the convention that negative k values denote the lower nappe of the double cone with $\theta > \pi/2$, corresponding to downward-propagating waves.

The kinetic equation (5-4.2) for the horizontally isotropic mode $n = 0$ is simulated on an evenly-spaced grid of $k \in [-254/\sin\theta, 254/\sin\theta]$ interpolated to provide twice the resolution of data from the Boussinesq simulations for a given frequency, giving $2\times\lfloor 511\cot\theta/(N/f)\rfloor - 1$ grid points. The time-integration is accomplished using an Euler scheme with timesteps chosen so that $\Delta t = 0.5\,(\max_{\boldsymbol{k}}\Sigma(\boldsymbol{k}))^{-1}$. The discretised integrals in k' are computed using a Riemann sum, which respects the energy conservation property of the kinetic equation, and an FFT with 512 modes to compute the φ-averaged cross-section. We interpolate the geostrophic energy spectrum $\widehat{E}$ to double the resolution in each dimension for computing the cross-sections $\sigma_\pm$. Absorbing layers 20-grid points wide at each end of the domain are used to prevent cascaded energy from building up, and the energy at the apex of the

double cone is kept fixed at its initial value. For comparison, the diffusion equation (5-4.6) is solved on the upper nappe on the grid $k \in [0, 254/\sin\theta]$ with the same resolution as the kinetic equation, using first order central-difference differences for the k-derivatives, and a stiff ODE solver for time-stepping.

5-5.1 Scattering in the wave diffusion regime

We first investigate scattering in the regime of spatial-scale separation where the diffusion approximation of Chapter 4 holds, that is where the IGW wavenumber k_{h*} is much larger than the characteristic flow wavenumber K_{h*}. We present results for $\epsilon = K_{h*}/k_{h*} \simeq 0.25$ for initial value simulations in this section which is only moderately small but limitations of the available numerical resolution meant smaller values of ϵ were not practically accessible.

The initial spectrum $b^{\pm}(k, t_a)$ is obtained from the Boussinesq simulations after waiting for an adjustment period $t_a \gg (K_*|\boldsymbol{c}_g|)^{-1}$, the time for a wave packet to traverse typical eddies at the IGW group speed, required for the kinetic equation and diffusion equation to be valid (Besieris (1987); Müller *et al.* (1986) §5). We then solve the kinetic equation (5-3.15) taking $b^{\pm}(k, t_a)$ as the initial profile. The results of this procedure are presented in Figure 5-6, with a comparison of the kinetic equation spectra against the Boussinesq spectra for a subset of the four sets of values (Ro, ω). We see that the kinetic equation is able to forecast the energy profile on both nappes of the double cone, unlike its diffusion approximation counterpart, and captures the rate and shape of the decay well in both cases. Figure 5-7 displays the corresponding wave energy spectra in log–log coordinates, with the results of the diffusion equation included in Figure 5-7a for comparison. While both the kinetic equation and diffusion equation show good agreement with the numerical spectrum, it is clear that the kinetic equation avoids the tendency of the diffusion operator to flatten the portions of the spectrum with large curvature, such as the area to the left of the peak at small wavenumbers. We see that kinetic equation performs well in this regime even at the higher Rossby number, though it is difficult to assess its results for the highest wavenumbers since the absorbing layer at the end of the wavenumber domain relaxes all energy to zero there.

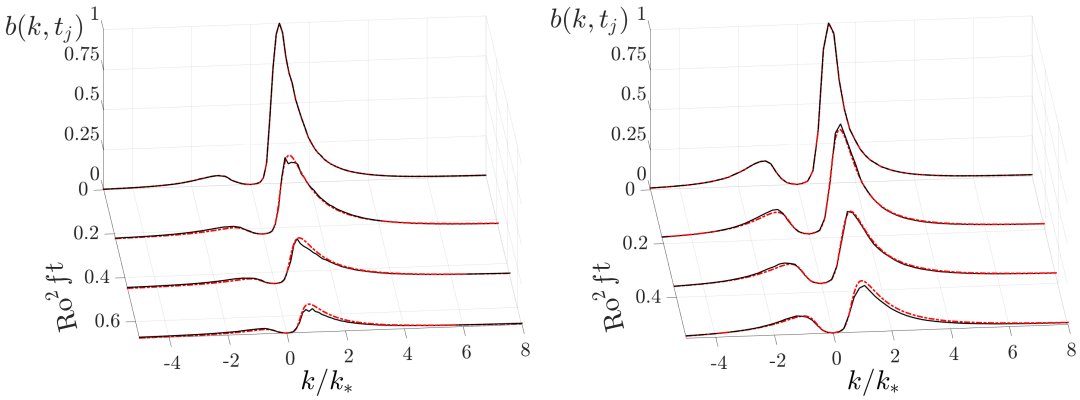

(a) $\omega = 2f$, low Ro. **(b)** $\omega = 3f$, high Ro.

Figure 5-6. Evolution of the IGW energy spectrum $b(k,t)$ in the wave diffusion regime with $\epsilon = K_{h*}/k_{h*} \simeq 0.25$. Here are results for the Boussinesq simulations (— black solid line) and kinetic equation (··· red dotted line). Negative wavenumbers correspond to the lower nappe of the double cone (downward-propagating IGWs).

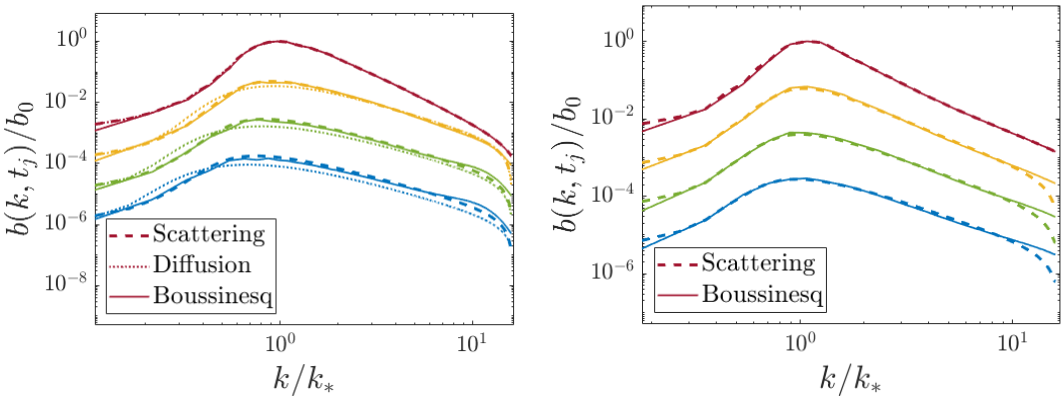

(a) $\omega = 2f$, low Ro. **(b)** $\omega = 3f$, high Ro.

Figure 5-7. Log-log representations of the $k > 0$ regions of Figure 5-6. The curves correspond to the times shown in Figure 5-6 and are successively shifted downwards by half a decade for clarity.

5-5.2 Beyond the wave diffusion regime

We now present results in the shared spatial-scale regime with $\epsilon = K_{h*}/k_{h*} \simeq 1$, comparing the kinetic equation with the full Boussinesq simulations. The results are somewhat harder to establish confidence in due to the relatively poor resolution of the spectra from the Boussinesq simulations in this regime. The peak wavenumber of the background flow remains at $K_h* \simeq 4$, and the IGW energy is initialised at $k_{h*} = 4$. However, the conversion of the spectra obtained on the (k_h, k_v) Cartesian grid to the $(k, \theta = \text{const})$ grid results in very crude looking energy profiles. This could be mitigated by taking a higher resolution Boussinesq simulation to begin with such that the flow should peak at a higher wavenumber, and the IGWs could be initialised at that same higher wavenumber but then with more grid points apart from the origin than these results. Achieving the higher resolution is costly, but appears to be necessary for future work. We emphasise though that the Boussinesq simulations in this chapter were simulated on a domain of 768^3 grid points which is already very high.

The results in this regime are presented in Figures 5-8, 5-9, and 5-10 for a log-log representation. They indicate that the kinetic equation (5-3.15) matches the Boussinesq simulations well when the differences in resolution between the curves are taken into account. The cascade is slower for smaller k_*/K_*, and so the results are presented for a greater period of time in order to see behaviour comparable to Figure 5-6. This lower cascade rate can perhaps be anticipated from the behaviour of the diffusion coefficient D_{kk} in Figure 5-5, which shows that diffusion of energy to different scales is slower for smaller values of k/K_*; though as the diffusion approximation does not apply for small k/K_*, such an interpretation should be treated with caution. Another difference in this regime is the much enhanced transfer of energy between the nappes of the cone, particularly noticeable for higher frequency. This is since the energy is initialised closer to the apex of the double cone than in the wave diffusion regime and physically it is more likely that a triad can be formed to bridge the smaller divide between the nappes.

Figure 5-11 presents a comparison of the function $\Delta(t) = \int (b^+ - b^-) \mathrm{d}\boldsymbol{k}$, predicted in §5-4.2 to decay to zero, obtained from the Boussinesq simulations and kinetic equation for a subset of the parameters $(k_*/K_*, \omega, \mathrm{Ro})$. We see that both the kinetic equation and Boussinesq simulations respect the theoretical lower-bound of the decay rate in all cases. However, these numerically calculated $\Delta(t)$ are not truly accurate due to the finite wavenumber domain of both the Boussinesq and kinetic equation,

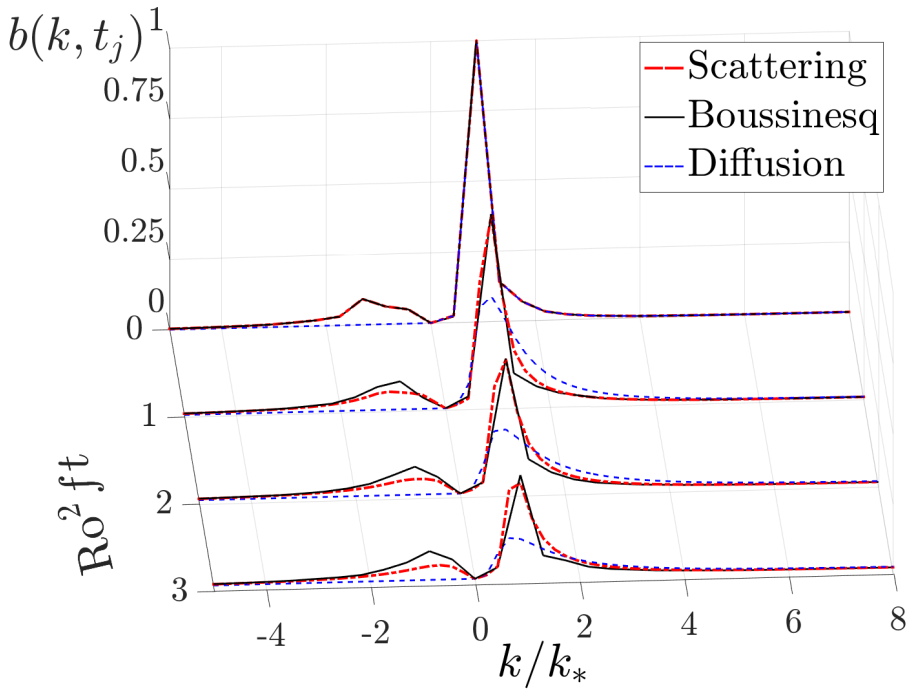

Figure 5-8. Evolution of the IGW energy spectrum $b(k,t)$ in the scattering regime with $K_*/k_* \simeq 1$, showing the Boussinesq simulations compared with the kinetic equation (5-3.15). Also included for contrast is the diffusion approximation prediction, which is being used outside of its valid regime. This simulation is for the parameters $\omega = 2f$, low Ro.

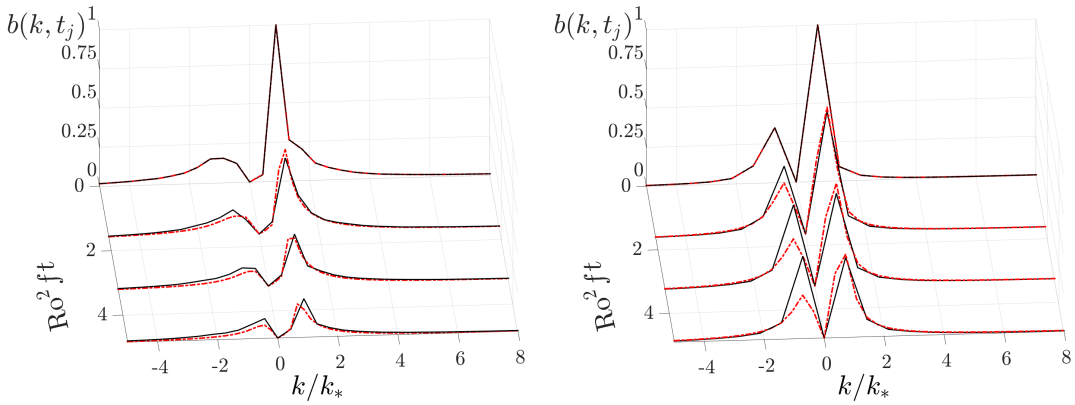

(a) $\omega = 2f$, high Ro. **(b)** $\omega = 3f$, high Ro.

Figure 5-9. Comparison of the IGW energy spectra from the Boussinesq simulations and the kinetic equation (5-3.15) in the regime $k_* \simeq K_*$. As described in the main text, though the resolution is relatively high for a Boussinesq simulation, it is visibly a limiting factor for these experiments.

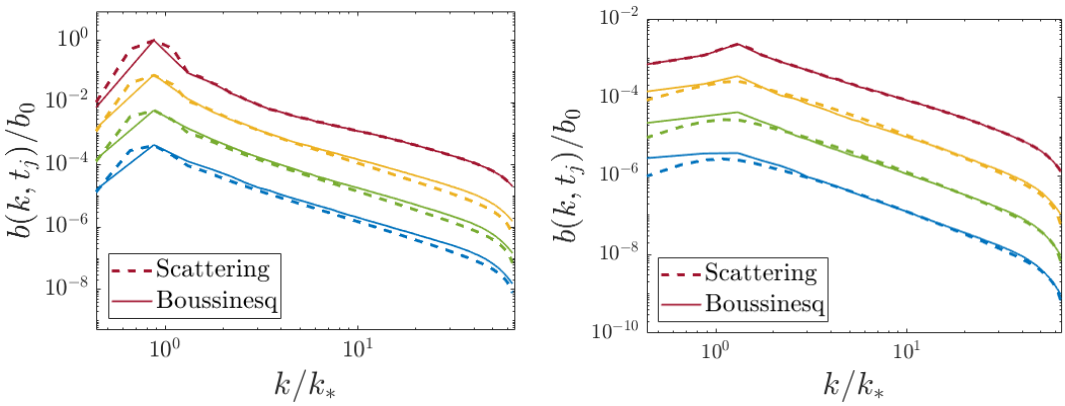

(a) $\omega = 2f$, high Ro, upper nappe. **(b)** $\omega = 2f$, high Ro, lower nappe.

Figure 5-10. A log-log representation of the IGW spectrum in Figure 5-9a. The curves correspond to the times shown in Figure 5-9a and are successively shifted downwards by half a decade for clarity. Note that interpolating the Boussinesq data for the kinetic equation gives a noticeable mismatch on the first few points.

with energy abruptly quenched at the higher wavenumbers, though they should be approximately correct for early times before the energy has cascaded to small scales. It is highly noticeable from this figure that the Boussinesq simulations with $k_* \simeq K_*$ suffer from being under-resolved, particularly at the higher IGW frequency of $\omega = 3f$.

5-5.3 Horizontally isotropic forcing of IGWs

It was shown in Chapter 4 §4 that, in the wave diffusion regime, the spectrum attained by IGWs balanced with a forcing of the form $\delta(k - k_*)$ is predicted to comprise two parts: a no-flux solution $b(k) \propto k^2$ and a constant-flux solution $b(k) \propto k^{-2}$. In the regime $k_* \simeq K_*$ we now must use the kinetic equation for horizontally isotropic IGWs, which we can write in the form (using (5-4.2) with $n = 0$)

$$\partial_t \boldsymbol{b} = 2\pi k^2 \int_0^\infty \widehat{\underline{\underline{\mathfrak{G}}}}_0(k,k')\, \boldsymbol{b}(k',t)\mathrm{d}k' - \Sigma(k)\, \boldsymbol{b}(k,t) + \boldsymbol{\mathcal{F}}, \tag{5-5.1}$$

where the forcing term

$$\boldsymbol{\mathcal{F}} = \begin{pmatrix} A\delta(k-k_*) \\ 0 \end{pmatrix}$$

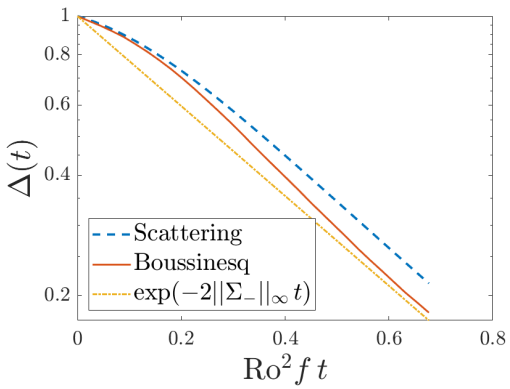

(a) $k_* \simeq 4K_*$, $\omega = 2f$, low Ro

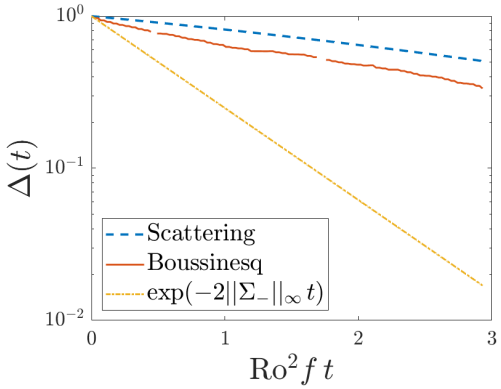

(b) $k_* \simeq K_*$, $\omega = 2f$, low Ro

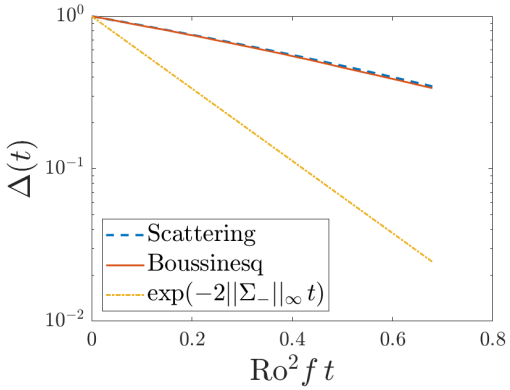

(c) $k_* \simeq 4K_*$, $\omega = 3f$, low Ro

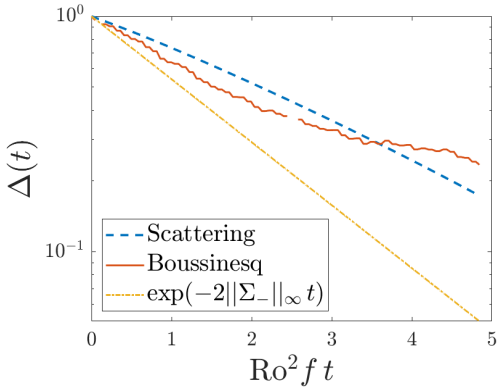

(d) $k_* \simeq K_*$, $\omega = 2f$, high Ro

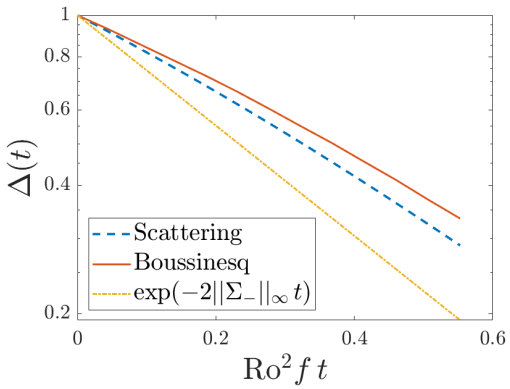

(e) $k_* \simeq 4K_*$, $\omega = 3f$, high Ro

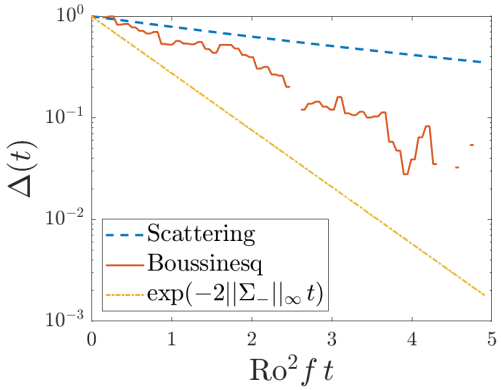

(f) $k_* \simeq K_*$, $\omega = 3f$, high Ro

Figure 5-11. Comparisons of $\Delta(t) = \int (b^+ - b^-)\mathrm{d}\boldsymbol{k}$ obtained from the kinetic equation simulations (- -blue dashed line) and Boussinesq simulations (—red line) against the theoretical lower-bound from §5-4.2 (··· yellow dotted line). The left column shows the WKB regime results, while the right column is in the scattering regime.

is applied only to upward-propagating waves. When the IGWs reach a statistically stationary state, the time derivative disappears from (5-5.1), and the solution $b^+ = b^- \propto k^2$ for $k < k_*$ is supported. The kinetic equation does not admit a simple power-law solution of the form $b^\pm \propto k^{-p}$ for the constant-flux $k > k_*$ part of the spectrum however, unlike the case for the diffusion equation. Given that the diffusion equation is a limit of the kinetic equation however, the solution of (5-5.1) should converge to $b^\pm \propto k^{-2}$ in the limit $K_*/k \to 0$.

Figure 5-12 shows the stationary spectra for $\mathrm{Ro} = 0.049$ and $\mathrm{Ro} = 0.099$ with the forcing wavenumber $k_{h*} \simeq K_{h*} = 4$. At high wavenumbers, before the absorbing layer causes the rapid decay of the energy spectra to zero, the slope appears to follow a k^{-2} power law. This is most clearly observed in Figure 5-12b, but it appears that there is not a single power law covering the entire range from forcing to dissipation scales. Figure 5-12 also includes the spectrum of downward-propagating waves from the unforced nappe of the double-cone. It is perhaps obvious that the equilibrium spectrum of downward-propagating waves should be the same as the upward-propagating ones, but we also observe that the difference in the energy level becomes indistinguishable for a broad range of scales outside the immediate vicinity of k_* between the spectra. This appears to be a further consequence of the equilibration property of the kinetic equation demonstrated in §5-4.2, though in the presence of forcing the analysis becomes complicated.

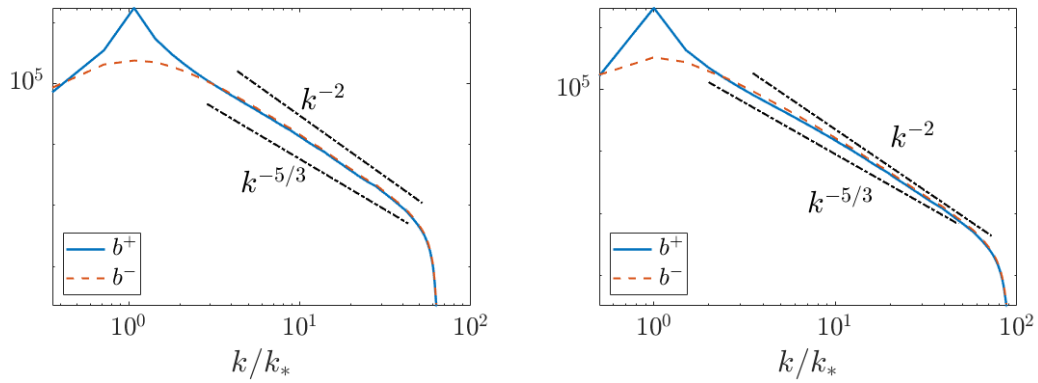

(a) Low Ro. **(b)** High Ro.

Figure 5-12. Equilibrium spectra resulting from forcing the upper-nappe only at IGW wavenumber $k_{h*} = 4 = K_{h*}$. (Arbitrary units on the vertical-axis.) We see here that a k^{-2} scaling is clearly achieved in the WKB regime of large k (large k/K_*), as predicted in Chapter 4. The spectrum at intermediate wavenumbers of $1 \lesssim k/k_* \lesssim 10$ appears to follow a shallower scaling close to $k^{-5/3}$, though the mechanism to explain this is not obvious.

5-6 Discussion

In this chapter we have introduced a new mathematical model, in the form of a kinetic equation, to provide a quantitative statistical description of IGWs propagating through and scattered by geostrophic turbulence. We have demonstrated that the kinetic equation (5-3.10) recovers the diffusion equation of Chapter 4 in the WKB limit, and that the cross-section (5-3.9) reduces to that of Chapter 3 when considering transfers with fixed vertical wavenumbers. The recovery of the results from the two previous chapters instils confidence in the form of the kinetic equation derived here, which is algebraically cumbersome to arrive at. The model presented in this chapter is more general than those of the preceding chapters, and has allowed previously neglected or missing effects to be included. Specifically, this kinetic equation is able to quantitatively predict the reflections of upward- to downward-propagating waves, while the kinetic equation revealed, and numerical experiments corroborated, that in an initial-value scenario the IGWs should reflect and equilibrate in the vertical. The function $\Delta(t)$ introduced in this chapter provides yet another perspective to compare how faithfully the kinetic equation captures the essential dynamics compared with the Boussinesq simulations and observations.

While the results of this chapter represent a significant step for quantifying the energy transfers of IGWs due to their interactions with the vortical mode, filling a gap in the literature that has been noted by several authors from Müller *et al.* (1986) to de Lavergne *et al.* (2019) among others, there is plenty of work remaining to be addressed. Though there were fewer restrictions and limitations than the preceding chapters, we have not tested the performance of the kinetic equation in the case of spatially inhomogeneous flows. Additionally we have left the investigation of the isotropisation of IGWs to future work, choosing instead to study already-isotropic IGWs. We showed that the kinetic equation predicts that the final state of IGWs scattered by horizontally isotropic turbulence is itself horizontally isotropic – this was borne out by simulations of the Boussinesq equations, but not presented in this chapter.

An important task for the future would be to establish the relative importance of wave-wave interactions compared to wave-vortical mode interactions. We have shown that interactions with the vortical mode, the 'catalytic interactions' of Lelong and Riley (1991) and Bartello (1995), can facilitate energy cascades in time scales comparable to other dynamical time scales in the atmosphere and ocean, and lead to equilibrium spectra that are consistent with as-yet-unexplained features observed by recent observational methods (Callies and Ferrari, 2013; Callies *et al.*, 2014; Bühler *et al.*, 2014; Qiu *et al.*, 2018). The theory developed in this chapter provides the mathematical foundation to quantify the impact of catalytic interactions, which has previously been assessed by mostly numerical observations and heuristic arguments.

Chapter 6

Conclusion

6-1 Summary

We described in Chapter 1 how IGWs contribute in important ways to a number of processes in the atmosphere and ocean, and that they may be responsible for much of the observed variability in the poorly-understood submesoscale range of the atmosphere and ocean. This thesis has developed new theory that can be used to assess the hypothesis that submesoscale IGWs are controlled by their interactions with geostrophic turbulence, and to understand the contribution of IGWs to submesoscale dynamics in general. We have shown that geostrophic turbulence is an important agent for redistributing energy in the atmosphere and ocean, and could potentially explain some of the observed but unexplained features in their energy spectra.

Through this thesis we have derived a series of kinetic equations, which give a statistical description and quantification of IGW energy transfers across physical and spectral space, with increasingly general applicability. In Chapter 3 we considered scattering by flows with no vertical structure which allowed the equations governing the IGWs to be reduced to an equivalent rotating shallow-water system. In such a model the energy-transfers are confined to be horizontal. The kinetic equation took the form of a so-called scattering integral, reminiscent of the Boltzmann equation in non-equilibrium statistical mechanics. Then in Chapter 4 we explored the interactions of geostrophic turbulence having a non-trivial vertical dependence with short length-scale IGWs such that the WKB approximation applies. In this regime the kinetic

equation takes the form of a diffusion equation in phase space. Finally in Chapter 5 we went beyond the WKB limit to consider a complete description of IGWs with no spatial-scale separation relative to the geostrophic turbulence. The kinetic equation here also took the form of a scattering integral, and we showed that the kinetic equations of Chapters 3 and 4 could be recovered from it in the appropriate limits, demonstrating a satisfying consistency between the theories.

6-1.1 Main results

Here we summarise and review the findings of Chapters 3–5, which together provide a rich description of the impact of geostrophic turbulence on IGWs, with their spectral transfers quantified and the role of the vortical mode in shaping the distribution of IGW energy highlighted in detail.

Given that the kinetic equations of Chapters 3 and 4 are limiting cases of the kinetic equation of Chapter 5, it comes as no surprise that there are related themes and outcomes that are common to all of the three chapters. We first discuss the general findings and outcomes before focusing on those that are specific to each chapter individually.

General findings and outcomes

Each of the simplified models we derived shared similarities in their mathematical form. As highlighted in Chapter 2, the models can be generically written as

$$\partial_t a + \nabla_{\boldsymbol{k}}\omega \cdot \nabla_{\boldsymbol{x}} a - \nabla_{\boldsymbol{x}}\omega \cdot \nabla_{\boldsymbol{k}} a = \mathcal{L}_{sc} a,$$

with $a(\boldsymbol{x}, \boldsymbol{k}, t)$ the energy density given in terms of the Wigner transform of the IGW fields, $\omega(\boldsymbol{x}, \boldsymbol{k})$ the dispersion relation of the linear waves, and $\mathcal{L}_{sc}$ a scattering operator.

We showed that in each case the form of the scattering operator $\mathcal{L}_{sc}$ restricts energy transfers to constant-frequency surfaces in wavenumber space. The constant-frequency surface accessible through scattering depends on the underlying model or limit being considered. In Chapter 5 the resonant surface was shown to be a double-cone for IGWs scattered by geostrophic turbulence with no spatial-scale separation

assumed, and non-trivial vertical dynamics. By contrast the WKB limit of that model, as considered in Chapter 4, has a scattering operator which indicates that IGWs are restricted to just a single nappe of the resonant double-cone. For the barotropic flows considered in Chapter 3, where there is no vertical shear by the flow to transfer energy vertically, the transfers are restricted to circles in wavenumber space where a vertical mode corresponds to two circles, one on each nappe spaced equally from the apex. Scattering then transfers energy around a single nappe of the double-cone and at a fixed horizontal and vertical wavenumber.

A common feature of the scattering operator $\mathcal{L}_{sc}$ for the different models is its linear dependence on the geostrophic energy spectrum $\widehat{E}(\boldsymbol{K})$. This has a direct and simple implication for the rate of scattering; the rate of scattering, including scale cascades and isotropisation, varies as U_*^{-2}, where U_* is a characteristic velocity of the flow, for example the rms velocity of the geostrophic turbulence. When the geostrophic energy spectrum is horizontally isotropic such that $\widehat{E} = \widehat{E}(|\boldsymbol{K}_h|, K_v)$, then we found in each of the models that an arbitrary IGW distribution is relaxed into horizontal isotropy by it.

Finally we note that each of the models conserve the total energy $E = \iint a \mathrm{d}\boldsymbol{k}\mathrm{d}\boldsymbol{x}$, as well as the wave action $\mathcal{A} = E/\omega$ that is usually found to be the conserved quantity in wave–mean flow interacting systems (e.g. Salmon (1998); Olbers *et al.* (2012)). This is because the weak-flow assumption means the energy differs from the action by only a small term. Indeed we have shown that to leading order the intrinsic frequency ω is independent of time and unaffected by scattering.

We now briefly summarise the results that were particular to each chapter.

Chapter 3: Scattering of internal tides

The focus of this chapter was the application of internal tide (IT) scattering, and so the kinetic equation was used to conduct an investigation of the physical parameter dependence of IT scattering which was summarised in Figure 3-2. The kinetic equation for this chapter took a relatively simple form that allowed for an explicit calculation of the rate of isotropisation of IGWs by an isotropic flow in a straightforward way, along with an estimate of the length scales that ITs can propagate before becoming isotropised. We demonstrated that the time scales were similar to those found in Ward

and Dewar (2010), who studied IT scattering in a deterministic framework. The rate of scattering was shown to be comparable with those due to the fastest wave–wave interactions of PSI at the critical latitude (Ward and Dewar, 2010).

Chapter 4: Diffusion of IGWs by geostrophic turbulence

The diffusion equation of this chapter was shown to be amenable to explicit analytic solutions for initial-value decay and steady forcing scenarios. We showed this for spatially homogeneous, horizontally isotropic IGWs. Interestingly, we showed that steady forcing achieves a k^{-2} stationary spectrum. This is potentially relevant for understanding some universal features of atmospheric and oceanic spectra, though further investigation is required to establish the importance of this mechanism in determining observed features in such spectra.

Chapter 5: Scattering of IGWs by geostrophic turbulence

The kinetic equation of this chapter is the main outcome of the thesis. It incorporates features missing from the previous chapters such as the reflection of upwards- to downwards-propagating waves, yet it recovers the kinetic equations of two preceding chapters in the appropriate limits. The kinetic equation furthermore revealed new insights into the dynamics of IGWs scattered by geostrophic turbulence. In particular it predicts the equilibration of waves in the vertical as well as providing an explicit bound on the rate that equilibration is achieved – such additional insight is potentially useful for designing parameterisations.

Due to the non-compact resonant surface – the double-cone – and the non-local nature of the transfers in this system, the scattering behaviour is necessarily more complicated than the preceding chapters, and explicit estimates and solutions were not given. However, numerical comparisons with high-resolution simulations of the Boussinesq equations in this chapter showed that the kinetic equation gives a good statistical description of the scattering of IGWs by geostrophic turbulence.

6-2 Further work

While the work contained in this thesis constitutes progress for understanding the interplay between IGWs and geostrophic turbulence, it has left several avenues open for exploration.

First, there are a number of ideas that can be considered within the framework of the theory presented in this thesis. We established in Chapter 5 that an arbitrary distribution of IGWs is ultimately horizontally isotropised through interactions with a horizontally isotropic flow, but there is more that can be done to describe the process in detail. For example it would be worthwhile investigating how the rate of isotropisation depends on the relative length scale of the IGWs and the flow, and how the rate of isotropisation in general compares with the rate of the scale cascades. Simulations of the Boussinesq equations indicated that the isotropisation occurs on a rapid time scale compared with the cascades, but the kinetic equation could be useful for exploring a range of different initial IGW distributions, and the effect of varying the physical parameters, with less computational effort in the highly simplified context of simulating transfers on the cone. In general, the kinetic equation is computationally demanding to simulate as it is an equation defined on the 6-dimensional $(\boldsymbol{x}, \boldsymbol{k})$ phase space. However, by considering experiments that ignore variations in physical space, it is quite efficient for studying transfers on the 2-dimensional resonant surface in wavenumber space.

Throughout this thesis we have considered scattering by horizontally isotropic and spatially homogeneous flows, but the kinetic equation requires neither of these restrictions. Indeed, it would be interesting to consider how the IGW distributions and energy transfers are affected by considering scattering by features such as jets and shear flows, or with spatially varying versions f and N. Another aspect that we have touched upon but not explored in depth is the relaxation to equilibrium of a forced IGW spectrum. For example, Müller *et al.* (1986) present the Boltzmann and Langevin rates which characterise the relaxation of a distorted spectrum to its equilibrium through the decay of spikes in an otherwise smooth stationary spectrum. These rates can be used to define parameterised viscosity coefficients that characterise the effect of IGWs on the background flow, and the kinetic equation is well suited for exploring such rates.

Second, we set out some of the main restrictions and assumptions in Chapter 2 that

the theory in this thesis operates within, and naturally there are questions to explore that extend beyond such limitations. All of the models we have explored in this thesis have assumed that the background flow interacts only weakly with the IGWs such that it is dominated by their dispersion effects. While this assumption is valid for many parts of the atmosphere and ocean (Alford *et al.*, 2016; Callies *et al.*, 2014) it is not the full story, and indeed breaks down at small scales and for background flows with a Rossby number $\mathrm{Ro} > O(1)$. In such cases it is not possible to derive a kinetic equation to describe the average properties of IGWs propagating through a random background flow as we have done, but instead, in the eikonal regime described in Chapter 2 §1, the transport equation becomes

$$\partial_t a + \nabla_{\boldsymbol{k}}\Omega \cdot \nabla_{\boldsymbol{x}} a - \nabla_{\boldsymbol{x}}\Omega \cdot \nabla_{\boldsymbol{k}} a = 0, \tag{6-2.1}$$

where $\Omega = \omega + \boldsymbol{U} \cdot \boldsymbol{k}$ is the Doppler-shifted absolute frequency. While this equation appears simple, it is a stochastic equation with the coefficients depending on the particular realisation of the geostrophic velocity field $\boldsymbol{U}$. The equation would be relatively simple to simulate if not for its high dimensionality, with $(\boldsymbol{x}, \boldsymbol{k}, t) \in \mathbb{R}^3 \times \mathbb{R}^3 \times \mathbb{R}$. The statistics of (6-2.1) were investigated in the 1970-80s for a one-dimensional setup in the context of wave-wave interactions (Henyey and Pomphrey, 1983; Flatté *et al.*, 1985; Müller *et al.*, 1986), investigating fields that depend on z only. However, it is known that the one-dimensional scenario is idiosyncratic as the presence of random critical layers in the vertical trap IGWs so that they cannot propagate (also known as Anderson localisation). If the computational difficulties of the high dimensionality can be overcome, it would be useful to study the statistics of IGWs propagating in the eikonal regime, both in the context of wave-vortical mode interactions and wave-wave interactions.

It would also be desirable to develop theory to consider higher-order effects such as information about the IGW phase, and frequency broadening. The confinement of IGW energy to the constant-frequency surfaces in this thesis is a consequence of the assumption of stationarity for the flow. If this is relaxed, there is frequency broadening. The method presented in Chapter 2 which focuses on scattering in the $(\boldsymbol{x}, \boldsymbol{k})$ phase-space using a spatial Wigner transform can be extended with a spatio-temporal Wigner transform to consider transfers in $(\boldsymbol{x}, \boldsymbol{k}, \omega, \tau)$ (Bal, 2005). Such a method could be used to investigate the energy transfers perpendicular to the surface

of the resonant cone which may help to unpick how the continuum of energy observed in frequency spectra, such as the one shown in Figure 1-1a, is established.

Appendix A

Potential vorticity in the linear Boussinesq equations

The full expression for the potential vorticity (anomaly) is as follows:

$$\begin{aligned} q &= (f\hat{\boldsymbol{z}} + \nabla \times \boldsymbol{u}) \cdot (N^2\hat{\boldsymbol{z}} + \nabla b) - fN^2 \\ &= f\partial_z b + N^2\zeta + (\nabla \times \boldsymbol{u}) \cdot \nabla b, \end{aligned}$$

where we have defined the vertical component of the vorticity as $\zeta = \hat{\boldsymbol{z}} \cdot \nabla \times \boldsymbol{u}$.

In the linear approximation, we have the linear potential vorticity given simply by

$$q_l = f\partial_z b + N^2\zeta. \tag{A-0.1}$$

Now, using the linear Boussinesq equations given by (1-2.8) we can derive the equations for the vertical vorticity ζ and the horizontal divergence given by $\delta = \nabla_h \cdot \boldsymbol{u} = -\partial_z w$ to obtain

$$\partial_t \delta = f\zeta - \nabla_h^2 \tilde{p}, \tag{A-0.2}$$

$$\partial_t \zeta = -f\delta. \tag{A-0.3}$$

These can be combined by taking ∂_t(A-0.2) and substituting (A-0.3) to obtain

$$(\partial_{tt} + f^2)\delta = -\nabla_h^2 \partial_t \tilde{p}. \tag{A-0.4}$$

Also from (1-2.8) are the equations for the vertical velocity and the buoyancy, given by

$$\partial_t w = -\partial_z \tilde{p} + b, \tag{A-0.5}$$

$$\partial_t b = -N^2 w. \tag{A-0.6}$$

Taking $\partial_t \partial_z$(A-0.5)$-\partial_z$(A-0.6) gives

$$(\partial_{tt} + N^2)\delta = \partial_{zz} \partial_t \tilde{p}. \tag{A-0.7}$$

Now, taking $(\partial_{tt} + f^2)$(A-0.7)$-(\partial_{tt} + N^2)$(A-0.4) gives

$$\partial_t [\partial_{tt} \nabla^2 + f^2 \partial_{zz} + N^2 \nabla_h^2] \tilde{p} = 0. \tag{A-0.8}$$

Taking an ansatz of the form $\tilde{p}(\boldsymbol{x}, t) = \hat{p}(\boldsymbol{x}) e^{-i\omega t}$, we find that (A-0.8) has two distinct solutions. If $\omega = 0$, it leaves the possibility that

$$[\partial_{tt} \nabla^2 + f^2 \partial_{zz} + N^2 \nabla_h^2] \tilde{p} = F(\boldsymbol{x}), \tag{A-0.9}$$

so that F is a function of space only and is determined by the initial state of the pressure $\tilde{p}(\boldsymbol{x}, t)$. On the other hand if $\omega \neq 0$, then the solution to (A-0.8) demands that

$$[\partial_{tt} \nabla^2 + f^2 \partial_{zz} + N^2 \nabla_h^2] \tilde{p} = 0, \tag{A-0.10}$$

so that when $\omega \neq 0$, $F \equiv 0$.

Now, it is possible to express the linearised potential vorticity q_l in terms of the pressure $\tilde{p}$. Note that from (A-0.2) and ∂_z(A-0.5) we have

$$f q_l = (N^2 - f^2)\partial_t \delta + (f^2 \partial_{zz} + N^2 \nabla_h^2)\tilde{p}. \tag{A-0.11}$$

To eliminate the term involving the horizontal divergence we take $\partial_t\big($(A-0.7)$-$(A-0.4)$\big)$

which gives

$$(N^2 - f^2)\partial_t \delta = \partial_{tt} \nabla^2 \tilde{p}. \tag{A-0.12}$$

Substituting (A-0.12) into (A-0.11), we find from (A-0.9) that

$$F(\boldsymbol{x}) = f q_l.$$

From Chapter 1 §1-2, we have shown that the linear Boussinesq system (1-2.8) admits two distinct solutions – the IGW modes with $\omega = \omega_{\pm}$ and the vortical mode with $\omega = 0$. We also described how the system has a conserved quantity in the form of the linearised potential vorticity q_l. This appendix has established that we can discriminate between the IGW and vortical mode solutions based on q_l. When $\omega = \omega_{\pm}$, $q_l \equiv 0$, and when $\omega = 0$, $q_l = q_l(\boldsymbol{x})$ can be non-zero.

Appendix B

Vertical mode decomposition

Since the background flow in (3-2.1) is barotropic, we project onto a vertical-mode basis according to

$$\begin{pmatrix} u \\ v \\ w \\ p \\ b \end{pmatrix} = \sum_{m=0}^{\infty} \begin{pmatrix} u_m(x,y,t) & F_m(z) \\ v_m(x,y,t) & F_m(z) \\ w_m(x,y,t) & N^{-2}(z)F'_m \\ p_m(x,y,t) & F_m(z) \\ b_m(x,y,t) & F'_m \end{pmatrix}, \tag{B-0.1}$$

where the F_m are eigenfunctions of the Sturm–Liouville problem

$$\mathscr{L}F_m = -\frac{1}{r_m^2}F_m, \quad F'_m(0) + N^2F_m(0)/g = 0, \;\; F'_m(-H) = 0,$$

where $\mathscr{L}(\cdot) = \partial/\partial z[f^2/N^2\partial/\partial z(\cdot)]$ and H is the ocean depth (Olbers *et al.*, 2012). The eigenvalues r_m are the Rossby radii of deformation. Orthonormality implies

$$(F_n, F_m) = \int_{-H}^{0} F_m F_n \mathrm{d}z = \delta_{mn}.$$

Substituting (B-0.1) into (3-2.1) leads to a system for the amplitudes u_m, v_m, etc. of each baroclinic mode m. Defining the equivalent depth $h_m = f^2 r_m^2/g$ and the equivalent surface height $\eta_m = b_m/g$, we rewrite this system in the shallow-water-like form given by (3-2.2).

Appendix C

Derivation of the diffusion equation and of its solution

C-1 General wave systems

We introduce a small parameter $\mathrm{Ro} \ll 1$ in the action conservation (4-2.1) by writing the frequency as $\Omega = \omega + \mathrm{Ro}\, \boldsymbol{U} \cdot \boldsymbol{k}$, indicating that the velocity field is weak enough for the intrinsic frequency to dominate over the Doppler shift. Defining slow time and spatial scales by $T = \mathrm{Ro}^2 t$ and $\boldsymbol{X} = \mathrm{Ro}^2 \boldsymbol{x}$, we substitute the expansion

$$a = a^{(0)}(\boldsymbol{X}, \boldsymbol{k}, T) + \mathrm{Ro}\, a^{(1)}(\boldsymbol{x}, \boldsymbol{X}, \boldsymbol{k}, t, T) + \cdots$$

into (4-2.1). The first non-trivial equation appears at $O(\mathrm{Ro})$ and is given by

$$\partial_t a^{(1)} + c_i \partial_{x_i} a^{(1)} = k_m \partial_{x_i} U_m \, \partial_{k_i} a^{(0)},$$

using Cartesian components and implied summation. Assuming that the velocity field varies on the slow time scale only, the solution is given by

$$a^{(1)}(\boldsymbol{x}, \boldsymbol{X}, \boldsymbol{k}, t, T) = k_m \int_0^t \partial_{x_j} U_m(\boldsymbol{x} - \boldsymbol{c}s, T)\, \mathrm{d}s \, \partial_{k_j} a^{(0)}. \tag{C-1.1}$$

Averaging the next-order equation to eliminate the terms containing $a^{(2)}$, we find

$$\partial_T a^{(0)} + c_i \partial_{X_i} a^{(0)} = k_n \langle \partial_{x_i} U_n \partial_{k_i} a^{(1)} \rangle,$$

since $\langle U_i \partial_{x_i} a^{(1)} \rangle = \langle \partial_{x_i} (U_i a^{(1)}) \rangle = 0$ using incompressibility and spatial homogeneity. Substituting the limit of (C-1.1) as $t \to \infty$ as appropriate for the slow dynamics, we obtain the diffusion equation

$$\partial_T a^{(0)} + c_i \partial_{X_i} a^{(0)} = \partial_{k_i} \left(\mathsf{D}_{ij} \partial_{k_j} a^{(0)} \right) \tag{C-1.2}$$

with the diffusivity

$$\mathsf{D}_{ij} = -k_m k_n \int_0^\infty \langle \partial_{x_i} U_n(\boldsymbol{x}) \partial_{x_j} U_m(\boldsymbol{x} - \boldsymbol{c}s) \rangle \, \mathrm{d}s.$$

This can be written as (4-2.4) in terms of the correlation tensor Π_{mn} or, alternatively, as

$$\mathsf{D}_{ij} = \frac{k_m k_n}{8\pi^2} \int_{\mathbb{R}^3} K_i K_j \hat{\Pi}_{mn}(\boldsymbol{K}) \delta(\boldsymbol{K} \cdot \boldsymbol{c}) \, \mathrm{d}\boldsymbol{K}, \tag{C-1.3}$$

in terms of the Fourier transform $\hat{\Pi}_{mn}$ of Π_{mn}. The diffusive approximation (C-1.2) is standard for Hamiltonian systems with weak random perturbation and has been obtained in a variety of contexts (e.g., McComas and Bretherton (1977) for wave–wave interactions). The formal derivation above follows Bal *et al.* (2010, §4.2) who also discuss its rigorous justification.

C-2 IGWs in quasigeostrophic flow

We particularise (C-1.3) to the IGW dispersion relation (4-2.2) and a velocity field of the form $\boldsymbol{U} = (-\partial_{x_2}\psi, \partial_{x_1}\psi, 0)$ with ψ the geostrophic streamfunction. We use the spherical polar coordinates (k, θ, φ) for $\boldsymbol{k}$, with $\boldsymbol{e}_k$, $\boldsymbol{e}_\theta$ and $\boldsymbol{e}_\varphi$ the corresponding unit vectors, and express the group velocity as

$$\boldsymbol{c}(\boldsymbol{k}) = \frac{(N^2 - f^2)\cos\theta \sin\theta}{k\omega} \, \boldsymbol{e}_\theta.$$

The diffusivity can be written in the basis $(\boldsymbol{e}_k, \boldsymbol{e}_\theta, \boldsymbol{e}_\varphi)$ as

$$\mathsf{D} = \mathsf{D}_{kk} \, \boldsymbol{e}_k \otimes \boldsymbol{e}_k + \mathsf{D}_{k\varphi} (\boldsymbol{e}_k \otimes \boldsymbol{e}_\varphi + \boldsymbol{e}_k \otimes \boldsymbol{e}_\varphi) + \mathsf{D}_{\varphi\varphi} \, \boldsymbol{e}_\varphi \otimes \boldsymbol{e}_\varphi, \tag{C-2.1}$$

where $D_{kk} = \boldsymbol{e}_k \cdot \mathbf{D} \cdot \boldsymbol{e}_k$, $D_{k\varphi} = \boldsymbol{e}_k \cdot \mathbf{D} \cdot \boldsymbol{e}_\varphi$, $D_{\varphi\varphi} = \boldsymbol{e}_\varphi \cdot \mathbf{D} \cdot \boldsymbol{e}_\varphi$, and we have made use of the fact that $\mathbf{D} \cdot \boldsymbol{e}_\theta \propto \mathbf{D} \cdot \boldsymbol{c} = 0$ to eliminate all components along $\boldsymbol{e}_\theta$.

With Θ and Φ the polar and azimuthal angles of the flow wavevector $\boldsymbol{K}$, we have

$$\begin{aligned}\boldsymbol{K} &= K(\sin\Theta\sin\theta\cos\gamma + \cos\Theta\cos\theta)\,\boldsymbol{e}_k \\ &\quad + K\sin\Theta\sin\gamma\,\boldsymbol{e}_\varphi + K(\sin\Theta\cos\theta\cos\gamma - \cos\Theta\sin\theta)\,\boldsymbol{e}_\theta,\end{aligned}$$

where $\gamma = \Phi - \varphi$. Hence the delta function in (C-1.3) can be written as

$$\delta(\boldsymbol{K}\cdot\boldsymbol{c}) = \frac{k\omega\,(\delta(\gamma-\gamma_*)+\delta(\gamma+\gamma_*))}{K(N^2-f^2)\sin\Theta\sin\theta\cos^2\theta\sin\gamma_*}, \tag{C-2.2}$$

where $0 \le \gamma_* = \cos^{-1}(\tan\theta/\tan\Theta) \le \pi$. We also note that

$$k_m k_n \hat{\Pi}_{mn} = (k_1K_2 - k_2K_1)^2\langle\hat{\psi}(\boldsymbol{K})\hat{\psi}(-\boldsymbol{K})\rangle = 2k^2\sin^2\theta\sin^2\gamma E(\boldsymbol{K}), \tag{C-2.3}$$

where $E(\boldsymbol{K}) = K^2\sin^2\Theta\langle\hat{\psi}(\boldsymbol{K})\hat{\psi}(-\boldsymbol{K})\rangle/2$ is the flow kinetic energy spectrum. We now introduce (C-2.2)–(C-2.3) into (C-1.3) projected onto $\boldsymbol{e}_k$ and $\boldsymbol{e}_\varphi$ to compute the components of $\mathbf{D}$ in (C-2.1). Assuming that the flow is isotropic in the horizontal so that $E(\boldsymbol{K})$ is independent of γ, we obtain after some simplifications

$$D_{kk} = \frac{k^3\omega\sin^2\theta}{2\pi^2(N^2-f^2)|\cos^5\theta|}\int_{-\infty}^{\infty}\int_{-\theta}^{\pi-\theta} K^3\cos^2\Theta(\cot^2\theta-\cot^2\Theta)^{1/2}E(\boldsymbol{K})\,\mathrm{d}K\mathrm{d}\Theta,$$

$$D_{\varphi\varphi} = \frac{k^3\omega\sin^4\theta}{2\pi^2(N^2-f^2)|\cos^5\theta|}\int_{-\infty}^{\infty}\int_{-\theta}^{\pi-\theta} K^3\sin^2\Theta(\cot^2\theta-\cot^2\Theta)^{3/2}E(\boldsymbol{K})\,\mathrm{d}K\mathrm{d}\Theta,$$

and $D_{k\varphi} = 0$. The form (4-2.6) follows by replacing the kinetic-energy spectrum $E(\boldsymbol{K})$ by its two-dimensional counterpart $E(K_\mathrm{h},K_\mathrm{v}) = 2\pi K_\mathrm{h}E(\boldsymbol{K})$ and changing the integration variables from (K,Θ) to $(K_\mathrm{h},K_\mathrm{v})$, with $K\,\mathrm{d}K\mathrm{d}\Theta = \mathrm{d}K_\mathrm{h}\mathrm{d}K_\mathrm{v}$.

C-3 Solution of (4-3.1) and its long-time approximation

Introducing a solution of the separable form $e(k,t) = \mathrm{e}^{-Q\lambda^2 t/4} f(k,\lambda)$, with $\lambda \geq 0$ a spectral parameter, into (4-3.1) leads to

$$k^3 f'' + k^2 f' + 4\left(\lambda^2/16 - k\right) f = 0,$$

where the prime denotes derivative with respect to k. Solutions bounded as $k \to 0$ are proportional to the Bessel function $J_4(\lambda/\sqrt{k})$. The general solution of (4-3.1) follows as

$$e(k,t) = \int_0^\infty A(\lambda) J_4(\lambda/\sqrt{k}) \mathrm{e}^{-Q\lambda^2 t/4}\, \mathrm{d}\lambda,$$

for an arbitrary function $A(\lambda)$. Imposing the initial condition $e(k,0) = \delta(k-k_*)$ yields (4-3.2) on using the Bessel-function expansion of $\delta(k-k_*)$ (*NIST Digital Library of Mathematical Functions*, 2018, Eq. 1.17.13).

For large t, the integral in (4-3.2) is dominated by a neighbourhood of $\lambda = 0$. The Bessel functions J_4 can therefore by replaced by their small-argument approximation, $J_4(z) \sim z^4/16$ as $z \to 0$ (*NIST Digital Library of Mathematical Functions*, 2018, Eq. 10.2.1), leading to

$$e(k,t) \propto k^{-2} \int_0^\infty \lambda^9\, \mathrm{e}^{-Q\lambda^2 t/4}\, \mathrm{d}\lambda \propto k^{-2} t^{-5}.$$

Appendix D

Diffusion limit of the kinetic equation

In this appendix we show how to pass from the kinetic equation (5-3.10) to its diffusion approximation.

The diffusion approximation is valid in the WKB regime, where local transfers dominate in the kinetic equation so that waves with wavevector $\boldsymbol{k}$ are scattered by a small amount to $\boldsymbol{k}' = \boldsymbol{k} + \epsilon\boldsymbol{K}$, with $\boldsymbol{K}$ a large scale flow wavevector to make up a triad $(\boldsymbol{k}, \boldsymbol{K}, \boldsymbol{k}')$, and $\epsilon \ll 1$ here is a bookkeeping parameter.

We substitute $\boldsymbol{k}' = \boldsymbol{k} + \epsilon\boldsymbol{K}$ into the full scattering cross-section $\sigma(\boldsymbol{k}, \boldsymbol{k}')$, given by (5-3.9), and Taylor expand to obtain the simpler cross-section

$$\sigma_{\mathrm{WKB}}(\boldsymbol{k}, \boldsymbol{k} + \epsilon\boldsymbol{K}) = 2\pi\epsilon^{-d}|\boldsymbol{k}_h \times \boldsymbol{K}_h|^2 R_\epsilon(\boldsymbol{K})\delta\big(\boldsymbol{c}_g \cdot \boldsymbol{K}\big), \tag{D-0.1}$$

with $d = 3$. In order to obtain this we have Taylor expanded the resonant delta-function (5-3.9) as

$$\begin{aligned}
\delta(\omega(\boldsymbol{k} + \epsilon\boldsymbol{K}) - \omega(\boldsymbol{k})) &= \delta(\omega(\boldsymbol{k}) + \epsilon\boldsymbol{K} \cdot \nabla_{\boldsymbol{k}}\omega + O(\epsilon^2) - \omega(\boldsymbol{k})) \\
&= \epsilon^{-d}\delta(\boldsymbol{c}_g \cdot \boldsymbol{K} + O(\epsilon)) \\
&= \epsilon^{-d}\delta(\boldsymbol{c}_g \cdot \boldsymbol{K}) + O(1),
\end{aligned}$$

and defined the scaled power spectrum

$$\widehat{R}_\epsilon(\boldsymbol{K}) := \epsilon^{-2}\widehat{R}(\epsilon\boldsymbol{K}).$$

With the cross-section (D-0.1) the kinetic equation reads

$$\partial_t a + \nabla_{\boldsymbol{k}}\omega \cdot \nabla_{\boldsymbol{x}} a = \int_{\mathbb{R}^3} \sigma_{\mathrm{WKB}}(\boldsymbol{k}, \boldsymbol{k}')\, a(\boldsymbol{k}', t)\mathrm{d}\boldsymbol{k}' - \Sigma(\boldsymbol{k})\, a(\boldsymbol{k}, t). \tag{D-0.2}$$

Expansion of the kinetic equation

We define a rescaled cross-section

$$S(\boldsymbol{k}, \boldsymbol{K}) = \epsilon^d \sigma_{\mathrm{WKB}}(\boldsymbol{k}, \boldsymbol{k} + \epsilon\boldsymbol{K}),$$

such that

$$\Sigma(\boldsymbol{k}) = \int_{\mathbb{R}^3} S(\boldsymbol{k}, \boldsymbol{K})\mathrm{d}\boldsymbol{K}.$$

The reversibility symmetry of the scattering cross-section, analogous to $\sigma(\boldsymbol{k}, \boldsymbol{k}') = \sigma(\boldsymbol{k}', \boldsymbol{k})$, is expressed for the new function $S(\boldsymbol{k}, \boldsymbol{K})$ as

$$S(\boldsymbol{k}, \boldsymbol{K}) = S(\boldsymbol{k} + \epsilon\boldsymbol{K}, -\boldsymbol{K}). \tag{D-0.3}$$

Taylor expanding (D-0.3) gives

$$\begin{aligned} S(\boldsymbol{k}, \boldsymbol{K}) =& S(\boldsymbol{k} + \epsilon\boldsymbol{K}, -\boldsymbol{K}) \\ =& S(\boldsymbol{k}, -\boldsymbol{K}) + \epsilon K_i \partial_i S(\boldsymbol{k}, -\boldsymbol{K}) + \frac{\epsilon^2}{2} K_i K_j \partial_i \partial_j S(\boldsymbol{k}, -\boldsymbol{K}) + O(\epsilon^3), \end{aligned} \tag{D-0.4}$$

where $\partial_i = \partial/\partial k_i$ and Einstein summation is assumed.

Applying the same expansion with $\boldsymbol{K} \to -\boldsymbol{K}$ gives

$$\begin{aligned} S(\boldsymbol{k}, -\boldsymbol{K}) =& S(\boldsymbol{k} - \epsilon\boldsymbol{K}, \boldsymbol{K}) \\ =& S(\boldsymbol{k}, \boldsymbol{K}) - \epsilon K_i \partial_i S(\boldsymbol{k}, \boldsymbol{K}) + \frac{\epsilon^2}{2} K_i K_j \partial_i \partial_j S(\boldsymbol{k}, \boldsymbol{K}) + O(\epsilon^3) \end{aligned} \tag{D-0.5}$$

Thus subtracting (D-0.5) from (D-0.4) we find

$$S(\boldsymbol{k},\boldsymbol{K}) - S(\boldsymbol{k},-\boldsymbol{K}) = \epsilon K_i \partial_i S(\boldsymbol{k},\boldsymbol{K}) - \frac{\epsilon^2}{2} K_i K_j \partial_i \partial_j S(\boldsymbol{k},\boldsymbol{K}) + O(\epsilon^3). \tag{D-0.6}$$

Using (D-0.6), we see

$$\begin{aligned}\int K_i S(\boldsymbol{k},\boldsymbol{K}) \mathrm{d}\boldsymbol{K} &= \frac{1}{2}\int K_i \big(S(\boldsymbol{k},\boldsymbol{K}) - S(\boldsymbol{k},-\boldsymbol{K})\big)\mathrm{d}\boldsymbol{K} \\ &= \frac{\epsilon}{2}\int K_i K_j \partial_j S(\boldsymbol{k},\boldsymbol{K})\mathrm{d}\boldsymbol{K} + O(\epsilon^2).\end{aligned} \tag{D-0.7}$$

We now expand $a(\boldsymbol{k}',t)$ in the kinetic equation (D-0.2) to find

$$\begin{aligned}\partial_t a + \nabla_{\boldsymbol{k}}\omega\cdot\nabla_{\boldsymbol{x}} a &= \int_{\mathbb{R}^3} \sigma_{\mathrm{WKB}}(\boldsymbol{k},\boldsymbol{k}')\, a(\boldsymbol{k}',t)\mathrm{d}\boldsymbol{k}' - \Sigma(\boldsymbol{k})\, a(\boldsymbol{k},t) \\ &= \int_{\mathbb{R}^3} S(\boldsymbol{k},\boldsymbol{K}) a(\boldsymbol{k}+\epsilon\boldsymbol{K},t)\mathrm{d}\boldsymbol{K} - \Sigma(\boldsymbol{k})\, a(\boldsymbol{k},t) \\ &= \int_{\mathbb{R}^3} S(\boldsymbol{k},\boldsymbol{K})\Big(\epsilon K_i\partial_i + \frac{\epsilon^2}{2}K_iK_j\partial_i\partial_j\Big)\mathrm{d}\boldsymbol{K}\ a(\boldsymbol{k},t) \\ &\quad + O(\epsilon^3).\end{aligned} \tag{D-0.8}$$

Diffusion equation

We substitute the expression (D-0.7) into (D-0.8) to finally allow the expansion of the kinetic equation, in the limit $\epsilon \to 0$, to be expressed as

$$\partial_t a + \nabla_{\boldsymbol{k}}\omega\cdot\nabla_{\boldsymbol{x}} a = \nabla_{\boldsymbol{k}}\cdot\big(\mathbf{D}\cdot\nabla_{\boldsymbol{k}}\, a(\boldsymbol{k},t)\big),$$

where the diffusivity tensor $\mathbf{D}$ has its components defined by

$$D_{ij}(\boldsymbol{k}) = \frac{1}{2}\int_{\mathbb{R}^3} S(\boldsymbol{k},\boldsymbol{K})(\hat{\boldsymbol{e}}_i\cdot\boldsymbol{K})(\hat{\boldsymbol{e}}_j\cdot\boldsymbol{K})\mathrm{d}\boldsymbol{K}. \tag{D-0.9}$$

The expression (D-0.9) is identical to (C-1.3). We note that, in the notation of this chapter, (C-2.3) shows

$$k_m k_n \widehat{\Pi}_{mn} = |\boldsymbol{k}_h \times \boldsymbol{K}_h|^2 \widehat{R}_\epsilon(\boldsymbol{K}),$$

and that the factor $(2\pi)^3$ difference between (D-0.9) and (C-1.3) is due to different Fourier transform conventions having been applied between the two derivations.

Thus, diffusion in the k-direction along the cone is controlled by the coefficient

$$\begin{aligned} D_{kk}(\boldsymbol{k}) &= \frac{1}{2}\int_{\mathbb{R}^3} S(\boldsymbol{k},\boldsymbol{K})(\hat{\boldsymbol{e}}_k \cdot \boldsymbol{K})^2 \mathrm{d}\boldsymbol{K} \\ &= \frac{1}{2}\int_{\mathbb{R}^3} \sigma_{\mathrm{WKB}}(\boldsymbol{k},\boldsymbol{k}')(\hat{\boldsymbol{e}}_k \cdot (\boldsymbol{k}'-\boldsymbol{k})/\epsilon)^2 \mathrm{d}\boldsymbol{k}', \end{aligned}$$

while horizontal isotropisation is controlled by

$$D_{\varphi\varphi}(\boldsymbol{k}) = \frac{1}{2}\int_{\mathbb{R}^3} \sigma_{\mathrm{WKB}}(\boldsymbol{k},\boldsymbol{k}')(\hat{\boldsymbol{e}}_\varphi \cdot (\boldsymbol{k}'-\boldsymbol{k})/\epsilon)^2 \mathrm{d}\boldsymbol{k}'.$$

As in Appendix C, the other components $D_{k\varphi} = D_{\varphi k}$ and $D_{i\theta} = D_{\theta i}$ for $i = k, \varphi, \theta$ are all zero.

Bibliography

Alford, M.H., McKinnon, J.A., Simmons, H.L. and Nash, J.D. (2016). Near-inertial internal gravity waves in the ocean. *Annu. Rev. Mar. Sci.*, **8**, 95–123.

Bal, G. (2005). Kinetics of scalar wave fields in random media. *Wave Motion*, **43**, 132–157.

Bal, G., Komorowski, T. and Ryzhik, L. (2010). Kinetic limits for waves in a random medium. *Kinetic Rel. Models*, **3**, 529–644.

Bartello, P. (1995). Geostrophic adjustment and inverse cascades in rotating stratified turbulence. *J. Atmos. Sci.*, **52**, 4410–4428.

Besieris, I.M. (1987). Stochastic wave-kinetic theory of radiative transfer in the presence of ionization. *Rad. Sci.*, **22**, 885–888.

Bühler, O., Callies, J. and Ferrari, R. (2014). Wave-vortex decomposition of one-dimensional ship-track data. *J. Fluid. Mech.*, **756**, 1007–1026.

Bühler, O. (2014). *Waves and Mean Flows*. Cambridge Monographs on Mechanics, Cambridge University Press, 2nd edn.

Callies, J. (2016). *Submesoscale turbulence in the upper ocean*. Ph.D. thesis, Massachusetts Institute of Technology.

Callies, J. and Ferrari, R. (2013). Interpreting Energy and Tracer Spectra of Upper-Ocean Turbulence in the Submesoscale Range (1–200 km). *J. Phys. Oceanogr.*, **43**, 2456–2474.

Callies, J., Ferrari, R. and Bühler, O. (2014). Transition from geostrophic turbulence to inertia–gravity waves in the atmospheric energy spectrum. *Proc. Natl. Acad. Sci.*, **111**, 17033–17038.

Callies, J., Bühler, O. and Ferrari, R. (2016). The dynamics of mesoscale winds in the upper troposphere and lower stratosphere. *J. Atmos. Sci.*, **73**, 4853–4872.

Chavanne, C., Flament, P., Carter, G., Merrifield, M., Luther, D., Zaron, E. and Gurgel, K.W. (2010). The surface expression of semidiurnal internal tides near a strong source at Hawaii. part i: Observations and numerical predictions. *J. Phys. Oceanogr.*, **40**, 1155–1179.

Danioux, E. and Vanneste, J. (2016). Near-inertial-wave scattering by random flows. *Phys. Rev. Fluids*, **1**, 033701.

de Lavergne, C., Falahat, S., Madec, G., Roquet, F., Nycander, J. and Vic, C. (2019). Toward global maps of internal tide energy sinks. *Ocean Modelling*, **137**, 52–75.

Dunphy, M. and Lamb, K. (2014). Focusing and vertical mode scattering of the first mode internal tide by mesoscale eddy interaction. *J. Geophys. Res.: Oceans*, **119**, 523–536.

Dunphy, M., Ponte, A.L., Klein, P. and Le Gentil, S. (2017). Low-mode internal tide propagation in a turbulent eddy field. *J. Phys. Oceanogr.*, **47**, 649–665.

Eden, C., Chouksey, M. and Olbers, D. (2019). Mixed rossby–gravity wave–wave interactions. *J. Phys. Oceanogr.*, **49**, 291–308.

Ferrari, R. and Wunsch, C. (2009). Ocean circulation kinetic energy: reservoirs, sources and sinks. *Ann. Rev. Fluid Mech.*, **41**, 253–182.

Flatté, S.M., Henyey, F.S. and Wright, J.A. (1985). Eikonal calculations of short-wavelength internal-wave spectra. *J. Geophys. Res.: Oceans*, **90**, 7265–7272.

Garrett, C. and Munk, W. (1972). Space-Time scales of internal waves. *Geophysical Fluid Dynamics*.

Gill, A. (1982). *Atmosphere–Ocean Dynamics*. Elsevier Science.

Hasselmann, K. (1962). On the non-linear energy transfer in a gravity-wave spectrum part 1. general theory. *J. Fluid. Mech.*, **12**, 481–500.

Hasselmann, K. (1967). *Weak-interaction theory of ocean waves*. Institut für Schiffbau der Universität Hamburg.

Henyey, F.S. and Pomphrey, N. (1983). Eikonal description of internal wave interactions: A non-diffusive picture of "induced diffusion". *Dyn. Atmos. Oceans*, **7**, 189–219.

Jin, S. and Wen, X. (2006). Hamiltonian-preserving schemes for the liouville equation of geometrical optics with discontinuous local wave speeds. *Journal of Computational Physics*, **214**, 672–697.

Kafiabad, H.A. and Bartello, P. (2016). Balance dynamics in rotating stratified turbulence. *J. Fluid Mech.*, **795**, 914–949.

Kafiabad, H.A. and Bartello, P. (2018). Spontaneous imbalance in the non-hydrostatic boussinesq equations. *Journal of Fluid Mechanics*, **847**, 614–643.

Kafiabad, H.A., Savva, M.A.C. and Vanneste, J. (2019). Diffusion of inertia-gravity waves by geostrophic turbulence. *J. Fluid. Mech.*, **869**, R7.

Kelly, S.M. and Lermusiaux, P.F.J. (2016). Internal-tide interactions with the Gulf Stream and Middle Atlantic Bight shelfbreak front. *J. Geophys. Res.: Oceans*, **121**, 6271–6294.

Kelly, S.M., Lermusiaux, P.F.J., Duda, T.F. and Haley, P.J. (2016). A coupled-mode shallow-water model for tidal analysis: Internal tide reflection and refraction by the Gulf Stream. *J. Phys. Oceanogr.*, **46**, 3661–3679.

Lelong, M.P. and Riley, J.J. (1991). Internal wave–vortical mode interactions in strongly stratified flows. *J. Fluid Mech.*, **232**, 1–19.

Li, Q. and Lindborg, E. (2018). Weakly or strongly nonlinear mesoscale dynamics close to the tropopause? *J. Atmos. Sci.*, **75**, 1215–1229.

Liu, H.L. (2019). Quantifying gravity wave forcing using scale invariance. *Nat. Commun.*, **10**.

Lvov, Y.V., Polzin, K.L. and Yokoyama, N. (2012). Resonant and near-resonant internal wave interactions. *J. Phys. Oceanogr.*, **42**, 669–691.

Lynch, P. (2008). The origins of computer weather prediction and climate modeling. *Journal of Computational Physics*, **227**, 3431–3444.

MacKinnon, J.A. and Winters, K.B. (2005). Subtropical catastrophe: Significant loss of low-mode tidal energy at 28.9°. *Geophys. Res. Lett.*, **32**.

Majda, A. (2003). *Introduction to PDEs and Waves for the Atmosphere and Ocean*, vol. 9. American Mathematical Soc.

McComas, C.H. and Bretherton, F.P. (1977). Resonant interaction of oceanic internal waves. *J. Geophys. Res.*.

McWilliams, J.C. (2016). Submesoscale currents in the ocean. *Proceedings of the Royal Society A: Mathematical, Physical and Engineering Sciences*, **472**, 20160117.

McWilliams, J.C., Weiss, J.B. and Yavneh, I. (1994). Anisotropy and coherent vortex structures in planetary turbulence. *Science*, **264**, 410–413.

Meiss, J.D. and Watson, K.M. (1982). Internal-wave interactions in the induced-diffusion approximation. *J. Fluid. Mech.*, **117**, 315–341.

Modave, A., Deleersnijder, É. and Delhez, É.J. (2010). On the parameters of absorbing layers for shallow water models. *Ocean Dynamics*, **60**, 65–79.

Morrow, R., Fu, L.L., Ardhuin, F., Benkiran, M., Chapron, B., Cosme, E., d'Ovidio, F., Farrar, J.T., Gille, S.T., Lapeyre, G. *et al.* (2019). Global observations of fine-scale ocean surface topography with the surface water and ocean topography (SWOT) mission. *Frontiers in Marine Science*, **6**, 232.

Müller, P. (1976). On the diffusion of momentum and mass by internal gravity waves. *J. Fluid Mech.*, **77**, 789–823.

Müller, P. (1977). Spectral features of the energy transfer between internal waves and a larger-scale shear flow. *Dynam. Atmos. Oceans*, **2**, 49–72.

Müller, P. and Olbers, D.J. (1975). On the Dynamics of Internal Waves in the Deep Ocean. *J. Geophys. Res.*, **27**, 3848–3860.

Müller, P. (2006). *The Equations of Oceanic Motions*. Cambridge University Press.

Müller, P., Holloway, G., Henyey, F. and Pomphrey, N. (1986). Nonlinear interactions among internal gravity waves. *Rev. Geophys.*, **24**, 493–536.

Nastrom, G.D. and Gage, K.S. (1985). A climatology of atmospheric wavenumber spectra of wind and temperature observed by commercial aircraft. *J. Atmos. Sci.*, **42**, 950–960.

Nazarenko, S. (2011). *Wave Turbulence*. Springer, 1st edn.

NIST Digital Library of Mathematical Functions (2018). http://dlmf.nist.gov/, Release 1.0.21 of 2018-12-15 (ed. F. W. J. Olver, A. B. Olde Daalhuis, D. W. Lozier, B. I. Schneider, R. F. Boisvert, C. W. Clark, B. R. Miller and B. V. Saunders).

Olbers, D. (1981). A Formal Theory of Internal Wave Scattering with Applications to Ocean Fronts. *J. Phys. Oceanogr.*, **11**, 1078–1099.

Olbers, D., Willebrand, J. and Eden, C. (2012). *Ocean Dynamics*. Springer, 1st edn.

Olbers, D.J. (1976). Nonlinear energy transfer and the energy balance of the internal wave field in the deep ocean. *J. Fluid. Mech.*, **74**, 375.

Ponte, A.L. and Klein, P. (2015). Incoherent signature of internal tides on sea level in idealized numerical simulations. *Geophys. Res. Lett.*, **42**, 1520–1526.

Powell, J. and Vanneste, J. (2005). Transport equations for waves in randomly perturbed Hamiltonian systems, with application to Rossby waves. *Wave Motion*, **42**, 289 – 308.

Qiu, B., Nakano, T., Chen, S. and Klein, P. (2017). Submesoscale transition from geostrophic flows to internal waves in the northwestern pacific upper ocean. *Nat. Commun.*, **8**, 14055.

Qiu, B., Chen, S., Klein, P., Wang, J., Torres, H., Fu, L.L. and Menemenlis, D. (2018). Seasonality in transition scale from balanced to unbalanced motions in the world ocean. *J. Phys. Oceanogr.*, **48**, 591–605.

Rainville, L. and Pinkel, R. (2006). Propagation of low-mode internal waves through the ocean. *J. Physl Oceanogr.*, **36**, 1220–1236.

Ray, R.D. and Zaron, E.D. (2016). M2 internal tides and their observed wavenumber spectra from satellite altimetry. *J. Phys. Oceanogr.*, **46**, 3–22.

Rocha, C.B., Chereskin, T.K., Gille, S.T. and Menemenlis, D. (2016). Mesoscale to Submesoscale Wavenumber Spectra in Drake Passage. *J. Phys. Oceanogr.*, **46**, 601–620.

Ryzhik, L. (2014). Waves in weakly random media: lecture notes for the Vienna Inverse Problems school.

Ryzhik, L., Papanicolaou, G. and Keller, J.B. (1996). Transport equations for elastic and other waves in random media. *Wave Motion*, **24**, 327 – 370.

Salmon, R. (1998). *Lectures on Geophysical Fluid Dynamics*. Oxford University Press, New York.

Savva, M.A.C. and Vanneste, J. (2018). Scattering of internal tides by barotropic quasigeostrophic flows. *J. Fluid. Mech.*, **856**, 504–530.

Staquet, C. and Sommeria, J. (2002). Internal gravity waves: from instabilities to turbulence. *Annu. Rev. Fluid Mech.*, **34**, 559–593.

Thomas, J. and Yamada, R. (2019). Geophysical turbulence dominated by inertia–gravity waves. *J. Fluid. Mech.*, **875**, 71–100.

Thomas, J., Smith, K.S. and Bühler, O. (2017). Near-inertial wave dispersion by geostrophic flows. *J.Fluid Mech.*, **817**, 406–438.

Thorpe, S.A. (2005). *The turbulent ocean*. Cambridge University Press.

Torres, H.S., Klein, P., Menemenlis, D., Qiu, B., Su, Z., Wang, J., Chen, S. and Fu, L.L. (2018). Partitioning ocean motions into balanced motions and internal gravity waves: A modeling study in anticipation of future space missions. *Journal of Geophysical Research: Oceans*, **123**, 8084–8105.

Vallis, G.K. (2017). *Atmospheric and Oceanic Fluid Dynamics: Fundamentals and Large-Scale Circulation*. Cambridge University Press, 2nd edn.

Vanneste, J. (2013). Balance and Spontaneous Wave Generation in Geophysical Flows. *Annu. Rev. Fluid Mech.*, **45**, 147–172.

Villani, C. (2008). H-theorem and beyond: Boltzmann's entropy in today's mathematics. In *Boltzmann's Legacy,* Gallavoti, G., Reiter, W.L., Yngvason, J., Eds., EMS Publishing House, Zürich, Switzerland, pp. 129–143.

Wagner, G.L. and Young, W.R. (2016). A three-component model for the coupled evolution of near-inertial waves, quasi-geostrophic flow and the near-inertial second harmonic. *J. Fluid Mech.*, **802**, 806–837.

Wagner, G.L., Ferrando, G. and Young, W.R. (2017). An asymptotic model for the propagation of oceanic internal tides through quasi-geostrophic flow. *J. Fluid Mech.*, **828**, 779–811.

Waite, M.L. (2017). Random forcing of geostrophic motion in rotating stratified turbulence. *Physics of Fluids*, **29**, 126602.

Waite, M.L. and Bartello, P. (2006a). Stratified turbulence generated by internal gravity waves. *J. Fluid. Mech.*, **546**, 313–339.

Waite, M.L. and Bartello, P. (2006b). The transition from geostrophic to stratified turbulence. *J. Fluid. Mech.*, **568**, 89–108.

Ward, M.L. and Dewar, W.K. (2010). Scattering of gravity waves by potential vorticity in a shallow-water fluid. *J. Fluid Mech.*, **663**, 478–506.

Warn, T. (1986). Statistical mechanical equilibria of the shallow water equations. *Tellus A*, **38**, 1–11.

Watson, K.M. (1985). Interaction between internal waves and mesoscale flow. *J. Phys. Oceanogr.*, **15**, 1296–1311.

Wheeden, R. and Zygmund, A. (2015). *Measure and Integral: An Introduction to Real Analysis, Second Edition.* Chapman & Hall/CRC Pure and Applied Mathematics, CRC Press, 2nd edn.

Wigner, E. (1932). On the quantum correction for thermodynamic equilibrium. *Phys. Rev.*, **40**, 749–759.

Wunsch, C. and Ferrari, R. (2004). Vertical mixing, energy, and the general circulation of the oceans. *Annu. Rev. Fluid Mech.*, **36**, 281–314.

Xie, J.H. and Vanneste, J. (2015). A generalised-Lagrangian-mean model of the interactions between near-inertial waves and mean flow. *J. Fluid Mech.*, **774**, 143–169.

Young, W.R. and Ben Jelloul, M. (1997). Propagation of near-inertial oscillations through a quasi-geostrophic flow. *J. Mar. Res.*, **55**, 735–766.

Zakharov, V., Dias, F. and Pushkarev, A. (2004). One-dimensional wave turbulence. *Physics Reports*, **398**, 1–65.